Stony Brook University

Effects of Disordered Dopants on the Electronic Structure of Functional Materials: Wannier Function-Based First Principles Methods for Disordered Systems

A Dissertation Presented

by

Tom Berlijn

to

The Graduate School

in Partial Fulfillment of the Requirements

for the Degree of

Doctor of Philosophy

in

Physics

Stony Brook University

August 2011

Stony Brook University

The Graduate School

Tom Berlijn

We, the dissertation committee for the above candidate for the Doctor of Philosophy degree, hereby recommend acceptance of this dissertation.

Wei Ku - Advisor
Physicist, CMPMSD, Brookhaven National Laboratory

Philip Allen - Committee Chair
Professor, Department of Physics and Astronomy

Axel Drees
Professor, Department of Physics and Astronomy

Mark S. Hybertsen
Group Leader, CFN, Brookhaven National Laboratory

This dissertation is accepted by the Graduate School

Lawrence Martin
Dean of the Graduate School

ii

Abstract of the Dissertation

Effects of Disordered Dopants on the Electronic Structure of Functional Materials: Wannier Function-Based First Principles Methods for Disordered Systems

by

Tom Berlijn

Doctor of Philosophy

in

Physics

Stony Brook University

2011

Doping is one of the most powerful tools for tuning the electronic properties of functional materials. Well known examples include doped semiconductors and the Cu and Fe based high temperature superconductors. Besides introducing charge carriers and chemical pressure, it is almost inevitable that dopants will introduce quenched disorder into the system. This can have a wide range of consequences for the electronic structure, such as electric and thermal resistance, a deformation of the nodal structure of a superconductor or Anderson localization.

In this thesis the influence of disordered dopants is studied by calculating the configuration-averaged spectral function $\langle A(k, \omega) \rangle$ from first principles within the super cell approximation. To overcome two major problems of the super cell approximation, the

band folding and the computational expense, two Wannier function based first principles techniques are developed.

The developed methodology is applied to address three realistic materials problems. The first problem is on the influence of disorder on the Fermi surface of NaxCoO2, an important thermoelectric material. The second problem is on the role of oxygen vacancies in the room temperature ferromagnetism in the recently discovered dilute magnetic semiconductor Cu:ZnO. The third problem is on the carrier doping and charge localization in transition metal doped iron based superconductors.

To my mother.

Contents

List of Figures

List of Tables

Chapter 1

Introduction: Material Science, First Principles Simulations, Crystals and Disorder

In the first section of this chapter we introduce the general area of research, namely material science and first principles calculations. In the second section we introduce the topic of this thesis, being disordered materials. What are they and why should we study them?

1.1 Material Science and First Principles Calculations

Material science studies the mechanical, chemical, electronic and optical properties of materials and is a very broad area of research that besides being a discipline of its own, overlaps with chemistry, physics, geophysics, molecular biology, engineering, etc. Material properties play a key role in modern technology development. We can think for example of technology related to the biggest problem of our time, the energy problem. How well a solar cell can convert sunlight into current, depends on the energy it takes to excite an electron (bandgap) and how stable this excitation is (exciton lifetime). In order for a thermoelectric to efficiently convert heat into a voltage, it needs to have high electric conductivity and low thermal conductivity. The voltage of a bat-

tery depends on the amount of ions that can be intercalated in the cathode material. To use superconductivity for transporting electrical energy without heating losses, a material needs to be found with high transition temperature and a high critical current. We can also think of information technology. The amount of data that can be stored in a hard disk depends on the ferromagnetic "hardness" of the storage material. To continue Moore's law of yearly doubling the number of transistors in an integrated chip the traditional silicon is replaced by materials with a higher dielectric constant (such as hafnium oxide) in order to prevent current leakage. The list of examples goes far beyond energy and information technology, from the catalytic effect of an enzyme that depends on its influence on the reaction barrier, to the corrosion resistance of alloys to produce good coatings.

To study these important properties of materials there exists a tremendous amount of experimental techniques. On the one hand materials can be exposed to extreme circumstances such as a pressure of 100GPa or a temperature almost at the absolute freezing point. On the other hand, there is an endless list of experimental probes x-ray absorption, electron microscopy or photo emission spectroscopy, to mention just a few. Given the resulting overwhelming amount of experimental data, the role of theoretical material science is to put it all together in order to gain insight in the origin of the properties of materials. For example, theoretical material scientists ask themselves questions like why do materials with a high superconducting-transition temperature also tend to become magnetic? The answer to such questions would not only satisfy scientific curiosity, it could be of guidance in finding new materials with a higher superconducting-transition temperature.

The traditional approach for theoretical material science is to find the simplest model that is consistent with the given experimental data on a wide range of materials that behave similarly, lets say the high temperature superconductors. The modeling approach aims at getting a general insight for a wide class of materials. A much younger approach, made possible only by the invention of the computer, is to simulate materials from first principles. In this approach the atomic positions and their influence on the electrons are fully taken into account, without the use of free parameters. One calculation in this approach corresponds to one specific material, for example $Ba_8Fe_{14}Co_2As_{16}$,

instead of all the iron based superconductors. In some sense the first principles simulations have the characteristics of an experiment: the theorists puts $Ba_8Fe_{14}Co_2As_{16}$ into the simulation and sees what comes out. One of the exciting aspects of first principles simulations is its potential to virtually design new materials [1]. Simulating new materials or new phases of materials on the computer is of course much faster and far less costly then synthesizing it in the lab. Another important role of the first principles simulations is to function as a bridge between the modeling approach and the experiments. On the one hand the first-principles simulations can guide experimentalist in interpreting their data in terms of physical models. On the other hand first-principles simulations can provide realistic parameters for models and more importantly they can provide information on which models to use.

1.2 Crystalline and Disordered Materials
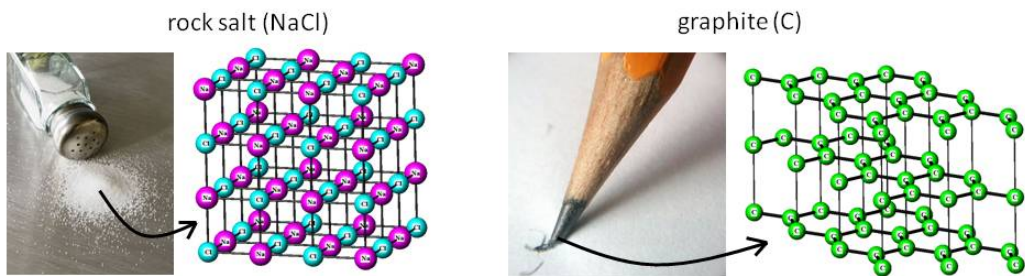
Figure 1.1: Two every day examples of crystals.

In this thesis we are interested in simulating from first principles the properties of disordered materials. Let us first start by explaining what disordered materials are, which is best done by explaining what they are not, namely crystals. Crystals are materials consisting of atoms or molecules that are arranged in a perfectly periodically repeating pattern (see figure 1.1 for two everyday examples of crystals). In 1928 Felix Bloch published a remarkable theorem about the conduction of electrons in crystals. The theorem says that the wave functions of electrons do not scatter against atoms that are periodically arranged. Instead the electron wave functions adjusts themselves smoothly to the periodic atoms and freely flow through the crystal. The energy spectrum of

these free waves, called the band structure, became one of the most useful concepts from which many electronic properties of crystalline materials could be understood, such as the conduction of heat and electric charge or magnetism and superconductivity.
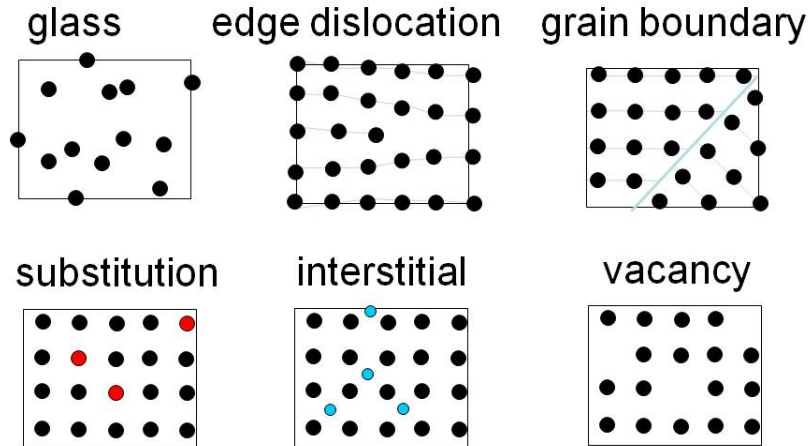
Figure 1.2: Types of disorder. The doping-induced disorders such as substitutions, interstitials and vacancies are also known as cellular disorders, because there is an underlying lattice present. The glass, edge dislocation and grain boundary have no such underlying lattice.

The disordered materials are all the other materials that are not crystals. Why should we study disordered materials? If we just look around us, and ignore the table salt and the pencils, we see stone, wood, paper, glass, plastic and water. The atomic and molecular arrangement in these materials are far from crystalline. But even if we focus ourselves on crystals, as we will do in this thesis, in reality there will always be disorder present (see figure 1.2). When a crystalline sample is synthesized in the lab it typically tends to grow not as one single crystal but as many different crystal grains. At the boundaries of these crystal grains the periodicity is broken. Even within a single crystal grain small defects occur by random chance. These defects are not just bad luck, they have to be there according to a fundamental law of physics called the second law of thermodynamics. Since the materials from which crystals are made are never a 100 percent pure, crystals will always contain impurities. What the above mentioned disorders, grain boundaries, defects and impurities, have in common is that they break the periodicity of

the crystal and therefore that Bloch's theorem will not be applicable for them. The electrons will scatter from the disorders and therefore experience electrical resistance. This means that unless the crystal is in a superconducting phase, the more disorder there is, the more electrical energy transported through a crystal will be lost into heat. Therefore to remove impurities and defects from crystals as much as possible is an important and difficult challenge for crystal growers. Surprisingly however, these same crystals growers, more often then not, deliberately grow defects and impurities into the crystals, by a process called doping.

Doping is one of the most powerful ways to tune the important properties of functional materials. The most famous example probably is doped silicon. Depending on whether silicon is doped with for example phosphorous (which has one more electron then silicon) or boron (which has one less electron then silicon) negative (n-type) or positive (p-type) charge carriers are inserted. From the resulting n-type and p-type semiconductors, transistors and diodes can be made which in turn are the basic building blocks of all modern electronic devices. Another famous example are the high temperature superconductors. La_2CuO_4 is a so called charge transfer insulator, but when 5 percent of the La's are replaced by Sr, it becomes a superconductor. It is indeed truly a miracle that such a little change in the chemical composition can have such an extreme consequence for the conductivity.

The dopants have several effects. The dopants generally introduce carriers into the system like for example in the above mentioned doped semiconductors. At the same time the dopants will exert what is called a chemical pressure, for example they might attract their neighboring atoms and thereby compress the system. Effects very similar to the ones mentioned above can also be accomplished more directly. A material can be hooked up to a battery to increase its number of carriers or it can be placed in a pressure cell to get compressed. However it is clear that a material will not be very useful for building a device, if it constantly needs to be put under high pressure or hooked up to a battery. Finally there is also a third effect of the dopants that does not have such a direct analogue, namely the dopants will break the periodicity of the crystal and therefore introduce disorder in the crystal.

Sofar we have presented disorder as something that is inevitably present,

but there is more to it. Disorder itself can play a crucial role for the properties of materials. For example in a pure crystal, the layers of atoms might easily slide over one another, but point-defects and dislocations can stop that and therefore are directly responsible for the hardness of the material. Disorder is probably even more of a crucial factor for the electronic properties. A famous discovery by Phil Anderson [2] is that even though individual impurities might only scatter the electrons, the quantum mechanical interference in a cluster of impurities can completely localize an electron. In terms of material properties this means that if a sufficient amount of disorder is introduced in a crystal it will not just become a bad conductor, it can be made an insulator. Defects in a current carrying type II superconductor will pin magnetic flux lines, which would otherwise move and destroy the superconducting state [3]. The integer quantum hall effect, good for the Nobel prize of 1985, can only occur in the presence of disorder [4]. Disorder is capable of forming local magnetic moments [5–7], which in turn can give rise to important magnetic properties. Disorder is believed to be one of the key ingredients for the nanoscale electronic inhomogeneity observed in transition metal oxides such as cuprates, manganites and cobaltates, but also in the newly discovered Fe based superconductors [8]. Elbio Dagotto [9] argues that this disorder induced nanoscale electronic inhomogeneity is responsible for the collosal magnetic resistance (CMR) in manganites, an effect that has the potential to drastically enhance the amount of data stored in hard disks.

So let us now get back to our question, why do we study disordered systems? On the one hand it is clear that disorder is present everywhere, especially in the very important doped materials and therefore its influence can not be ignored. On the other hand disorder is a crucial ingredient for many important electronic properties.

1.3 Overview of the Thesis

To approach the study of disordered systems we focus ourselves on a limited kind of disorder in which there is an underlying lattice present. These so-called cellular disorders include the doping induced impurities such as substitutions, interstitials and vacancies (the lower three in figure 1.2), but not for exam-

ple dislocations, grain boundaries or glasses(the upper three in figure 1.2). Furthermore we will be focusing ourselves on the bandstructure of disordered materials. As we argued in the beginning of this section, the bandstructure has been the fundamental quantity from which a tremendous amount of crystal properties have been understood and calculated. In this thesis we want to study quantitatively what happens to the bandstructure when disorder is introduced in the crystal.

chapter 2

Density Functional Theory	Wannier functions
WIEN2K (commercial software)	**GenWannier_h_KS (by Wei Ku)**
Input: experimental lattice structure + Schroedinger equation	**Input:** bandstructures + LAPW-based Blochwaves of ordered systems
Output: bandstructures + LAPW-based Blochwaves of ordered systems	**Output:** Wannier based tight binding Hamiltonian of ordered systems

Unfolding	Effective Hamiltonian
GenWannier_BandStructure_SC_with_H + Wan_BS_2_pnm (by Wei Ku)	**hdelta.cpp + heff.cpp (by Tom Berlijn)**
Input: Wannier based tight binding Hamiltonian of disordered systems	**Input:** Wannier based tight binding Hamiltonian of ordered systems
Output: bandstructure of disordered systems	**Output:** Wannier based tight binding Hamiltonian of disordered systems

chapter 3

Figure 1.3: Flow chart of the codes used to obtain bandstructures of disordered systems from first principles.

In chapters 2 and 3 the methodology is presented that allows the calculation of the bandstructures of disordered systems from first principles. Behind the

scenes of the formal presentation of the methods in this thesis, there is a series of codes that we represent in the flow chart in figure 1.3. In chapter 2 we will set up the technological background. In chapter 3 we present the newly developed Wannier function based methods that facilitate the study of the influence of disorder on the bandstructure from first principles. In chapters 4, 5 and 6 we will use the developed methodology to address realistic materials problems. In chapter 4 we will compute the influence of disorder on the Fermi surface of sodium doped cobaltate (Na_xCoO_2), an important thermoelectric material. In chapter 5 we will investigate the role of oxygen vacancies in the room temperature ferromagnetism in copper doped zinc oxide (Cu:ZnO), a recently discovered dilute magnetic semiconductor. In chapter 6 we will investigate carrier doping and charge localization in transition metal doped iron based superconductors.

Chapter 2

Background: Density Functional Theory, Linear Augmented Plane Waves and Wannier Functions

In this chapter we discuss three general methods that have been developed outside of the context of this thesis. The first two sections are based on standard text books. Specifically section 2.1 is based on [10, 11] and section 2.2 is based on [12–14]. The last section, section 2.3, is mostly based on discussions with Wei Ku.

2.1 Density Functional Theory

The starting point of most first principles methods is the Schroedinger equation of the electrons in the background of the classical external potentials of the

atomic nuclei[1]

$$\left(-\frac{\hbar^2}{2m} \sum_j \nabla_j^2 - \sum_{j,l} \frac{Z_l e^2}{|r_j - R_l|} + \sum_{j<j'} \frac{e^2}{|r_j - r_j'|} \right) \Psi(r_1, ..., r_N) = E\Psi(r_1, ..., r_N)$$

(2.1)

where j labels the N electrons and l labels the atomic nuclei. From the solutions of the Schroedinger equation $\Psi(r_1, ..., r_N)$, for which the total wave function $\Psi(r_1, ..., r_N)\chi(s_1, ..., s_N)$ are antisymmetric under exchange of electrons, all properties of all materials can be obtained. However, unless something fundamentally changes about our computers, it is a pretty safe bet that the Schroedinger for any reasonably sized system can never be solved. To get a flavor of how complicated it is lets use Walter Kohn's "guesstimate" from his Nobel lecture [15] of the computational expense of calculating the ground state wave function Ψ_0 and ground state energy E_0 from the variational principle:

$$\underset{min\Psi}{E}[\Psi] = E[\Psi_0] = E_0 \ ; \ E[\Psi] = T[\Psi] + U[\Psi] + V[\Psi]$$

(2.2)

where the kinetic energy $T[\Psi]$, the interaction energy $U[\Psi]$ and the external energy $V[\Psi]$ are given by:

$$T[\Psi] = -\frac{\hbar^2}{2m} \int dr_1...dr_N \Psi^*(r_1, ..., r_N) \sum_j \nabla_j^2 \Psi(r_1, ..., r_N)$$

$$U[\Psi] = \int dr_1...dr_N |\Psi(r_1, ..., r_N)|^2 \sum_{j<j'} u(r_j, r_{j'}) \ ; \ u(r, r') = \frac{e^2}{|r - r'|}$$

$$V[\Psi] = \int dr_1...dr_N |\Psi(r_1, ..., r_N)|^2 \sum_j v(r_l) \ ; \ v(r) = \sum_l \frac{Z_l e^2}{|r - R_l|}$$

Suppose we want to calculate the ground state wave function $\Psi_0(r_1, r_2, r_3, r_4, r_5)$ of a system with 5 electrons by evaluating it on 10 grid points for each coordinate then we have are left with a 10^{15} dimensional minimization problem. The ground state wave function of such a system with such a small amount

---

[1]The approximation of separating the nuclear and electronic wave function is based on the fact that the nuclear mass is much larger then the electron mass. The classical nuclei approximation is based on the fact that nuclear wave functions are usually smaller than the distance between nuclei [10].

of electrons therefore is already practically impossible to solve, let alone the ground state wave function of a solid containing 10^{23} electrons.

2.1.1 The Hohenberg Kohn Theorems

The original idea of density functional theory is to exploit the fact that many relevant material properties can be calculated from a quantity that is much simpler then the electron wave function, namely the electron density

$$n(x) = N \int dr_2...dr_N |\Psi(x, r_2, ..., r_N)|^2. \tag{2.3}$$

The Hohenberg Kohn theorems [16] prove that in principle it is possible to calculate the density $n(x)$ directly without calculating the wave function $\Psi(r_1, ..., r_N)$. If we realize that the external energy can be expressed in terms of the density:

$$V[\Psi] = N \int dx dr_2...dr_N |\Psi^*(x, r_2, ..., r_N)|^2 v(x) = \int dx n(x) v(x) \tag{2.4}$$

the Hohenberg Kohn theorems are technically (although not conceptually) simple to prove, especially when the ground states are assumed to be non-degenerate.

claim 1 *Given an interaction $u(x, x')$, then for each non-degenerate ground state density $n_0(x)$ there exists a unique external potential $v(x)$*

proof 1 *Suppose there are two different external potentials $v_1(x)$ and $v_2(x)$ with ground state energies E_1 and E_2, ground state wave functions Ψ_1 and Ψ_2, and identical ground state density $n_0(x)$. Applying the variational principle (2.2) to the system with external potential $v_1(x)$ we find:*

$$E_1 < E_1[\Psi_2] = T[\Psi_2] + U[\Psi_2] + \int dx n_0(x) v_1(x) = E_2 + \int dx n_0(x)(v_1(x) - v_2(x)) \tag{2.5}$$

Similarly using the variational principle for the system with external potential

$v_2(x)$ *we find:*

$$E_2 < E_1 + \int dx n_0(x)(v_2(x) - v_1(x)) \qquad (2.6)$$

Adding (2.5) and (2.6) gives the contradiction: $E_1 + E_2 < E_1 + E_2$

claim 2 *Given an interacting $u(x, x')$ and external potential $v(x)$ there exists an energy density functional which is minimized by the ground state density to the ground state energy.*

proof 2 *All eigenstate wave functions, including the ground state wave function, are a unique functional of the external potential: $\Psi_0[v]$. From claim 1 it follows that the external potential is a unique functional of the ground state density: $v[n_0]$. Therefore we can define the following energy density functional:*

$$E[n] = T[\Psi_0[v[n]]] + U[\Psi_0[v[n]]] + \int dx v(x) n(x) \qquad (2.7)$$

which by construction is minimized by the ground state density to the ground state energy.

The sum of the kinetic energy and interaction density functional is called the universal function $F[n] = T[\Psi_0[v[n]]] + U[\Psi_0[v[n]]]$, because it is independent of the form of the external potential. Finally it is important to remark that the densities over which the energy functional are minimized are not arbitrary. First of all they have to integrate to the number of electrons $\int dx n(x) = N$. A more subtle issue is that the densities have to be v-representable. A density $n(x)$ is said to be v-representable with respect to an interaction $u(x, x')$, if there exists an external potential $v(x)$ that has $n(x)$ as the ground state. This means for example that the functional derivative $\delta E[n]/\delta n(x)$ is only well defined under the assumption that the variations of the ground state density are v-representable.

2.1.2 The Kohn Sham System and the Local Density Approximation

The Hohenberg Kohn theorems formally prove that the universal functional $F[n]$ exists and therefore that in principle the ground state density can be

obtained without calculating the wave function $\Psi(r_1, ..., r_N)$. However, the Hohenberg Kohn theorems by themselves are not very useful, because they don't give any information on the explicit form of the universal functional $F[n]$. Density functional theory therefore only became of practical use after the invention of the Kohn Sham system together with the Local Density Approximation (LDA) [17]. The Kohn Sham system is defined as the non-interacting system which has the same ground state density as the interacting system. This system can then be used to define the exchange correlation functional:

$$E_{XC}[n] \quad = \quad F[n] - \frac{1}{2} \int dx dx' n(x) u(x, x') n(x') - T_s[n] \qquad (2.8)$$

where $T_s[n]$ is the kinetic energy of the non-interacting system. The idea is that by subtracting the classical coulomb interaction and the non-interacting kinetic energy from the unknown universal functional $F[n]$, the remaining exchange correlation functional will be small, such that approximations of it (such as the LDA) can only result in small errors. Let us first focus on the question, which non-interacting external potential $v_s(x)$ has the same ground state density as the interacting system?

claim 3 *Given interaction $u(x, x')$ and external potential $v(x)$. If the variations of the ground state density $n_0(x) + \delta n_0(x)$ are interacting v-representable and non-interacting v-representable, the latter by $v_s(x) + \delta v_s(x)$, then*

$$v_s(x) = v(x) + \int dx' u(x, x') n_0(x') + v_{XC}[n_0](x) \ ; \ v_{XC}[n](x) = \frac{\delta E_{XC}[n]}{\delta n(x)}$$
$$(2.9)$$

proof 3 *First we use the Hohenberg Kohn theorem for the interacting system together with the assumption that the variations of the ground state density are interacting v-representable:*

$$\frac{\delta E[n]}{\delta n(x)}\bigg|_{n_0} \quad = \quad \frac{\delta F[n]}{\delta n(x)}\bigg|_{n_0} + v(x) \qquad (2.10)$$
$$= \quad v_{XC}[n_0](x) + \int dx' u(x, x') n_0(x') + \frac{\delta T_s[n]}{\delta n(x)}\bigg|_{n_0} + v(x) = 0$$

13

Next we use the Hohenberg Kohn theorem for the non-interacting system together with the assumption that the variations of the ground state density are non-interacting v-representable:

$$\left.\frac{\delta E_s[n]}{\delta n(x)}\right|_{n_0} = \left.\frac{\delta T_s[n]}{\delta n(x)}\right|_{n_0} + v_s(x) = 0 \tag{2.11}$$

substituting (2.11) into (2.10) completes the proof

The single particle potential (2.9), together with the single particle Schroedinger equation

$$H_s|\varphi_i\rangle = [-\frac{\hbar^2}{2m}\nabla^2 + v_s(x)]|\varphi_i\rangle = \varepsilon_i|\varphi_i\rangle \; ; \; \varepsilon_1 \leq \varepsilon_2 \leq ... \tag{2.12}$$

and the single particle density

$$n(x) = \sum_{i=1}^{N} |\langle x|\varphi_i\rangle|^2 \tag{2.13}$$

form the set of Kohn Sham equations from which the ground state density can be calculated self consistently.

In order to evaluate the exchange correlation potential, an approximation for the exchange correlation functional has to be made. In the local density approximation (LDA) the exchange correlation *functional* is approximated as an integral over the exchange correlation energy as a *function* of the local density.

$$E_{XC}^{LDA}[n] = \int dx n(x)\epsilon_{xc}(n(x)) \; , \tag{2.14}$$

where the local exchange correlation energy is taken to be that of the homogeneous electron gas. The derivation of the exchange correlation energy as a function of density goes well beyond the scope of this thesis, but nonetheless it is reassuring to see it in its explicit form [10]. The exchange energy of a homogeneous gas is known analytically:

$$\epsilon_{xc}(n) = \epsilon_x(n) + \epsilon_c(n) \; ; \; \epsilon_x(n) = -\frac{3}{4}\left(\frac{3}{\pi}\right)^{1/3} n^{1/3} \tag{2.15}$$

The correlation energy of the homogeneous electron gas is nearly exactly reproduced by the the parameterization of Perdew and Zunger [18] of the quantum monte carlo results of [19]:

$$\begin{aligned}
\epsilon_c(n) &= A \ln r_s + B + C r_s \ln r_s + D r_s \; ; \; \text{if } r_s < 1 \\
&= \gamma / \left(1 + \beta_1 \sqrt{r_s} + \beta_2 r_s\right) \; ; \; \text{if } r_s \geq 1
\end{aligned} \tag{2.16}$$

where r_s is the Wigner-Seitz radius defined as $r_s = (3/4\pi n)^{1/3}$.

The Kohn Sham orbitals φ_i in (2.12) so far have been introduced as mathematical objects which sole purpose is to calculate the density. Except for the highest occupied Kohn Sham orbital of a finite system, the energy of which equals the negative of the ionization energy [20], the Kohn Sham orbitals have not been proven to have physical meaning. Nonetheless it is common practice to interpret them as quasi-particles and the eigenvalues of the occupied/unoccupied Kohn-Sham orbitals as electron removal/addition energies. In this way the Kohn Sham energies have often been proven useful in comparing with Angular Resolved Photo Emission Spectroscopy (ARPES). Especially within the LDA approximation they are the number one choice for theoretically determining the Fermi surface for metallic systems, not necessarily limited to weakly correlated systems. Some recent investigations of correlated systems (for example, the heavily doped cuprates [21, 22] and the ferro-pnictides [23, 24] have shown that while the Kohn Sham energies might underestimate the effective mass of the bands, they still produce Fermi surfaces with correct size and shape. To a large extend the capability of the LDA to accurately describe the Fermi surfaces of metallic systems is warranted by the Luttinger theorem [25] which states that the volume of the Fermi surface is independent of interaction strength.

2.2 Linear Augmented Plane Waves

In order to calculate the Kohn Sham orbitals the Kohn Sham Hamiltonian H_s in (2.12) needs to be represented on a basis and transformed into a secular equation, that can be fed to a diagonalization routine. This basis does not need to be orthonormal. Given a basis $|a_i\rangle$ that is complete, but not orthog-

onal, there exists a dual basis $|b_i\rangle$ such that: $\sum_i |a_i\rangle\langle b_i| = 1$. By using this fact, which simply states that each complete basis can be represented as an invertible matrix, we can rewrite (2.12) into the secular equation:

$$\sum_j \underbrace{\langle a_i|H_s|a_j\rangle}_{H_{ij}}\langle b_j|\varphi_i\rangle = \epsilon_i \sum_j \underbrace{\langle a_i|a_j\rangle}_{S_{ij}}\langle b_j|\varphi_i\rangle \Leftrightarrow \left|H_{ij} - \epsilon_i S_{ij}\right| = 0 \qquad (2.17)$$
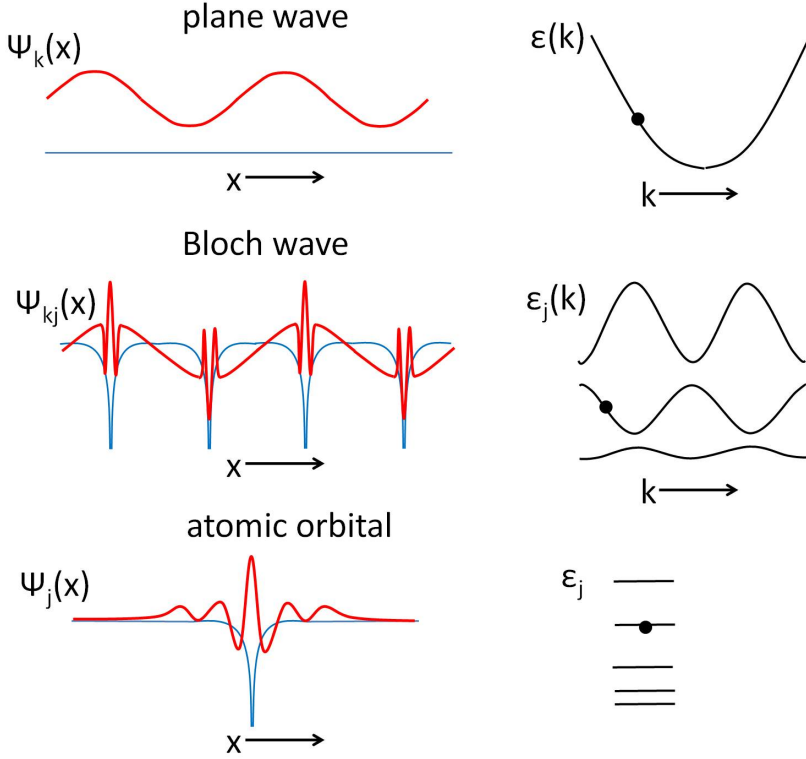
Figure 2.1: The dual character of the Bloch wave.

Now in order to decide which basis function to use it is necessary to know the nature of the Kohn Sham orbitals. In this thesis we will work with periodic external potentials $v(x) = v(x+r)$, which means that the Kohn Sham orbitals, of interest are Bloch waves.[2] On the one hand it is clear that nearby the atomic nuclei the diverging Coulomb potential will turn the Bloch wave into an atomic-like orbital. On the other hand, according to Bloch's theorem (which

---

[2]There is a subtlety here, namely that even for a periodic external potential, the translation symmetry can be broken spontaneously due to the non-linear nature of the Hartree and the exchange correlation potential. Physically such cases of spontaneous symmetry breaking correspond to the formation of charge and spin density waves or to orbital ordering [26, 27].

we will proof in just a minute), the Bloch wave will propagate in a plane wave like manner between the atoms. In figure 2.1 we sketch this dual character of the Bloch waves. Also their energy spectrum, the band structure, displays the dual character. On the one hand the Bloch wave energies are quantized with a band index, like the the energy levels in an atom. On the other hand the Bloch wave energies depends continuously on the crystal momentum like a free electron plane wave does on the plane wave momentum.

Since the Bloch waves are plane wave-like in nature, plane waves, defined as $|k + g\rangle = \int d^3x e^{-i(k+g)x}|x\rangle$, where $k \in$ brillouin zone and $g \in$ reciprocal lattice, make a very natural basis set. First off all it is convenient that plane waves are orthonormal (see appendix C), which reduces the overlap matrix to the unit matrix: $S_{k+g,k'+g'} = \delta_{k+g,k'+g'}$. But more importantly they respect the translational symmetry of the lattice and therefore block diagonalize the Hamiltonian.

claim 4 *Given a lattice Hamiltonian that commutes with the lattice translation operators $[H, T_r] = 0$, the plane waves states block diagonalize the lattice Hamiltonian*

$$\langle k' + g'|H|k + g\rangle = \delta_{k'k}\langle k + g'|H|k + g\rangle \tag{2.18}$$

proof 4 *The plane waves are eigenstates of the translation operator*

$$T_r|k + g\rangle = \int d^3x e^{i(k+g)x}|x + r\rangle = e^{-i(k+g)\cdot r}\int d^3x e^{i(k+g)x}|x\rangle = e^{-ikr}|k + g\rangle \tag{2.19}$$

Using $[H, T_r] = 0$ we find

$$\begin{aligned} e^{-ik'r}\langle k' + g'|H|k + g\rangle &= \langle k' + g'|T_rH|k + g\rangle \\ &= \langle k' + g'|HT_r|k + g\rangle = \langle k' + g'|H|k + g\rangle e^{-ikr} \\ \Leftrightarrow \quad k = k' &\text{ or } \langle \text{k}' + \text{g}'|\text{H}|\text{k} + \text{g}\rangle = 0 \end{aligned} \tag{2.20}$$

Incidentally here we also prove Bloch's theorem

claim 5 *The Bloch waves can be written as a plane wave e^{ikx} times a periodic*

function:

$$\langle x|kj\rangle = e^{ikx}u_{kj}(x) \; ; \; u_{kj}(x+r) = u_{kj}(x) \tag{2.21}$$

proof 5 *Since the lattice Hamiltonian is block diagonal per crystal momentum k the Bloch states are eigenvectors of the translation operator with eigenvalue*

$$T_r|kj\rangle = T_r\left(\sum_g c_g^{kj}|k+g\rangle\right) = e^{-ikr}|kj\rangle \tag{2.22}$$

from which it follows

$$e^{ik(x+r)}u_{kj}(x+r) = \langle x+r|kj\rangle = \langle x|T_r^\dagger|kj\rangle = e^{ikr}\langle x|kj\rangle = e^{ik(x+r)}u_{kj}(x) \tag{2.23}$$

So thanks to the crystal symmetry, the continuously infinite plane wave based Hamiltonian matrix (i.e. all crystal momenta k and all reciprocal vectors g) is reduced to a discrete but still infinite block per k-point (all g). Therefore in practice the number of plane waves needs to be cut off to a maximum reciprocal lattice vector g_{max}, which is possible, as long as the Bloch waves are smooth enough. The problem however is that realistic Bloch waves are not smooth. Although the Bloch waves oscillate slowly between the atoms, as the Bloch wave come near the diverging Coulomb potential of the atoms they start oscillating very rapidly (see figure 2.1). To overcome this problem the first step is to divide space into two regions. The first type of region is formed by spheres around the atomic nuclei called atomic muffin-tin regions. The remaining space is the interstitial region. One approach is to replace the core electron degrees of freedom and the diverging Coulombic potential in the atomic muffin-tin regions by a so-called pseudopotential [14], which is smooth everywhere allowing for finite amount of plane waves to describe the wave functions.

The other approach is to "augment" the plane waves in the atomic muffin-tin spheres in such a way that they can better describe the sharp oscillations of the Bloch waves induced by the diverging coulomb potentials of the atomic nuclei. Since calculations based on this approach do not sacrifice the core

electron degrees of freedom they are also known as "all electron" calculations. Historically the first type of these so-called augmented basis functions were the Augmented Plane Waves (APW) introduced by John C. Slater [28]. The APW is a plane wave within the interstitial region, but within the muffin-tin sphere S_α of atom α it is replaced by a linear combination of atomic orbitals :

$$
\begin{aligned}
\varphi_{k,g}^{APW}(x) & = (2\pi)^{-3/2} e^{ix(k+g)} \; ; \text{ if x} \notin \text{S}_\alpha \\
& = \sum_{lm} A_{\alpha lm}^{k+g} u_{\alpha l}(E_{\alpha l}, x) Y_{lm}(\theta, \phi) \; ; \text{ if x} \in \text{S}_\alpha
\end{aligned}
\tag{2.24}
$$

Here $u_{\alpha l}(E, x)$ are the radial wave functions that satisfy

$$
\left[-\frac{d^2}{dx^2} + \frac{l(l+1)}{x^2} + v_\alpha(x) \right] x u_{\alpha l}(E, x) = E x u_{\alpha l}(E, x)
\tag{2.25}
$$

where the radial potential $v_\alpha(x)$ is defined as the spherically averaged external potential around the center of atom α. The coefficients $A_{\alpha lm}^{k+G}$ are chosen in such a way that the APW is continuous at the muffin-tin boundary (see for example [12] for an explicit analytic expression), a necessary requirement for the expectation value of the kinetic energy to be well defined. The radial wave functions are not required to satisfy the boundary condition $\lim_{x \to \infty} u_{\alpha l}(x) \to 0$ and therefore the reference energies E are continuous parameters instead of quantized eigenvalues. The closer the reference energies are chosen to the band energy ε_{kj} the better the quality of the APW basis function becomes. Therein however lies precisely the disadvantage of the APW basis function namely that the eigenvalue ε_{kj} needs to be known a priori. This turns the eigenvalue problem into a non-linear problem. Furthermore a separate diagonalization is necessary for each band j which becomes especially a problem in the case of big super cells with many bands. This problem was overcome by O. K. Anderson [29] who extended the APW's to the Linear Augmented Plane Waves (LAPW). The basic idea is that since the radial functions continuously depend on the reference energies, they can be Taylor expended:

$$
u(\varepsilon_{kj}, x) = u(E, x) + (\varepsilon_{kj} - E)\dot{u}(E, x) + \mathcal{O}((\varepsilon_{kj} - E)^2)
\tag{2.26}
$$

By including a linear correction the basis function can still yield accurate

results even if the reference energy does not precisely equal the eigenenergy. Explicitly the LAPW is defined as:

$$
\begin{aligned}
\varphi_{k,g}^{LAPW}(x) &= (2\pi)^{-3/2}e^{ix(k+g)} \text{ ; if x} \notin S_\alpha & (2.27)\\
&= \sum_{lm}\left(A_{\alpha lm}^{k+g}u_{\alpha l}(E_{\alpha l},x) + B_{\alpha lm}^{k+g}\dot{u}_{\alpha l}(E_{\alpha l},x)\right)Y_{lm}(\theta,\phi) \text{ ; if x} \in S_\alpha
\end{aligned}
$$

Here $\dot{u}(E,x)$ are the energy derivatives of the radial wave functions whose determining equation is obtained by taking the energy derivative of (2.25):

$$
\left[-\frac{d^2}{dx^2} + \frac{l(l+1)}{x^2} + v_\alpha(x) - E\right]x\dot{u}_{\alpha l}(E,x) = xu_{\alpha l}(E,x) \qquad (2.28)
$$

The coefficients $A_{\alpha lm}^{k+g}$ and $B_{\alpha lm}^{k+g}$ are chosen in such a way that the LAPW and its spatial derivative are continuous at the muffin-tin boundary. Per definition, the radial wave functions are normalized within the muffin-tin radius r_{mt}:

$$
\int_0^{r_{mt}} dxx^2(u_{\alpha l}(E,x))^2 = 1 \Rightarrow \int_0^{r_{mt}} dxx^2u_{\alpha l}(E,x)\dot{u}_{\alpha l}(E,x) = 0 \qquad (2.29)
$$

where the last equation again simply follows from taking the energy derivative

Having defined the LAPW basis function, the Kohn Sham Hamiltonian can be cast into a secular equation (2.17). However, the explicit formulas for the LAPW-represented Hamiltonian and overlap matrix are very complex and far beyond the scope of this thesis (see for example Singh's book [13]). In stead let us make a few remarks. First of all, just like the plane waves, the LAPW's are eigenvectors of the translational operator: $T_r|\varphi_{k,g}^{LAPW}\rangle = e^{-ikr}|\varphi_{k,g}^{LAPW}\rangle$, meaning that they block diagonalize the Hamiltonian (and the overlap matrix, since of course $[T_r, 1] = 0$). Second, unlike the plane waves, the LAPW basis functions are non-orthonormal, meaning that the overlap matrix will not be the simple unit matrix. Third off all, although the single particle potential was spherically averaged in order to construct the basis function, the full non-spherical single particle potential is still included in the LAPW based Hamiltonian. Fourth, when the Bloch states $|kj\rangle$ are represented on the LAPW basis function, the atomic character of the band can be illustrated by projecting them onto the spherical Harmonics Y_{lm} in the muffin-tin sphere of

20

atom α:

$$\langle\alpha lm|kj\rangle = \sum_{g\alpha} c_j^{kg} \left(A_{lm\alpha}^{kg} + B_{lm\alpha}^{kg} \int_0^{r_{mt}} dx x^2 (\dot{u}_{\alpha lm}(x, E_{l\alpha}))^2 \right) \qquad (2.30)$$

An example of such a character plot that is produced with WIEN2K [30] is given in figure 2.2. Fifth, we have not discussed the other three LAPW-like basis functions LAPW+LO, APW+lo and the APW+lo+LO, that are part of the WIEN2K package. Their definition and properties are discussed for example in [12]. Finally we should remark that the LAPW is accepted to be the most accurate and general basis function for calculating the electronic structure at present time [14]. Probably less common knowledge is that the LAPW basis function is also very suitable for the construction of projected Wannier functions, which brings us to the next section.

2.3 Wannier Functions

The first principles Wannier function is becoming an increasingly important tool with applications all over electronic structure theory. Wannier functions can be used to obtain the band structure on a very fine k-mesh (Wannier-interpolation) which allows for accurate calculations of the Fermi-surface or the electron-phonon coupling [31]. Wannier functions can be used for calculating from first principles the Berry phase and related quantities such as electrical polarization [32] or orbital magnetization [33]. Wannier functions can be used to extract a simple physical insight from the complex output of first principles calculations [34]. Wannier functions can be used to calculate the formfactor [35] or transport properties [36]. Probably Wannier functions are most frequently used as a basis set for the low energy Hilbert space, which can serve as a starting point for more rigorous treatments of correlation beyond the Kohn Sham approximation, for example for dynamical mean field theory (DMFT) [37, 38], slave boson mean field theory [39], time-dependent density functional theory [40], renormalization group techniques [41] or the Gutzwiller method [42]. The technology developed in this thesis, designed to treat the influence of disorder from first principles, is yet another example in the long list of applications of first-principles Wannier functions.

Having motivated the importance of the first principles Wannier functions, let us now state what they are. Given the Bloch states $|kj\rangle$ corresponding to a set of bands ε_{kj}, one can construct a set of Wannier states $|rn\rangle$ according to

$$|rn\rangle = \frac{1}{\sqrt{l}} \sum_k e^{-ik\cdot r}|kn\rangle \; ; \; |kn\rangle = \sum_j |kj\rangle U_{jn}(k) \tag{2.31}$$

where l denotes the number of unit cells in the system, r denotes the lattice vector and n denotes the Wannier orbital index. The $|kn\rangle$ are what we shall refer to as "k-states" and are in fact nothing but the lattice Fourier transform of the Wannier states. One of the very important properties of the Wannier functions is that they are exponentially localized. Intuitively we can imagine why this is the case, since the Wannier transformation (2.31) is similar to a Fourier transformation and since the Bloch states are similar to a plane wave. The exponential decay was proven for 1 dimensional systems by Walter Kohn [43] and for 2 or 3 dimensions it was found to be true if and only if the Chern number(s) are zero [44, 45]. The gauge of the Wannier functions is set by the unitary matrix $U_{nj}(k)$ and can be chosen freely. A famous choice of the gauge results in the so called Maximally Localized Wannier Functions [46], for which the spread of the Wannier functions, $\sum_n \langle rn|x^2|rn\rangle - |\langle rn|x|rn\rangle|^2$, is minimized. In this thesis we fix the gauge by using the projected Wannier function method [37, 47].

2.3.1   Definition of the LAPW-Based Projected Wannier Function

In this subsection we shall describe Wei Ku's recipe [47] for the LAPW-based projected Wannier function which has been implemented for WIEN2K [30] and applied in the first principles studies of real materials [26, 27, 34, 35, 40, 41]. The basic idea of the projected Wannier functions is to define them as the lattice Fourier transform of the projection of n_{orb} orbitals $|\varphi_n\rangle$ onto the Bloch states of $n_{\text{band}}(\geq n_{\text{orb}})$ bands: $\sum_{kj} e^{ikr}|kj\rangle\langle kj|\varphi_n\rangle$. However, since the projections $\sum_j |kj\rangle\langle kj|\varphi_n\rangle$ are not orthonormal, neither will be their lattice Fourier transform. The idea is then to exploit the gauge freedom to orthonormalize the projections according to Lödwin's symmetric orthonormalization prescription

(see for example [48]):

$$|kn\rangle = \sum_{jn'} |kj\rangle\langle kj|\varphi_{n'}\rangle M_{n'n}(k) \tag{2.32}$$

where the matrix $M_{n'n}(k)$ is the inverse square root of the overlap matrix of the projections:

$$M_{n'n}^{-2}(k) = \left(\sum_{j'}\langle\varphi_{n'}|kj'\rangle\langle kj'|\right)\sum_{j}|kj\rangle\langle kj|\varphi_n\rangle = \sum_{j}\langle\varphi_n|\psi_{kj}\rangle\langle\psi_{kj}|\varphi_{n'}\rangle \tag{2.33}$$

By choosing the projected orbitals according to the atomic character of the bands, one can obtain localized Wannier functions, that for practical purposes are as localized as the Maximally Localized Wannier Functions. Having the Bloch states represented on a local basis set, such as the LAPW basis, this choice is greatly facilitated. Focusing on the LAPW basis function we shall now state the recipe for picking the atomic orbitals explicitly. Given the LAPW basis function defined in (2.27) the orbitals $|\varphi_n\rangle$, that will be projected on to the Bloch states are chosen to be:

$$\langle x|\varphi_n\rangle = \sum_{\alpha lm} d^n_{\alpha lm} u_{\alpha l}(x, E_{\alpha l}) Y^l_m(x) \text{ if } x \in S_\alpha \; ; \; \langle x|\varphi_n\rangle = 0 \text{ if } x \notin S_\alpha \tag{2.34}$$

The definition of the Wannier function is is given by the coefficients $d^n_{\alpha lm}$.

2.3.2 The Tight Binding Hamiltonian

Having defined the Wannier functions in terms of the coefficients $d^n_{\alpha lm}$ the tight binding Hamiltonian can be obtained from rotating the eigenvalues:

$$\langle r'n'|H|0n\rangle = \sum_{kj}\langle r'n'|kj\rangle\varepsilon_{kj}\langle kj|0n\rangle \tag{2.35}$$

where the rotation matrix depends on the product of the projected orbital and the Bloch state

$$\langle rn|kj\rangle = \sqrt{1/l}e^{ikr}\sum_{n'}M_{nn'}(k)\langle\varphi_{n'}|kj\rangle \; ; \; M_{nn'}^{-2}(k) = \sum_{j'}\langle\varphi_n|kj\rangle\langle kj|\varphi_{n'}\rangle \tag{2.36}$$

which is in turn reduces to a trace of the LAPW coefficients c_g^{kj} and $A_{lm\alpha}^{kg}$ and the Wannier definition coefficient $d_{lm\alpha}^n$:

$$
\begin{aligned}
\langle \varphi_n | kj \rangle &= \left(\sum_{lm} d_{\alpha lm}^n \langle u_{\alpha l}(E_{\alpha l}) | \langle Y_{lm} | \right) \times \\
&\quad \left(\sum_{gl'm'} c_g^{kj} \left(A_{\alpha'l'm'}^{k,g} | u_{\alpha'l'}(E_{\alpha'l'}) \rangle + B_{\alpha'l'm'}^{k,g} | \dot{u}_{\alpha l}(E_{\alpha'l'}) \rangle \right) | Y_{l'm'} \rangle \right) \\
&= \sum_{glm\alpha} d_{lm\alpha}^n c_g^{kj} A_{lm\alpha}^{kg}
\end{aligned}
\tag{2.37}
$$

where in the last equation we used the properties of the radial wave functions (2.29).

2.3.3 Example TaSe2

The Wannier functions constructed in this example have been used to explain the experimentally observed gapless charge density wave [34]. However, here we shall not be concerned with the physics of $TaSe_2$, rather we will use the $TaSe_2$ Wannier functions to illustrate the technique of LAPW-based projected Wannier functions.

In the left side of figure 2.2 we see the lattice structure of $TaSe_2$. It consists of a triangular sheet of Ta atoms sandwiched between two triangular sheets of Se atoms. In the previous section we mentioned that the projected orbitals, from which the Wannier functions are constructed, should be chosen according to the atomic character of the band. When the Bloch states $|kj\rangle$ are represented on the LAPW basis function, the atomic character can be illustrated using 2.30. In figure 2.2 the bandstructure of $TaSe_2$ in which the atomic characters are represented by the radius of the colored circles. The red circles correspond to the Ta-d_{xz}/Ta-d_{yz} character, the blue circles to the Ta-$d_{x^2-y^2}$/Ta-d_{xy} character and the black circles to the Ta-d_{z^2} character. From this character plot we learn that the two bands around the Fermi surface are mostly Ta-d_{z^2} character, although in certain parts of the Brillouin zone, around the high symmetry points K and H, the character is Ta-$d_{x^2-y^2}$/Ta-d_{xy}. Therefore, if we want to construct the Wannier functions of these two bands that are as localized as possible, we should use Ta-d_{z^2} as the projected orbitals.
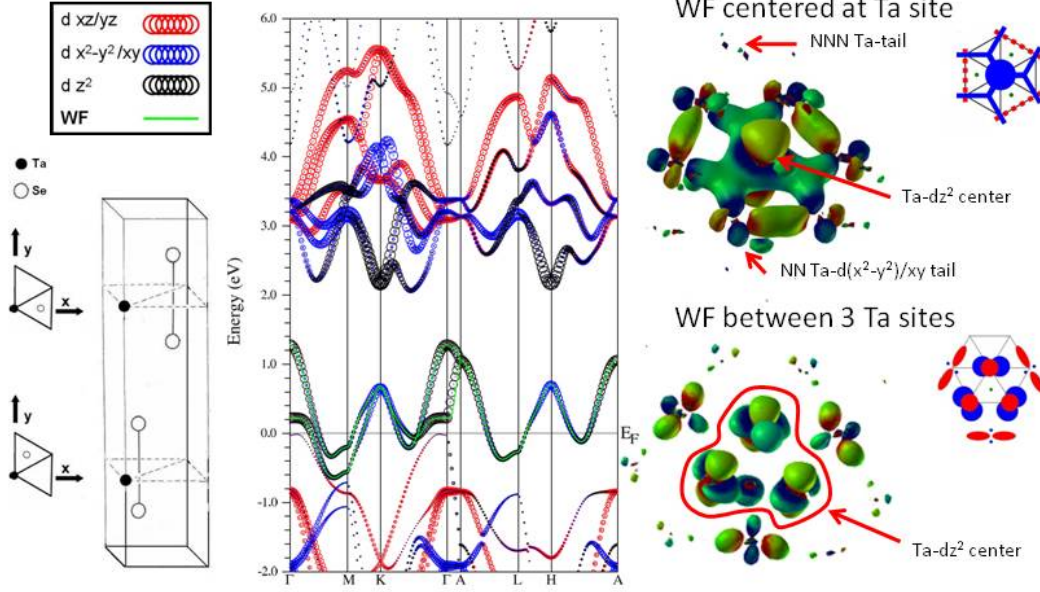
Figure 2.2: (Left) Unit cell of TaSe$_2$ (Middle) Band structure plot produced with WIEN2K [30], in which the radius of the colored circles corresponds to the atomic characters denoted in the upper left corner. (Right) Example of realistic Wannier functions of TaSe$_2$.

In the upper right corner of 2.2 the isosurface of the Wannier function is plotted that is constructed of a single Ta-d_{z^2} orbital. The color of the isosurface corresponds to the gradient of the Wannier function and can be ignored except for the fact that the blue-green corresponds to a negative sign and red-yellow to a positive sign of the Wannier function. (See also the cartoon of the Wannier function on the right as a guidance). The Wannier functions clearly reflect the atomic characters of the bands. The Ta-d_{z^2} character, by construction, is concentrated in the center of the Wannier function at the Ta site and the Ta-$d_{x^2-y^2}$/Ta-d_{xy} character is concentrated in the tails of the Wannier function at the nearest neighboring(NN) Ta sites. The weight in the next nearest neighboring (NNN) Ta site is exponentially suppressed.

Under the constraint of using the Ta-d_{z^2} character, there is still the freedom to take any kind of linear combination of Ta-d_{z^2} orbitals located at different sites. For example the Wannier function in the lower right of 2.2, is constructed

25

by projecting on

$$\sqrt{1/3}\Big(|\mathrm{Ta-d_{z^2}}, \mathrm{r} = (0,0)\rangle + |\mathrm{Ta-d_{z^2}}, \mathrm{r} = (1,0)\rangle + |\mathrm{Ta-d_{z^2}}, \mathrm{r} = (1,1)\rangle\Big)$$

The center of the Wannier function in this case is located between the Ta-sites. This kind of freedom can be used for example to construct bonding and anti-bonding Wannier states, which are more intuitive in covalent systems or the superatom [41], which can serve as a building block for including inter atomic correlations.

Depending on what gauge we chose we will get different tight binding Hamiltonians according to the formulas (2.35)-(2.37). However, as long as the Wannier functions are sufficiently localized they will all practically have the same band structure. Furthermore as long as the number of bands is equal to the number of Wannier functions, as is the case in this example, the Wannier band structure will reproduce the DFT band structure perfectly, as can been seen for the case of $TaSe_2$, by noticing that the green band structure corresponding to the Wannier functions, is on top of the DFT band structure.

Finally let's contrast the delocalized Ta-d_{z^2} Wannier functions in figure (2.2) with the atomic-like cobalt and oxygen Wannier functions in CoO_2 in figure 4.2 of chapter 4. The general rule of thumb is that the more bands that are included in the Wannier transformation, the more localized the Wannier functions get. The Ta-d_{z^2} Wannier functions were constructed out of 1 band per Ta atom and consequently spreads out to its nearest neighboring Ta atoms. The cobalt and oxygen Wannier functions in 4.2 are constructed out of the full Co-d and O-p band complex as a result of which they are extremely localized.

2.3.4 Respecting the Symmetry

One of the great advantages of the projected Wannier functions is that they respect the symmetry of the Hamiltonian. For example lets look back at the Ta-d_{z^2} Wannier functions in figure 2.2. The symmetry group of $TaSe_2$ include for example a mirror in the Ta plane, and rotation over $2\pi/3$. Under these symmetry operations the Ta-d_{z^2} Wannier function will transform into themselves, just like the projected $|z^2\rangle$ orbital from which the Wannier function was constructed. The center of the Wannier function, by construction, will be

$|z^2\rangle$-like and therefore could be expected to transform in the same way, but it is truly amazing that the NN-Ta tails, even though locally of $d_{x^2-y^2}$ character, together combine in a non-trivial way to also respect the symmetry properties of $|z^2\rangle$. For simplicity we will now prove the symmetry respecting property only for the special case of non-degenerate bands and point group symmetry operators, but keeping in mind that it holds in general. First we need to establish how a Bloch state will transform.

claim 6 *Given a point group symmetry operator S that commutes with the Hamiltonian $[H, S] = 0$ and given the Bloch states $|kj\rangle$, of a set non-degenerate bands ϵ_{kj}, which without loss of generality are chosen to have the same phase at the origin, then $S|kj\rangle = |Sk, j\rangle$.*

proof 6 *First off all $S|kj\rangle$ is a Bloch state with band index j, since*

$$HS|kj\rangle = S(H|kj\rangle) = S(\epsilon_{kj}|kj\rangle). \tag{2.38}$$

Second we establish that $T_r S = S T_{S^T \cdot r}$, from

$$T_r S|x\rangle = |S \cdot x + r\rangle = S|x + S^{-1} \cdot r\rangle = S T_{S^{-1} \cdot r}|x\rangle = S T_{S^T \cdot r}|x\rangle. \tag{2.39}$$

From which find

$$T_r S|kj\rangle = S T_{S^T \cdot r}|kj\rangle = e^{ik \cdot (S^T r)} S|kj\rangle = e^{i(Sk) \cdot r} S|kj\rangle, \tag{2.40}$$

which completes the proof since the bands were assumed non-degenerate.

claim 7 *Given a point group symmetry operator S that commutes with the Hamiltonian $[H, S] = 0$ under which the projected orbital $|n\rangle$ transforms as:*

$$S|n\rangle = \sum_{n'} |n'\rangle S_{n'n} \tag{2.41}$$

Then the projected Wannier state $|rn\rangle$, constructed from a set of non-degenerate Bloch states $|kj\rangle$, transforms as:

$$S|rn\rangle = \sum_{n'} |Sr, n'\rangle S_{n'n} \tag{2.42}$$

27

proof 7

$$
\begin{aligned}
S|rn\rangle &= \frac{1}{\sqrt{l}} \sum_{kj} |S \cdot kj\rangle \sum_{n'} \langle kj|n'\rangle M_{n'n}(k) e^{-ik \cdot r} \\
&= \frac{1}{\sqrt{l}} \sum_{kj} |kj\rangle \sum_{n'} \langle S^T k, j|n'\rangle M_{n'n}(S^T k) e^{-i(S^T k) \cdot r} \\
&= \frac{1}{\sqrt{l}} \sum_{kj} |kj\rangle \sum_{n'} \langle kj|S|n'\rangle M_{n'n}(S^T k) e^{-ik \cdot Sr} \\
&= \frac{1}{\sqrt{l}} \sum_{kj} |kj\rangle \sum_{n',n''} \langle kj|n''\rangle S_{n''n'} M_{n'n}(S^T k) e^{-ik \cdot Sr} \\
&= \frac{1}{\sqrt{l}} \sum_{kj} |kj\rangle \sum_{n''} \langle kj|n''\rangle [SM(S^T k)]_{n''n} e^{-ik \cdot Sr} \qquad (2.43)
\end{aligned}
$$

Next we work on the overlap matrix:

$$
\begin{aligned}
M_{n'n}^{-2}(S^T k) &= \sum_j \langle n'|S^T kj\rangle \langle S^T kj|n\rangle \\
&= \sum_{n''n'''} \sum_j S_{n'n''}^T \langle n''|kj\rangle \langle kj|n'''\rangle S_{n'''n} \\
&= [S^T M(k) S]_{n'n} \qquad (2.44)
\end{aligned}
$$

From which it follows:

$$
\begin{aligned}
& M^{-2}(S^T k) = S^T M^{-2}(k) S \\
\Rightarrow \quad & M^2(S^T k) = S^T M^2(k) S = S^T M(k) S S^T M(k) S \\
\Rightarrow \quad & M(S^T k) = S^T M(k) S \\
\Rightarrow \quad & SM(S^T k) = M(k) S \qquad (2.45)
\end{aligned}
$$

Plugging this we find

$$
\begin{aligned}
S|rn\rangle &= \frac{1}{\sqrt{l}} \sum_{kj} |kj\rangle \sum_{n'} \langle kj|n'\rangle [M(k)S]_{n'n} e^{-ik \cdot Sr} \\
&= \sum_{n''} \frac{1}{\sqrt{l}} \sum_{kj} |kj\rangle \sum_{n'} \langle kj|n'\rangle M(k)_{n'n''} S_{n''n} e^{-ik \cdot Sr} \\
&= \sum_{n''} |Srn''\rangle S_{n''n} \qquad (2.46)
\end{aligned}
$$

Chapter 3

Methods: Wannier Function Based First-Principles Methods for Disordered Systems

In this chapter we present two newly developed Wannier function based methods that facilitate the supercell approximation for disorder systems. In section 3.2 we present the unfolding method which has been published in reference [49]. It should be noted that the unfolding method also has an important application for systems with periodic impurities or spontaneous symmetry breakers such as charge density waves and orbital orderings. It should also be noted that for the application to disordered systems, work in parallel has been done [50]. In section 3.3 we present the effective Hamiltonian method which has been published in reference [51]. Additional technical details and examples of the methods presented in this chapter are given in appendices A-F.

3.1 Super Cell Approximation for Disordered Systems

The goal of this thesis is to compute the band structure of disordered systems from first principles within the quasiparticle interpretation of the Kohn Sham orbitals. Specifically we are interested in disordered dopants such as substitutions, interstitials and vacancies (see figure 1.2). These kind of disorders

are also known as cellular disorders because there is still an underlying lattice present. In the case of the crystalline materials, the Kohn Sham eigenstates and eigenvalues could be obtained because the lattice translational symmetry allowed the Kohn Sham Hamiltonian to be block diagonalized. For disordered systems, cellular or not, the Kohn Sham Hamiltonian is no longer block diagonal and therefore cannot be solved without making an approximation.

Roughly speaking there are two ways of studying the band structure of cellular disordered systems from first principles. Either within the supercell approximation or within a mean-field approximation [52, 53]. A combination of these approaches, a so-called cluster mean field approximation, is also possible. The general idea behind the mean-field methods is to replace the disordered system with an effective site-averaged medium. A very often used mean-field method is the Virtual Crystal Approximation (VCA) in which the external potential of the disordered impurities is replaced by its site-averaged potential called the virtual crystal. For example suppose that a fraction x of the atoms with potential V_A are randomly substituted with impurities with potential V_B, then the virtual crystal potential would be: $\langle V \rangle = (1 - x)V_A + (x)V_B$. The great advantage of the VCA is that it has a low computational expense. Since the virtual crystal potential is the same at each site, the VCA restores the lattice symmetry and therefore makes the Kohn Sham Hamiltonian block diagonal again. However, for the same reason, the VCA misses one of the most important aspects of disorder, namely scattering.
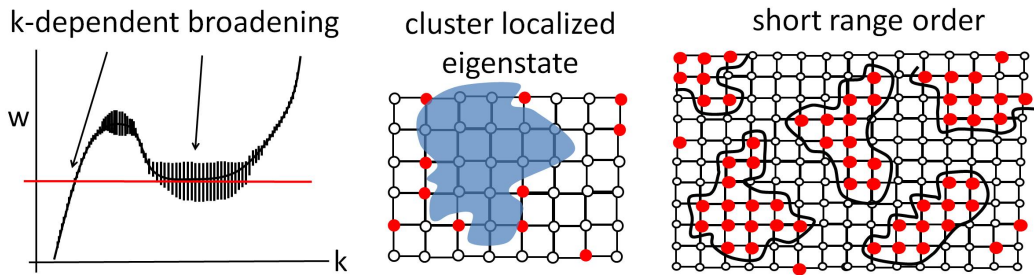
Figure 3.1: Three examples of non-local disorder effects.

In the Coherent Potential Approximation (CPA) the local Green's function is site averaged self-consistently: $\langle G^{00} \rangle = (1 - x)G_A^{00} + (x)G_B^{00}$. In appendix I we work out the CPA equations for the most simple case of a 1 dimensional 1

30

band model with binary disorder. The CPA is computationally more expensive then the VCA but does incorporate the single site scattering of the impurities. However, by construction, it can not incorporate any non-local influence of disorder that goes beyond one site. In figure 3.1 we illustrate three typical examples of non-local effects in disordered systems. The disorder induced self-energy can be bigger than one site, resulting in a crystal momentum dependent broadening of the bands. A cluster of impurities can trap eigenstates whose size can be much bigger then a single site. The impurities can be short range ordered, with a correlation length that spans over many sites.
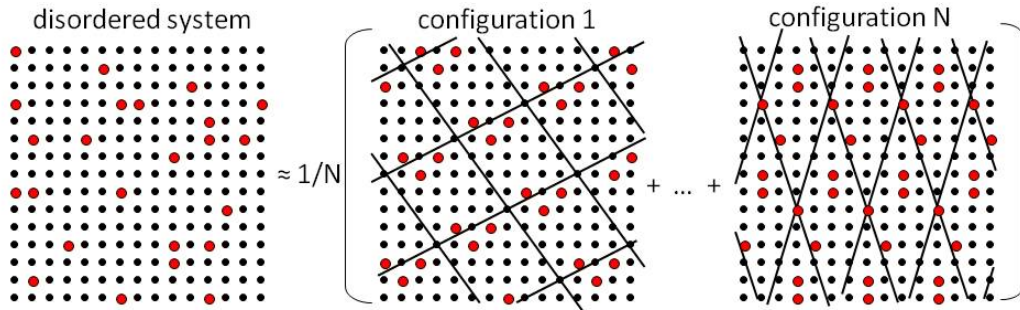
Figure 3.2: The super cell approximation.

Such non-local effects of disorder can be studied within the super cell approximation of disorder. In this approximation the disordered system is replaced by a large supercell in which a number of impurities are randomly distributed. The super cell approximation is conceptually a clean way to treat the disordered systems because it can be systematically converged as a function of the size of the supercell. In addition an average over multiple supercell configurations can be used in order to faster reach the convergence (see figure 3.2). Note that in this configurational average it will be desirable to not only randomly distribute the impurities within the supercells, but also to change the size, shape and orientation of the supercells themselves. In this way the artificial periodic boundary conditions of the supercell will be washed out more efficiently. In practice using the super cell approximation for calculating the band structure suffers from two problems: the band folding and the computational expense. In this chapter we will present two Wannier function based methods to overcome these problems.

3.2 Unfolding

The electronic band structure is the eigenvalue of ε_{kj} of a Bloch wave $\langle x|kj\rangle$ as a function of crystal momentum k. Here crystals momentum plays two roles. One the one hand the crystal momentum is a conserved quantum number, corresponding to the translational symmetry of the Hamiltonian. As we have already been discussing, the Hamiltonian can be block diagonalized if a basis set is used that conserves the crystal momentum (e.g. plane waves or LAPW's).

On the other hand the crystal momentum plays a crucial role in extracting physical insight from the first principles calculations. For example within semi-classical model of electrodynamics, the crystal momentum is the momentum of the semi-classical particles, when considering dynamical response to external electromagnetic field. The semiclassical picture allows the band structures to be connected with experimental electronic and optical properties such as ac and dc electrical conductivity,thermal conductivity, thermoelectric effects(Nernst, Peltier, thermopower), Hall effect, magnetoresistance, quantum oscillations (Shubnikov-de Haas and De Haas-van Alphen) [54]. In metals, the crystal momentum resolved Fermi surface can be used to study Fermi surface nesting, a mechanism responsible for many types of phase transitions such as superconductivity, charge density waves, spin density waves and structural phase transitions. In semi-conductors, depending on whether the conduction band minimum and the valence band maximum occur at the same crystal momentum or not, the bandgap will be either direct or indirect, the difference of which has dramatic consequences for the absorption of light. Last but not least, within the quasi-particle interpretation of the Kohn Sham orbitals, the band structure as a function of crystal momentum, can be directly related to the Angular Resolved Photo Emission Spectroscopy.

If the translational symmetry of the normal cell is broken by the presence of a super lattice of impurities, only the crystal momenta in the supercell Brillouin zone remain good quantum numbers. Bands outside of the supercell Brillouin zone will be folded into the smaller Brillouin zone. The situation is illustrated in figure 3.3, for the case of a 1 dimensional 1 band tight binding model. Substituting one out of every two atoms for an impurity, results in the supercell that is twice as big as the normal cell. Consequently the Brillouin
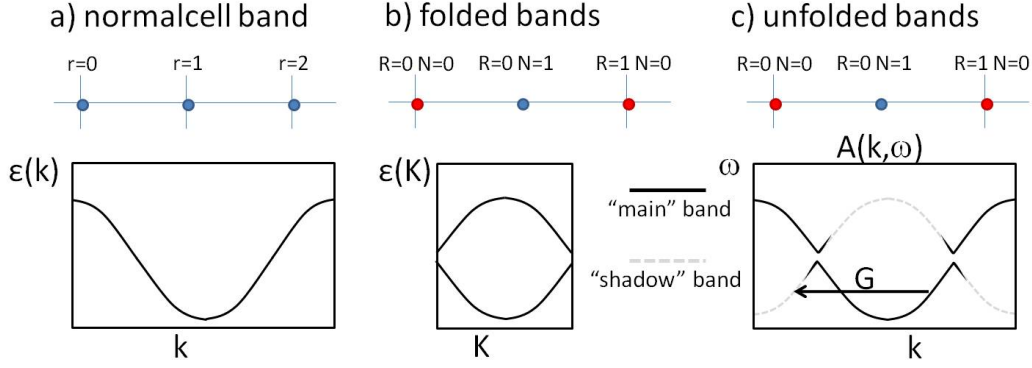
Figure 3.3: Cartoon of folding and unfolding for the case of a 1 dimensional 1 band tight binding model.

zone of the supercell gets twice as small as the normal cell Brillouin zone meaning that half of the original bands will be folded thereby doubling the number of bands per k-point.

Unfortunately the usefulness of the crystal momentum resolved band structure breaks down due to the band folding. If we keep increasing the size of the supercell, more and more bands will be folded into a smaller and smaller Brillouin zone. This is a big problem because in this thesis we are interested in supercells that contain hundreds of normal cells. For such big supercells the band structure would be nothing but a collection of small horizontal lines pilled on top of each other. It is clear that from such a dispersionless band structure no physical insight related to the crystal momentum can be extracted.

3.2.1   The Spectral Function

The resolution of the bandfolding problem is to realize that even though the normal cell crystal momentum k is not conserved, it is still possible to quantify its probability. Technically this can be accomplished by computing the diagonal[1] elements of the spectral function on the basis of the normal cell

---

[1]Focusing on the diagonal normal cell k-state basis is equivalent in real space with taking the average over lattice sites:

$$\langle kn|G(\omega)|kn\rangle = \frac{1}{l}\sum_{r,r'}e^{-ik(r-r')}\langle rn|G(\omega)|r'n\rangle = \sum_{r''}e^{-ikr''}\underbrace{\frac{1}{l}\sum_{r'}\langle r''+r'n|G(\omega)|r'n\rangle}_{\text{site}-\text{average}} \quad (3.1)$$

crystal momentum, which in this thesis we shall simply refer to as the spectral function. The goal is to calculate the spectral function given the Bloch states $\langle KN|KJ \rangle$ on the supercell K-basis and supercell band structure ε_{KJ}. We start by writing the spectral function as the imaginary part of the Green's function operator evaluated on the basis of the normal cell crystal momentum k and Wannier index n:

$$A_n(k,\omega) = -\frac{1}{\pi}\text{Im}\langle kn|G(\omega)|kn\rangle \ ; \ G(\omega) = (\omega - H + i0^+)^{-1} \tag{3.2}$$

where $|kn\rangle$ is the normal cell k-state which is the lattice Fourier transform of the normal cell Wannier state $|rn\rangle$ (see (2.31)). As we shall see the k-state $|kn\rangle$ does not need to be computed explicitly when assuming that the Wannier functions do not change under the influence of the impurities. By inserting the completeness relation of supercell Bloch states $|KJ\rangle$ the spectral function can be rewritten as:

$$A_n(k,\omega) = -\frac{1}{\pi}\text{Im} \sum_{KJ} |\langle kn|KJ\rangle|^2 \langle KJ|G(\omega)|KJ\rangle \tag{3.3}$$

The spectral function is diagonal on the basis of the supercell Bloch states and reduces to:

$$A_{KJ,KJ}(\omega) = -\frac{1}{\pi}\text{Im}\langle KJ|G(\omega)|KJ\rangle = -\frac{1}{\pi}\text{Im}\frac{1}{\omega - \varepsilon_{KJ} + i0^+} = \delta(\omega - \varepsilon_{KJ}) \tag{3.4}$$

So we can rewrite the spectral function in the form:

$$A_n(k,\omega) = \sum_{KJ} |\langle kn|KJ\rangle|^2 \delta(\omega - \varepsilon_{KJ}) \tag{3.5}$$

which confirms that it quantifies the probability of normal crystal momentum k at frequency ω. The overlap matrix element reduces to a structure factor:

$$
\begin{aligned}
\langle kn|KJ\rangle &= \sum_{RNr}\langle kn|rn\rangle\langle rn|RN\rangle\langle RN|KN\rangle\langle KN|KJ\rangle \\
&= \sum_{RNr}\Big(\frac{1}{\sqrt{l}}e^{-ikr}\Big)\Big(\delta_{r,R+r'(N)}\delta_{nn'(N)}\Big)\Big(\frac{1}{\sqrt{L}}e^{iKR}\Big)\langle KN|KJ\rangle \\
&= \sum_{RN}\Big(\frac{1}{\sqrt{l}}e^{-ik(R+r'(N))}\Big)\Big(\delta_{nn'(N)}\Big)\Big(\frac{1}{\sqrt{L}}e^{iKR}\Big)\langle KN|KJ\rangle \\
&= \sqrt{\frac{L}{l}}\sum_{N}\Big(\frac{1}{L}\sum_{R}e^{iR(K-k)}\Big)e^{-ikr'(N)}\delta_{nn'(N)}\langle KN|KJ\rangle \\
&= \sqrt{\frac{L}{l}}\sum_{N}\Big(\sum_{G}\delta_{k,K+G}\Big)e^{-ikr'(N)}\delta_{nn'(N)}\langle KN|KJ\rangle \qquad (3.6)
\end{aligned}
$$

Here $r'(N)$ is the normal cell lattice index of supercell orbital N within the zeroth supercell. The relationship between the normal cell and supercell coordinates is given by what we in this thesis refer to as "the map" (see appendix B). Note that in the second equation we made an assumption, namely that $\langle rn|RN\rangle = \delta_{r,R+r'(N)}\delta_{nn'(N)}$. To put it in words, we assumed that the Wannier function did not change under the influence of the impurity. We will come back to this important issue in section 3.3.2. All in all we find the spectral function $A_n(k,\omega)$ to be the product of the supercell band structure $\delta(\omega - \varepsilon_{KJ})$ unfolded to the normal cell Brillouin zone according to $\delta_{k+G,K}$ and weighted by the sum of the components of the eigenvector $\langle KN|KJ\rangle$ modulated by the phase $e^{-ikr'(N)}$. As we mentioned before the assumptioned $\langle rn|RN\rangle = \delta_{r,R+r'(N)}\delta_{nn'(N)}$ allowed for the evaluation of $A_n(k,\omega)$ without calculating $|kn\rangle$ explicitly.

Lets go back to the example of the 1 dimensional 1 band tight binding model illustrated in figure 3.3(c). The first step is to translate the supercell band structure eigenvalues ε_{KJ} in the supercell Brillouin zone over each supercell reciprocal vector G in the normal cell Brillouin zone. Then the next step is to multiply the intensity of the band with the spectral weight (3.6). As the cartoon suggests, if the symmetry breaking impurity potential is not to strong, the weight will be such that the "main" bands will have almost a full intensity and the "shadow" bands will have almost zero intensity except

around the gapopenings. In appendix D we will work out the example of the 1 dimensional 1 band tight binding model mathematically. Especially the figures D.1 and D.2 are instructive. The "shadow bands" and the gapopenings together provide quantitative information about the coupling of the translational symmetry breaking potential to the normal cell Bloch states.

From the completeness of the supercell Bloch states $|KJ\rangle$ we can easily proof the following sum rule:

claim 8

$$\int d\omega A_n(k,\omega) = 1 \tag{3.7}$$

proof 8

$$\int d\omega A_n(k,\omega) = \int d\omega \sum_J |\langle kn|KJ\rangle|^2 \delta(\omega - E_{KJ})$$

$$= \sum_J |\langle kn|KJ\rangle|^2 = \sum_J \langle kn|KJ\rangle\langle KJ|kn\rangle = \langle kn|kn\rangle = 1 \tag{3.8}$$

The spectral function $A_n(k,\omega)$ has an important direct connection to the ARPES measurement. Within the "one-step model", the ARPES intensity is proportional to [55]

$$\sum_{KJ} |\mathbf{e}\cdot\langle f|\mathbf{p}|KJ\rangle|^2 A_{KJ,KJ}(\omega)$$

$$\sim \sum_{KJkn} |\mathbf{e}\cdot\langle f|\mathbf{p}|kn\rangle|^2 |\langle kn|KJ\rangle|^2 A_{KJ,KJ}(\omega)$$

$$= \sum_{kn} |\mathbf{e}\cdot\langle f|\mathbf{p}|kn\rangle|^2 A_n(k,\omega) \tag{3.9}$$

where $\mathbf{e}$ denotes the polarization vector of light, and $|f\rangle$ the "final state" of the photo electron. Except the non-diagonal elements $\langle kn|A(\omega)|k'n'\rangle$ and the polarization dependent dipole matrix element, $|\mathbf{e}\cdot\langle f|\mathbf{p}|kn\rangle|^2$, the unfolded spectral function, $A_n(k,\omega)$, contains almost the full information of the experimental spectrum by absorbing the additional structure factor $\langle kn|KJ\rangle$. The inclusion of this additional matrix element facilitates the comparison between the theory and the ARPES experiment.

3.2.2 Technical Details of Plotting the Spectral Function

For the purpose of visualization an artificial broadening η is introduced according to $\delta(\omega - \epsilon_{KJ}) \approx (\eta/\pi)((\omega - \epsilon_{KJ})^2 + \eta^2)^{-1}$, in such a way that the sum rule (3.7) is conserved. The Wannier orbital resolved spectral function is presented on a color bitmap consisting of a $n_\omega \times n_k$ pixel grid. The RGB value of each pixel is taken to be the complement of $(\eta\pi)\sum_n A_n(k,\omega)c_n$ (such that the background appears white), where c_n is the RGB value designated to Wannier orbital n. In figure 3.4 we compare the Wannier orbital resolution of the k-dependent spectral function $A_n(k,\omega)$ (figure 3.4(a)) with the exact decomposition in the constant $k = k_0$ spectral function $A_n(k = k_0, \omega)$ (3.4(b)), for Co_2O_4. The corresponding plotting parameters are summarized in table 3.1.
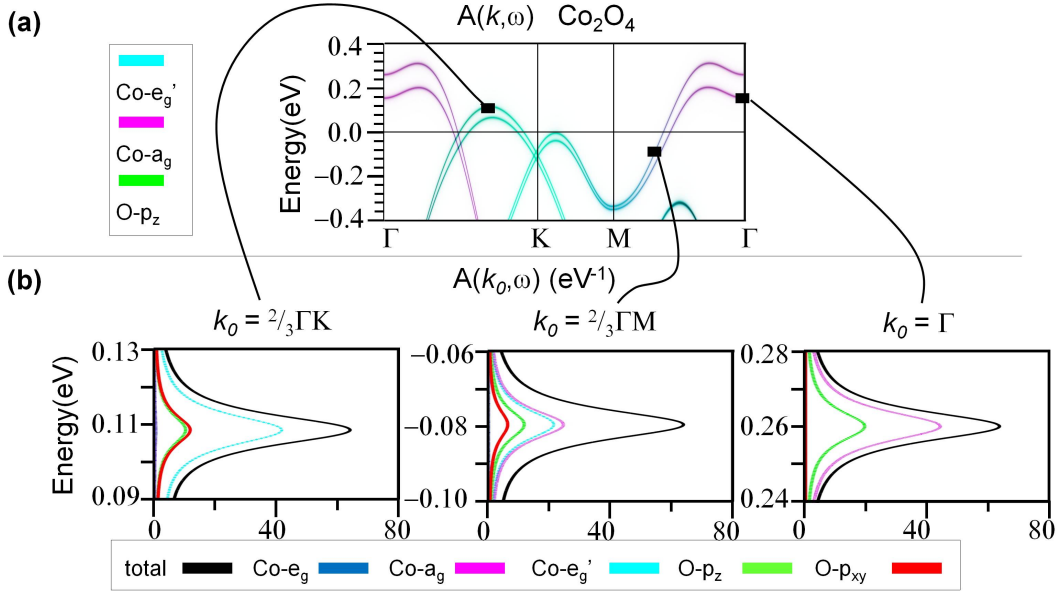
Figure 3.4: Comparison orbital resolution by color vs. exact decomposition.

η(meV)	n_ω	n_k	c_{e_g}	c_{a_g}	$c_{e'_g}$	c_{p_z}	$c_{p_{xy}}$
5	1600	1600	(255,255,255)	(0,255,0)	(255,0,0)	(255,0,255)	(255,255,255)

Table 3.1: Plotting parameters corresponding to Fig.3.4(a)

3.2.3 Realistic Example Unfolding 1: NaxCoO2

As an example, let's consider the effect of periodic Na impurities in Na-doped cobaltates, Na_xCoO_2 at $x = 1/3$. In typical first-principles studies[56, 57], the impurity is incorporated via a supercell as demonstrated in figure 3.4(b) in comparison with the undoped normal cell shown in 3.4(a). Figures 3.4(d) and (c) show the corresponding folded band structures. Since in this example the supercell is three times larger than the normal cell, the corresponding supercell Brillouin zone is three times smaller and contains three times more bands. Even for such a small supercell, the change of the size/orientation of the supercell Brillouin zone and more importantly the large number of folded bands, make it practically impossible to cleanly compare with the band structure in the normal cell Brillouin zone of the undoped parent compound. In fact, to many untrained eyes, these two band structures may appear entirely unrelated.

By contrast, the unfolded band structure shown in Fig. 3.5(e), demonstrates a strong resemblance to the band structure of the undoped compound. This allows a clear visualization of the effects of the (periodic) Na impurities on the original Co and O bands. Specifically, besides the introduction of additional Na-s bands, one observes shifts in band energies, gap openings and the nearby "shadow bands", all of which reflects the influence of the Na impurity on these bands. What is really nice here is the cleanness of the unfolded band structure in general, owing to the weak intensity of the shadow bands. As expected, the influence of the Na impurity is only minor on most Co-d and O-p bands, while the Na-s bands themselves show sizable effects of broken translational symmetry. The size of the gap opening and the intensity of the shadow bands actually reflect directly the strength of each band's coupling to the broken translational symmetry of the normal cell (in this specific case, introduced by the periodic presence of Na atoms).

3.2.4 Realistic Example Unfolding 2: Cu:ZnO (Rocksalt)

Now lets contrast the weak symmetry breaking due to Na interstitials with the strong symmetry breaking due Cu for Zn substitution in rock salt ZnO.
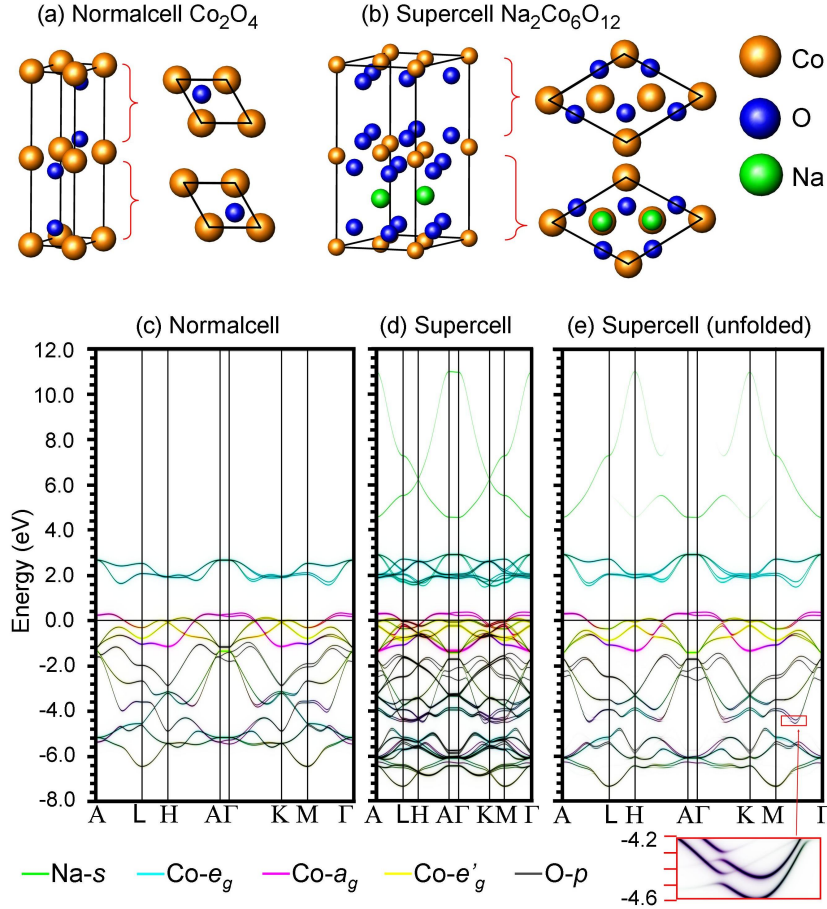
Figure 3.5: Realistic example of folding and unfolding for $Na_2Co_6O_{12}$. Lattice structures of (a) Co_2O_4 (normal cell) and (b) $Na_2Co_6O_{12}$ (supercell), the corresponding band structure of (c) the normal cell and (d) supercell calculation, and (e) the unfolded band structure of the supercell. Insect illustrates the effects of weak translational symmetry breaking via spectral functions over the region [-4.6eV,-4.2eV] and $[\frac{2}{5}\Gamma M, \frac{1}{5}\Gamma M]$.

We perform the simulations with a different functional LSDA+U (U=8eV, J=0.9eV), The lattice parameter a=4.28 Åwas chosen to match the lattice structure of rock salt ZnO at ambient pressure as measured by the diffraction experiments [58, 59]. The low energy Hilbert space is taken within [-8,40] eV consisting of projected Wannier orbitals Zn-d/Cu-d, O-p, Zn-s/Cu-s and Zn-p/Cu-p characters (12/normal cell).

In figure 3.6 we show four band structures, corresponding to ZnO with an increasing amount of Zn for Cu substitutions, starting from pure ZnO (x=0), increasing to pure CuO (x=1). The great advantage of using the unfolded band structure is that also the intermediate cases (x=1/8) and (x=1/4), whose supercell are very different from the 2 limiting cases, can now all be compared on the same normal cell crystal momentum basis. For example when going from x=0 to x=1/8, one sees that the zn-d band (around -5eV) is still very much present yet one can see also see a very weak Cu-O hybrid band appearing around the Fermi surface. Then, as one increases the doping from (x=1/8) to (x=1/4) the Cu-O hybrid band increases its intensity and the Zn-d band starts to weaken. Finally at x=1 the Zn-d band completely dissappears.
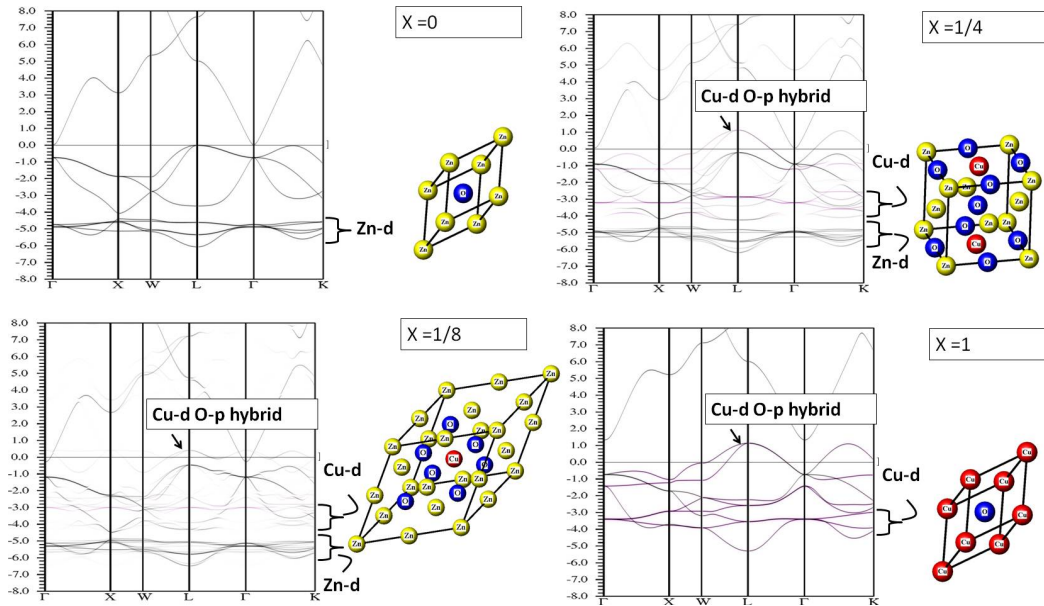
Figure 3.6: unfolded band structures of rocksalt Cu:ZnO.

3.3 The Effective Hamiltonian

The super cell approximation as discussed in the beginning of this chapter has the clear advantage that it is a conceptually clean approximation, in the sense that one can systematically converge the quantity of interest with respect to the supercell size. Moreover this direct approach allows for the investigation of non-local physics, by which we mean phenomena that involve a length scale larger then the normal cell size. However, the price one pays is high. The computational cost of obtaining the eigenvalues and eigenstates will scale with the systems size cubed. Therefore to be able to reach the convergence or to be able to reach the length scale of the non-local physics, one could greatly benefit from some kind of computational approximation method that could increase the efficiency yet not compromise the accuracy. In this section we describe the effective Hamiltonian method that will allow us to construct the low energy effective Hamiltonian of any cellular disordered configuration.

3.3.1 Basic Idea and Explicit Recipe

The Hamiltonian of an arbitrary configuration of N impurities, positioned at $(x_1, ..., x_N)$, can be exactly rewritten as

$$H^{(x_1,...,x_N)} = H^0 + \sum_{i=1}^{N} \Delta^{(x_i)} + \sum_{i>j=1}^{N} \Delta^{(x_i,x_j)} + ... \tag{3.10}$$

where H^0 denotes the Hamiltonian of the system with no impurities, $\Delta^{(x_i)} = H^{(x_i)} - H^0$, denotes the linear influence of the impurity at x_i and $\Delta^{(x_i,x_j)} = H^{(x_i,x_j)} - \Delta^{(x_i)} - \Delta^{(x_j)} - H^0$ denotes the two-body correction of a pair of impurities at (x_i,x_j), etc. The idea of the effective Hamiltonian method is to keep only the lower order impurity influences evaluated in the low energy Hilbert space. In practice we found that it is already highly accurate to keep only the linear influence of the impurities, as demonstrated for example below in section 3.3.4.

At first it might not be clear why this cutoff can lead to accurate results. After all density functional theory is a non-linear theory. Although the external potentials of the impurities will add linearly, the Hartree potential and the exchange correlation potential depend on the density which in turn depends

on the external potential in a non-linear way. But more importantly even if the Hamiltonian was density independent then still its low energy representation in general will depend on the change of external potentials in a non-linear way. Nonetheless there are two basic properties of the influence of disordered impurities that together can make it possible for the linear cut-off to be an accurate approximation. First of all the impurity induced changes in the Hamiltonian will be strongest nearby the position of the impurity. Second of all an impurity influence is never added at the same position twice. So the linear influence $\Delta^{(x_i)} = H^{(x_i)} - H^0$ can in fact incorporate the strong changes of the low energy Hamiltonian nearby the impurity. It is clear that the importance of the Wannier functions will be two-fold. On the one hand the Wannier functions can be used to represent the low energy Hilbert space thereby making the effective Hamiltonian method efficient. On the other hand the Wannier functions are exponentially localized a necessary condition for the linear cut-off to give accurate results.

The construction of the effective Hamiltonian explicitly consists of three steps.

- First, one normal cell DFT calculation is performed for the undoped system and an additional supercell DFT calculation is performed for each type of impurity m.

- Second, the low energy Bloch states of the DFT calculations are Wannier transformed resulting into normal cell and supercell Wannier function based tight binding Hamiltonians: $\langle r'-r'', n|H^0|0n''\rangle$ and $\langle r'n'|H^{(rm)}|r''n''\rangle$. Here, just like in the derivation of the structure factor formula (3.6) the consistency between the normal and supercell Wannier functions is important. We will discuss this issue in section 3.3.2.

- Third, linear super position is used to construct the effective Hamiltonian of any arbitrary configuration. The impurity influence (located in the zeroth normal cell) is extracted by taking the difference of the two tight binding Hamiltonians:

$$
\langle r'n'|\Delta^{(0,m)}|r''n''\rangle \tag{3.11}
$$
$$
= \left(\langle r'-r, n'|H^{(rm)}|r''-r, n''\rangle - \langle r'n'|H^0|r''n''\rangle \right) p^{(r,m)}(r'-r, n, r''-r, n')
$$

42

Where $0 \leq p^{(r,m)}(r', n, r'', n') \leq 1$ is the partitioning function that is necessary to partition the influence of the impurity from its super images. We will define the partitioning function in section 3.3.3. The effective low-energy Hamiltonian corresponding to a disorder configuration with N impurities is then constructed by adding to the undoped Hamiltonian the impurity influences N times at the corresponding positions:

$$\langle r'n'|H_{\text{eff}}^{\{(r_1,m_1),\ldots,(r_N,m_N)\}}|r''n''\rangle \tag{3.12}$$

$$= \langle r' - r'', n'|H^0|0n''\rangle + \sum_{i=1}^{N}\langle r' - r_i, n'|\Delta^{(0,m_i)}|r'' - r_i, n''\rangle$$

where r and n denote the lattice vector and the orbital index of the Wannier functions, and r_i and m_i denote the lattice vector and the type of impurity i, located at $x_i = r_i + x_{m_i}$.

The notation here also implies possible addition of impurity orbitals and removal of orbitals due to vacancies. A similar recipe could be designed if higher order contributions in (3.10) are desired.

3.3.2 Consistency Between Normal Cell and Supercell Wannier Functions

Both for the unfolding method from the previous section (3.2) and for the effective Hamiltonian method discussed in this section it is important to have the Wannier functions as robust as possible against the influence of the impurity. Mathematically this means that the supercell Wannier functions are orthonormal to their corresponding normal cell Wannier functions:

$$\langle rn|RN\rangle = \delta_{r,R+r'(N)}\delta_{nn'(N)} \tag{3.13}$$

where $r'(N)$ is the normal cell lattice index of supercell orbital N within the zeroth supercell. The relationship between the normal cell and supercell coordinates is given by what we in this thesis refer to as "the map" (see appendix B). For the unfolding method the normal cell Wannier states are implicit. The supercell band structure can be unfolded to the normal cell band structure without constructing the normal cell Wannier functions. What equation (3.13)

really means for the unfolding method is that the supercell Wannier states are as consistent as possible amongst themselves. For the effective Hamiltonian method the normal cell Wannier functions are explicitly constructed. The importance of (3.13) is obvious because only when the normal cell and supercell Hamiltonians are represented on the same Wannier basis does their addition and subtraction become meaningful.
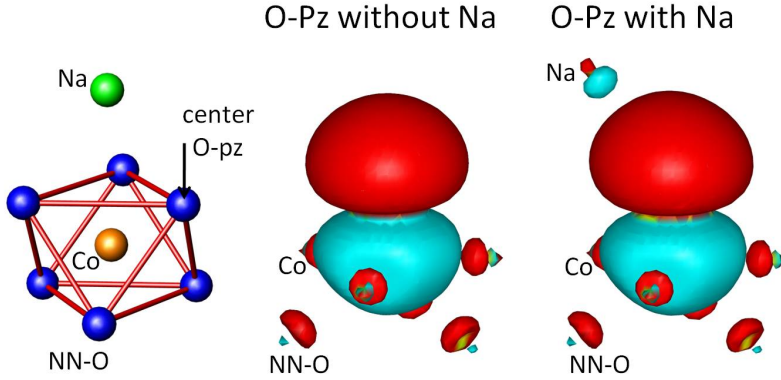
Figure 3.7: Consistency between normal cell and supercell O-p_z Wannier function. On the left the atomic environment of the Wannier functions is displayed. The black arrow indicates the center of the Wannier function. On the right the isosurfaces $|\langle x|rn\rangle|^2 = 10^{-4}\text{bohr}^{-3}$ of the normal cell and supercell O-p_z Wannier function are displayed.

To accomplish the consistency between the normal cell and supercell Wannier functions (3.13) as much as possible two requirements need to be fulfilled in their construction. The first requirement is to make sure that within the energy window of interest, the Hilbert space of the supercell and the normal cell are the same as much as possible. Under the influence of an impurity the atomic character of the bands will mix. Typically this mixing happens mostly within a specific band complex. For example for Na_xCoO_2 the mixing mostly occurs within the cobalt and oxygen band complex. Therefore it is desirable that the entire band complex is included in the analysis, such that certain atomic characters will not leak out of the Hilbert space under the influence of the impurity.

The importance of a big window can also be understood from a different point of view. If the Wannier functions are constructed out of a small number of bands, they necessarily have to be delocalized, because the corresponding

atomic character is spread over different bands. For example the Ta-d_{z^2} Wannier functions in section 2.3.3 were constructed out of the Ta-d_{z^2} bands only and consequently delocalized up to the second nearest neighbors (see figure 2.2). Such delocalized Wannier functions will probably not be good for the linear cut-off in (3.10). If the Wannier functions are bigger then the minimal distance between impurities, probably the two-body impurity influences can no longer be neglected.

So at this point we conclude that the larger the number of Wannier functions on which the Hamiltonian is represented, the more accurate the effective Hamiltonian will be. Of course the flip side of the coin here is that the larger number of Wannier functions also makes the effective Hamilotians computationally more expensive to diagonalize. In practice one needs to find a balance.

The second requirement for the consistency between the normal cell and supercell Wannier functions is to have the gauge of the Wannier functions as consistent as possible. This is naturally accomplished with the projected Wannier function method [37, 47] discussed in section 2.3.1, because one can simply project on the same orbital. Therefore for the methodologies discussed in this chapter, the unfolding and the effective Hamiltonian method, the maximally localized Wannier function method [46] might not be suitable, because it could define the gauge differently in the supercell in favor of better localization near the impurity.

In figure 3.7 we show an example of the consistency between the normal cell and supercell Wannier functions for Na_xCoO_2. Specifically we are showing the oxygen p_z Wannier function which will be most sensitive to the presence of the Na impurity. The difference between the normal cell and supercell Wannier functions (e.g. the absence or presence of the Na tail) only becomes visible for the very low value of the absolute square of the Wannier functions $|\langle x|rn\rangle|^2 = 10^{-4}\text{bohr}^{-3}$ which already indicates that even the O-p_z Wannier function is very robust against the Na impurity. A more quantitative comparison between the normal cell and supercell Wannier functions will be given in the next chapter in figure 4.3 which presents the overlap integrals of the Wannierfunctions evaluated on a grid.

3.3.3 Partitioning a Tight Binding Hamiltonian

When one tries to capture a local effect within a supercell calculation (e.g. frozen phonon calculations or defect formation energy calculations), it is inevitable that one needs to partition the influence of this local effect from its super images. In general there is no unique way for doing this partitioning and therefore one has to make a choice. Before going into the details of the particular partitioning method chosen in this work, let us first briefly discuss a very common application of supercell calculations, namely the calculation of the force constant matrix from which the phonon spectrum can be obtained. In such a calculation, one displaces one of the atoms in the supercell and calculates the forces induced on all the other atoms. In order to partition the forces induced by the displaced atom, from the forces induced by the super images of this displaced atom, one typically uses a hard cutoff. If the atom on which the force is induced is closer to the displaced atom then to its super image, this force will be fully attributed to the displaced atom and vice versa (see figure 3.8). This intuitive strategy however can not be used for the partitioning of a tight binding Hamiltonian. The fundamental difference between a force and a hopping matrix element is that the force is associated with one point in space, namely the position of the atom on which the force is induced. A hopping element, on the other hand, is associated with two points in space, the position of the orbital from which the electron hops and the position of the orbital to which the electron hops. Before going into the details of the particular partitioning method chosen in this work, let us first remark that the effective Hamiltonian method could probably also be followed with another choice of partitioning scheme. In fact, one could perhaps entirely avoid the partitioning by using a cluster DFT code (e.g. GAUSSIAN [60] or FHI-AIMS [61]).

We want to calculate the influence of an impurity on the low energy effective tight binding Hamiltonian, by subtracting the tight binding Hamiltonian with no impurities, $\langle r'n'|H^0|r''n''\rangle$, from the tight binding Hamiltonian with one impurity per supercell, $\langle r'n'|H^{(r,m)+\text{superimages}}|r''n''\rangle$. The objective now is to define a partitioning function $p^{(r,m)}(r'n', r''n'')$, that will enable us to partition the influence of a single impurity on the low energy effective tight binding Hamiltonian, from the influences of its superimages (see equation (3.11)). Since there is no intuitive choice for this partitioning function at hand, we shall
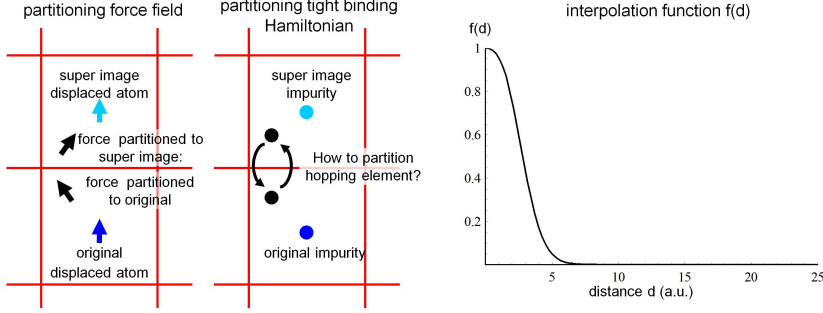
Figure 3.8: Partitioning of the tight binding Hamiltonian (Left) The typical partitioning strategy used in the calculation of the force constant matrix, the hard cutoff, can not be used to partition hopping elements of a tight binding Hamiltonian. (Right) Interpolation function $f_{r,c,w}(d)$ as a function of distance d with the parameters r_{cut}=25a.u., c=2.5a.u., w=1.25a.u.

start from an abstract form and add more and more desirable properties to it until we arrive at its explicit form. First of all we ensure that the partitioning function is normalized by defining it as

$$p^{(r,m)}(r'n', r''n'') = \frac{P^{(r,m)}(r'n', r''n'')}{\sum_{R \in \text{superlattice}} P^{(R+r,m)}(r'n', r''n'')} \qquad (3.14)$$

The next step is to define a distance between the hopping element $\langle r'n'|H|r''n''\rangle$ and the impurity (r, m). We choose

$$d^{(r,m)}(r'n', r''n'') = |\underbrace{r' + x_{n'}}_{\text{to}-\text{WF}} - \underbrace{r + x_m}_{\text{impurity}}| + |\underbrace{r'' + x_{n''}}_{\text{from}-\text{WF}} - \underbrace{r + x_m}_{\text{impurity}}| \qquad (3.15)$$

Here x_m,$x_{n'}$ and $x_{n''}$ are the positions within the normal cell of the impurity of type m and the Wannier state of type n' and n'' respectively. To put it in words the distance between an impurity and a hopping element will be defined as the sum of the distance of the impurity to the center of the "from-Wannier function" $\langle x|r''n''\rangle$ and the distance of the impurity to the center of the "to-Wannier function" $\langle x|r'n'\rangle$. Examples on a square lattice are given in figure 3.9.

Finally we need to define an interpolation function $f = f(d)$, a function of the distance, that smoothly interpolates between 1 at distance 0 and 0 at a
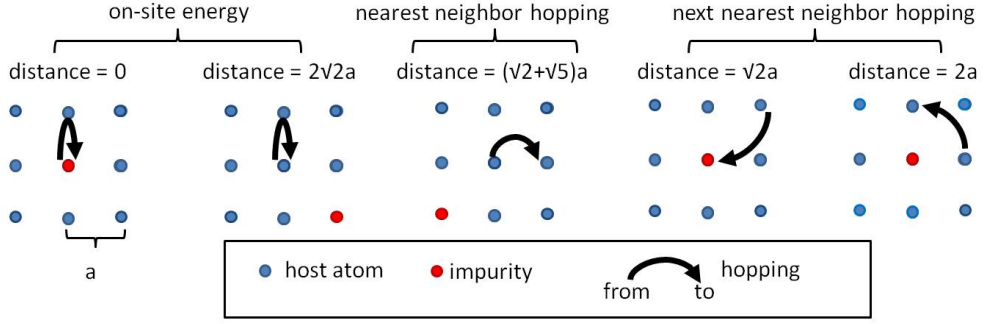
Figure 3.9: Examples of impurity-hopping element distances.

distance far away. The unnormalized partitioning function is then given by

$$P^{(r,m)}(r'n', r''n'') = f(d^{(r,m)}(r'n', r''n''))$$ (3.16)

The normalized partitioning function is then given by equations (3.14-3.16) and a yet to be defined interpolation function f.

First of all we want the interpolation function to satisfy the correct boundary conditions at distance 0 and some normalized cut-off distance. Specifically we require: $f(0) = 1$ and $f'(0) = f(1) = f'(1) = 0$. The following polynomial, $q(x)$, satisfies these boundary conditions:

$$q(x) = 1 - 3x^2 + 2x^3$$ (3.17)

Second of all we want to have some control over where the interpolating function drops to zero and how fast. For this purpose we borrow the Fermi-Dirac distribution function from statistical mechanics

$$g_{c,w}(x) = \frac{1}{\exp(\frac{x-c}{w}) + 1}$$ (3.18)

were the chemical potential corresponds to the center c of the drop and the temperature corresponds to the width w of the drop. Since the distance needs to be 0 when $x = 0$ and 1 when $x = r_{cut}$ we modify the Fermi function:

$$h_{c,w}(x) = \frac{g_{c,w}(0) - g_{c,w}(x)}{g_{c,w}(0) - g_{c,w}(r_{cut})}$$ (3.19)

The final interpolation function is obtained from combining (3.17)-(3.19).

$$f_{r,c,w}(x) = q(h_{c,w}(x))\theta(x - r_{cut}) \tag{3.20}$$

where r_{cut} is the cut-off distance beyond which the influence of an impurity is taken to be zero. In figure 3.8 the interpolation function is plotted for the parameters r_{cut}=25a.u., c=2.5a.u., w=1.25a.u., which are typical parameters used for the construction of the effective Hamiltonians in this work.

In appendix E, we work out the partitioning of a tight binding Hamiltonian difference, for the case of a simple toy model. As will become clear in that explicit example, the arbitrary choice of the interpolation function (3.17)-(3.20) is usually irrelevant for the partitioning.

3.3.4   Testing the Quality of the Effective Hamiltonian
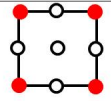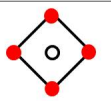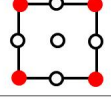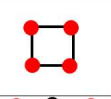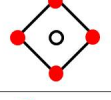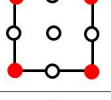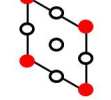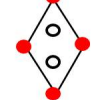
$\mathbf{M_{in}}$	$\mathbf{M_{test}}$	x_{in}	x_{test}	$\mathbf{M_{in}^{test}}$	linearity-test?	partition-test?
$\begin{pmatrix} 2 & 0 \\ 0 & 2 \end{pmatrix}$	$\begin{pmatrix} 1 & 1 \\ -1 & 1 \end{pmatrix}$	1/4	1/2	$\begin{pmatrix} 1 & 1 \\ -1 & 1 \end{pmatrix}$	yes	no
$\begin{pmatrix} 2 & 0 \\ 0 & 2 \end{pmatrix}$	$\begin{pmatrix} 1 & 0 \\ 0 & 1 \end{pmatrix}$	1/4	1	$\begin{pmatrix} 2 & 0 \\ 0 & 2 \end{pmatrix}$	ultimate	no
$\begin{pmatrix} 1 & 1 \\ -1 & 1 \end{pmatrix}$	$\begin{pmatrix} 2 & 0 \\ 0 & 2 \end{pmatrix}$	1/2	1/4	$\begin{pmatrix} \frac{1}{2} & \frac{1}{2} \\ -\frac{1}{2} & \frac{1}{2} \end{pmatrix}$	no	yes
$\begin{pmatrix} 2 & 0 \\ 0 & 2 \end{pmatrix}$	$\begin{pmatrix} 1 & 1 \\ -1 & 2 \end{pmatrix}$	1/4	1/3	$\begin{pmatrix} \frac{4}{3} & -\frac{2}{3} \\ \frac{2}{3} & \frac{2}{3} \end{pmatrix}$	yes	yes

Figure 3.10:   Testing quality of effective Hamiltonian: toy examples.

To test the quality of the effective Hamiltonian we will design test systems that are small enough to be be calculated within the full density functional theory. Then by comparing the quantity of interest, the spectral function $A_n(k, \omega)$, computed both from DFT and from the effective Hamiltonian, the quality of the effective Hamiltonian can be tested. Two aspects need to be tested, namely the linearity assumption and the quality of the partitioning. In figure 3.10 we give some two dimensional toy examples of how one can

design test systems that can test those two aspects. Designing a test system for testing the linearity is simple, namely the larger the extrapolation of the concentration of impurities the better the test case. For example in the first row of figure 3.10 we see a 2×2 input supercell to extract the impurity influence and a $\sqrt{2} \times \sqrt{2}$ supercell to test the quality of the effective Hamiltonian. The reason why this test case tests the linearity is because the concentration of impurities is extrapolated from $1/4$ to $1/2$. In that sense the test system in the second row of figure 3.10 is the ultimate test case of linearity, because the concentration of impurities is extracted from $1/4$ all the way to 1 the maximum amount of impurities that there can be.

To test the quality of the partitioning is a little bit more of a complicated issue. A test case that extrapolates the concentration of impurities to a smaller value is always a good test case for the partitioning. An example of such a test case is given in the third row of figure 3.10, in which the concentration of impurities is extrapolated from $1/2$ to $1/4$. However the other way around is not true. In other words a good test case for the partitioning does not necessarily extrapolate to a lower concentration of impurities. For example the test case in the fourth row extrapolates from $1/4$ to $1/3$ and yet is a good test case for the partitioning. Why is that the case? In appendix F we shall proof the following statement, namely that the effective Hamiltonian, depends on the partitioning function (3.14)-(3.16) if and only if the input superlatttice is a subset of the test superlattice.[2] The condition of the input superlatttice being a subset of the test superlattice is conveniently rephrased as the transformation matrix from the test-supercell to the input-supercell being an integer matrix:

$$M_{in}^{test} = M_{test}^{-1} \cdot M_{in} = \text{integer matrix}$$

$$\Leftrightarrow \quad \langle rn|H_{test}|r'n'\rangle \text{ independent of partitioning function} \qquad (3.21)$$

where M_{test} is the matrix that transforms from the test-supercell basis to the normal cell basis and M_{in} is the matrix that transforms from the input-

---

[2]This statement is in direct analogy with the more commonly known fact that in a frozen phonon calculation, the phonon frequency and wave vector become exact when its crystal momentum is equal to a reciprocal vector of the supercell within which the force constant matrix was calculated.

supercell basis to the normal cell basis. For example M_{in}^{test} in the test systems in the first two rows of figure 3.10 are integer matrices and therefore these test systems do no test partitioning. This means no matter what kind of crazy partitioning scheme is used, the effective Hamiltonian will always be the same. The transformation matrices M_{in}^{test} of the test systems in the third and fourth row of figure 3.10 are non-integer and therefore they do test the quality of the partitioning.
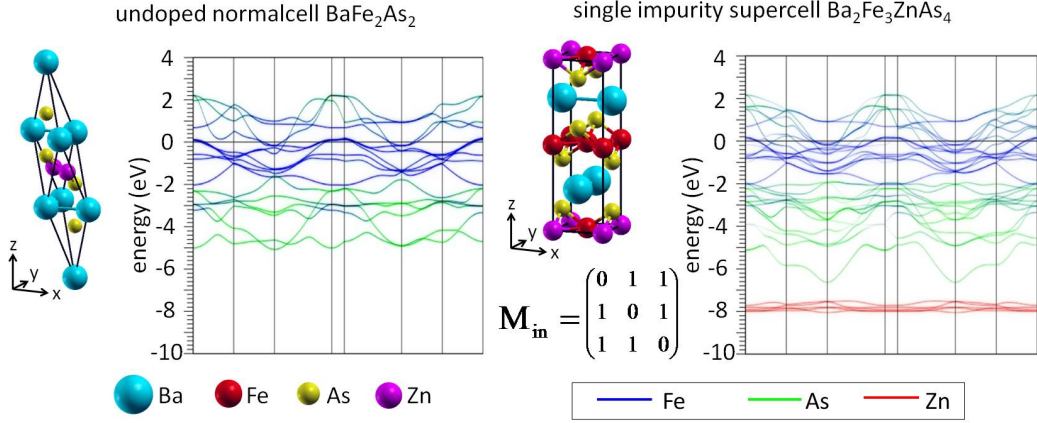
Figure 3.11: Input systems for studying Zn:BaFe$_2$As$_2$.

Now let us consider test cases for a realistic system, namely Zn for Fe substitutions in Ba(Fe$_{1-x}$Zn$_x$)$_2$As$_2$. The undoped BaFe$_2$As$_2$ has a body-centered tetragonal lattice structure of which the primitive cell is depicted on the left of figure 3.11. The influence of a Fe for Zn substitution is extracted from of Ba$_2$Fe$_3$ZnAs$_4$ of which the "input" supercell is depicted on the right of figure 3.11. The space group I4/mmm and the values of the lattice parameters a=b=3.9625 Åand c=13.0168 Åand the As height z=0.3545, were taken from [62]. The low energy Hilbert space is taken within [-10,4] eV consisting of projected Wannier orbitals of Zn-d/Fe-d and As-p characters (16/normal cell).

The test system BaZn$_2$As$_2$ is used to test the linearity the results of which are displayed in figure 3.12. From comparing the band structures computed from the effective Hamiltonian and from the full DFT, we can see that linearity approximation is amazingly accurate considering that the dramatic extrapolation all the way to 100 percent doping and considering that the impurity
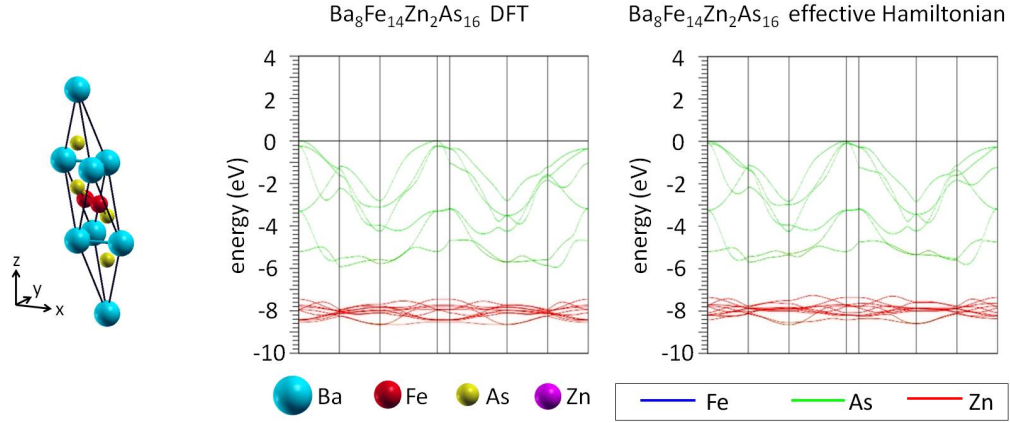
Figure 3.12: Testing the linearity assumption for Zn:BaFe$_2$As$_2$.

itself in this case, the Fe for Zn substitution is a very dramatic perturbation containing a downwards onsite energy shift of about 8eV. The test system of Ba$_8$Fe$_{14}$Zn$_2$As$_{16}$ is used to test the quality of the partitioning test the results of which are displayed in figure 3.13. Notice from the transformation matrix M_{in}^{test} is only non-integer in the plane, meaning the this particular test system actually does not test the quality of the out of plane partitioning.
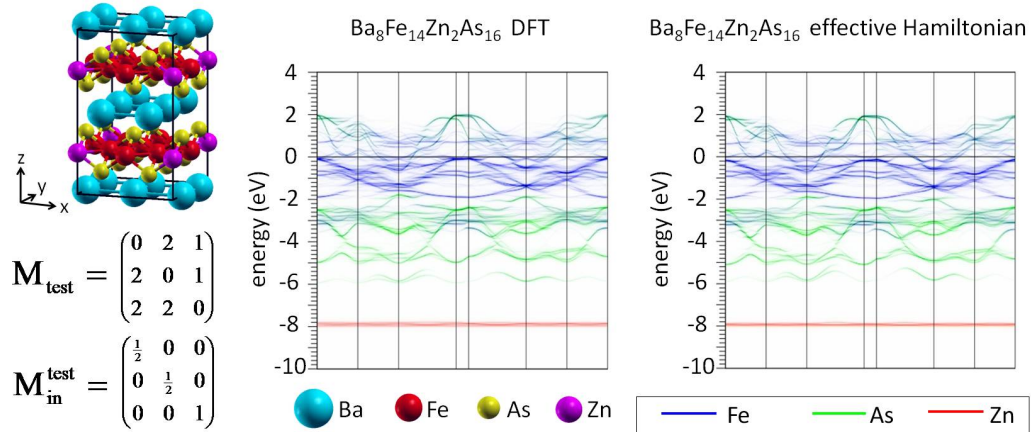
Figure 3.13: Testing the quality of the partitioning for Zn:BaFe$_2$As$_2$.

Chapter 4

Application 1: Can Disorder Alone Destroy the eg' Hole Pockets of NaxCoO2?

The work presented in this chapter has been published in reference [51].

4.1 Introduction

Like most transition metal oxides, sodium cobaltates obtain their important properties via the introduction of dopants (Na) between the layered structures of oxygen and transition metal atoms. Around $x = 0.3$, Na_xCoO_2 develops unconventional superconductivity under hydration [63], with evidence of a nodal order parameter [64]. From $x < 0.5$ to $x > 0.5$ it changes from a paramagnetic metal to a Curie-Weiss metal, while it is a charge ordered insulator at $x = 0.5$ [65]. At high doping, the combination of high thermopower and high conductivity is observed [66], together with A-type anti-ferromagnetism [67]. In addition, various Na orderings have been observed throughout the entire phase diagram [68]. This rich variety of behaviors has thus attracted intensive research activity.

Nevertheless, even the most basic starting point for an understanding is still under serious debate, namely the low-energy electronic structure near the chemical potential that controls most of the above mentioned remarkable properties. Early density functional (DFT) calculations [69] within the lo-

cal density approximation (LDA) predicted the existence of a central a_g hole pocket, surrounded by 6 e'_g hole pockets. Angle resolved photoemission spectroscopy (ARPES) experiments [70, 71] measured the central a_g pocket, but found the e'_g bands to be below the Fermi surface. Shubnikov-de Haas measurements [72] observed two pockets, but the assignment to e'_g was concluded incompatible with the specific heat data [73]. On the other hand, the presence of the second type of pocket was reconfirmed by Compton scattering [74] and assigned to e'_g.

Despite the controversial status on the experimental front, various theoretical efforts have been made to investigate the alleged absence of the e'_g pocket. Surface effects were suggested to suppress the e'_g pocket [57] under hydroxyl contamination. The other usual suspect of many-body correlation was investigated within dynamical mean-field theory (DMFT) by several groups. However, the results were inconclusive as the e'_g pockets were found to either grow or shrink depending sensitively on the crystal field splitting [75, 76]. Some researchers [77] argued that the e'_g pockets should not exist according to the specific heat data, while others [78] concluded from an extensive study of the crystal field that the e'_g pockets *cannot* be removed via local correlation.

Recently, an intriguing alternative resolution was proposed [56, 79]. It was argued that the random positioning of the Na intercalants alone can introduce strong disorder effects that mask the e'_g pockets from the ARPES experiments. This physically plausible picture, if proven, would not only enable a new resolution to reconcile the various theoretical and experimental observations, but would also introduce important novel physics missing in current considerations.

In this chapter, we examine the proposal of disorder-induced destruction of the e'_g pockets in Na_xCoO_2, using $x = 0.3$ as a representative case, by applying the first-principles Wannier function-based methods for the evaluation of electronic structure of disordered materials that was presented in chapter 3. Remarkable spectral broadenings ($\sim$1eV) of the oxygen bands are found that provide a natural explanation for the missing oxygen bands in ARPES studies. However, in contradiction with the current claim [56, 79], we only find a negligible influence of disorder on the e'_g pockets, incapable of masking them from the ARPES experiments.

4.2 Computational Details
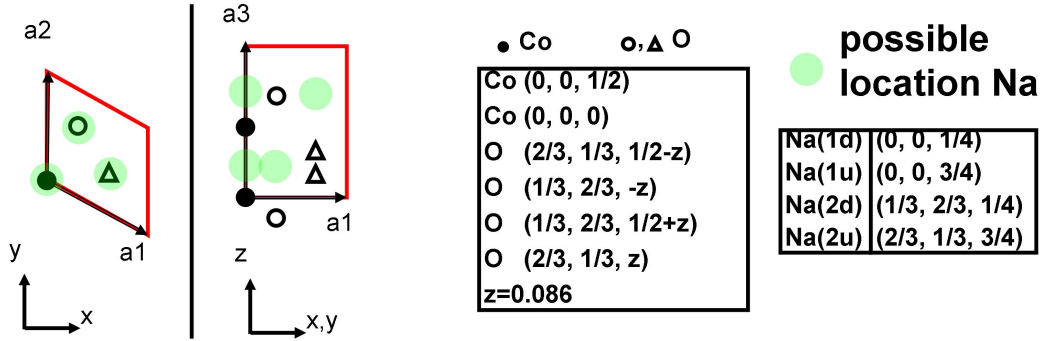
Figure 4.1: Normal cell Co_2O_4 with possible Na impurity locations.

The lattice structure of the undoped normal cell Co_2O_4, is depicted in the cartoon in figure 4.1. Its space group $P6_3/mmc$ and its lattice parameters a=5.31 bohr, c=21.2 bohr and z=0.086 were chosen to match the lattice structure of $Na_{0.3}CoO_2$ as measured by the diffraction experiments [80–85]. The lattice vectors expressed in Cartesian coordinates are given by: $a_1 = -\frac{1}{2}a\hat{x} + \frac{\sqrt{3}}{2}a\hat{y}$; $a_2 = a\hat{y}$; $a_3 = c\hat{z}$. Following [56] we model the Na dopants to be located at 4 positions within the normal cell, for which we introduce the corresponding labels Na(1d), Na(1u), Na(2d) and Na(2u). Here the labels d and u indicate whether the Na is located in the down-layer or the up-layer. The labels 1 and 2 indicate whether the Na is located at Wyckoff site 2a (above Co) or 2b (above a hole in the Co-sheet). We applied the WIEN2K[30] implementation of the full potential linearized augmented plane wave method in the local density approximation, as employed by [56] to remove any ambiguity of basis and functional dependence in the comparison. The basis size was determined by RKmax=7. The k-point meshes were chosen to be 12×12×3 for the normal cell Co_2O_4, 6×6×3 for the 2×2×1 super cells $Na(1)Co_8O_{16}$ and $Na(2)Co_8O_{16}$ and and 8×8×3 for the $\sqrt{3}\times\sqrt{3}\times1$ super cell $Na(2d)Na(1u)_2Co_6O_{12}$.

The Wannier functions are constructed according to the LAPW based projection recipe described in section 2.3.1. The low-energy Hilbert space is taken within [-8,3] eV consisting of symmetry-respecting complex Wannier orbitals of Co-d and O-p characters (22/normal cell) as illustrated in figure 4.2. The defining coefficients of the projected orbitals (see (2.34)) are chosen such that

55
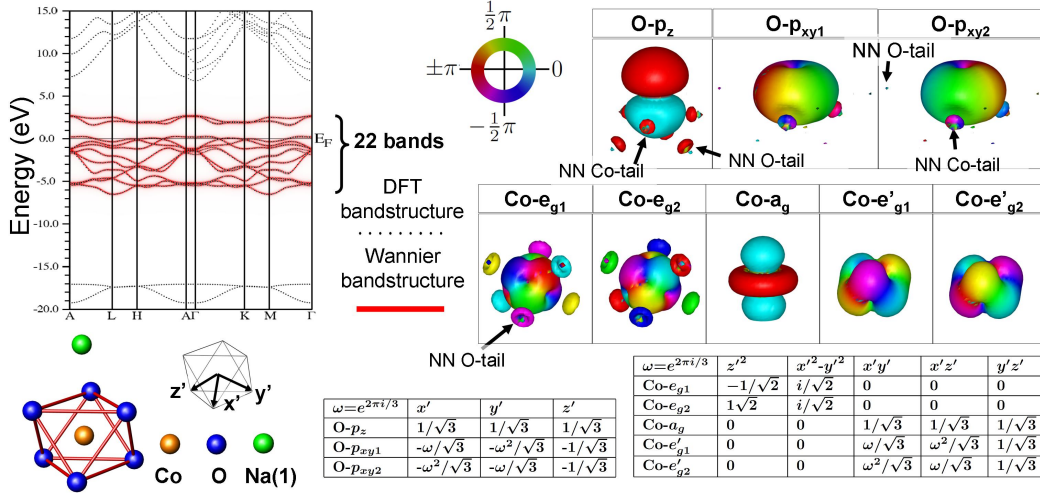
Figure 4.2: The Co-d and O-p Wannier functions. (Left up) Low energy Hilbert space of the normal cell Co_2O_4 is shown consisting of 22 bands in the energy window [-8,3]eV. (Right up) Isosurface plot $|\langle x|rn\rangle| = 0.03(\text{bohr})^{-3/2}$ of symmetry respecting Co-d and O-p Wannier functions, colored according to the phase of the complex functions. (Left down) Local crystal field environment and primed coordinate system. (Right down) Definition of the angular part of the projected orbitals $P_{ln}(\Omega)$ in terms of the primed coordinates.

The O-p projection table:

$\omega=e^{2\pi i/3}$	x'	y'	z'
O-p_z	$1/\sqrt{3}$	$1/\sqrt{3}$	$1/\sqrt{3}$
O-p_{xy1}	$-\omega/\sqrt{3}$	$-\omega^2/\sqrt{3}$	$-1/\sqrt{3}$
O-p_{xy2}	$-\omega^2/\sqrt{3}$	$-\omega/\sqrt{3}$	$-1/\sqrt{3}$

The Co-d projection table:

$\omega=e^{2\pi i/3}$	z'^2	$x'^2-y'^2$	$x'y'$	$x'z'$	$y'z'$
Co-e_{g1}	$-1/\sqrt{2}$	$i/\sqrt{2}$	0	0	0
Co-e_{g2}	$1\sqrt{2}$	$i/\sqrt{2}$	0	0	0
Co-a_g	0	0	$1/\sqrt{3}$	$1/\sqrt{3}$	$1/\sqrt{3}$
Co-e'_{g1}	0	0	$\omega/\sqrt{3}$	$\omega^2/\sqrt{3}$	$1/\sqrt{3}$
Co-e'_{g2}	0	0	$\omega^2/\sqrt{3}$	$\omega/\sqrt{3}$	$1/\sqrt{3}$

grid 25-25-25

	e'g1	e'g2	ag	eg1	eg2	pz	pxy1	pxy2
Co-e'g1	0.89	0.00	0.00	0.01	0.05	0.00	0.00	0.00
Co-e'g2	0.00	0.89	0.00	0.05	0.01	0.00	0.00	0.00
Co-ag	0.00	0.00	0.85	0.01	0.01	0.00	0.00	0.00
Co-eg1	0.01	0.05	0.01	0.91	0.05	0.00	0.00	0.00
Co-eg2	0.05	0.01	0.01	0.05	0.91	0.00	0.00	0.00
O-pz	0.00	0.00	0.00	0.00	0.00	0.89	0.00	0.00
O-pxy1	0.00	0.00	0.00	0.00	0.00	0.00	0.88	0.01
O-pxy2	0.00	0.00	0.00	0.00	0.00	0.00	0.01	0.88

grid 45-45-45

	e'g1	e'g2	ag	eg1	eg2	pz	pxy1	pxy2
Co-e'g1	0.93	0.00	0.00	0.00	0.00	0.00	0.00	0.00
Co-e'g2	0.00	0.93	0.00	0.00	0.00	0.00	0.00	0.00
Co-ag	0.00	0.00	0.93	0.00	0.00	0.00	0.00	0.00
Co-eg1	0.00	0.00	0.00	0.93	0.00	0.00	0.00	0.00
Co-eg2	0.00	0.00	0.00	0.00	0.93	0.00	0.00	0.00
O-pz	0.00	0.00	0.00	0.00	0.00	0.93	0.00	0.00
O-pxy1	0.00	0.00	0.00	0.00	0.00	0.00	0.93	0.00
O-pxy2	0.00	0.00	0.00	0.00	0.00	0.00	0.00	0.93

grid 75-75-75

	e'g1	e'g2	ag	eg1	eg2	pz	pxy1	pxy2
Co-e'g1	0.95	0.00	0.00	0.00	0.00	0.00	0.00	0.00
Co-e'g2	0.00	0.95	0.00	0.00	0.00	0.00	0.00	0.00
Co-ag	0.00	0.00	0.95	0.00	0.00	0.00	0.00	0.00
Co-eg1	0.00	0.00	0.00	0.95	0.00	0.00	0.00	0.00
Co-eg2	0.00	0.00	0.00	0.00	0.95	0.00	0.00	0.00
O-pz	0.00	0.00	0.00	0.00	0.00	0.95	0.00	0.00
O-pxy1	0.00	0.00	0.00	0.00	0.00	0.00	0.95	0.00
O-pxy2	0.00	0.00	0.00	0.00	0.00	0.00	0.00	0.95

Figure 4.3: Absolute value of the overlap matrix $|\langle rn|rn'\rangle|$ of the Co-d and O-p Wannier functions. The overlap integrals are evaluated in the box shown in upper left. As a function of the grid size, the overlap matrices tend to converge to $|\langle rn|rn'\rangle| = \delta_{nn'}$.

overlap normal cell with normal cell WF

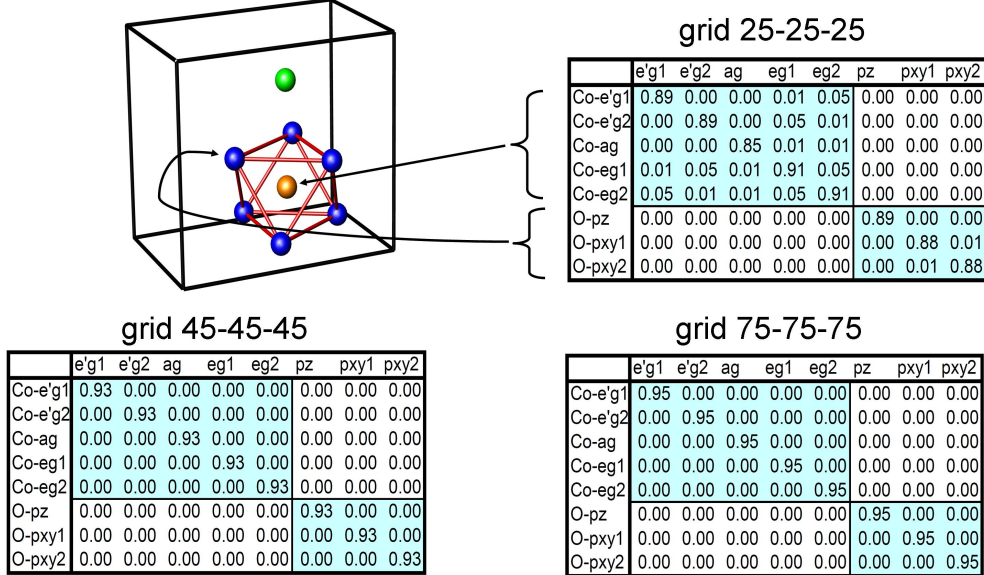|	e'g1	e'g2	ag	eg1	eg2	pz	pxy1	pxy2
Co-e'g1	0.9507	0.0003	0.0002	0.0001	0.0002	0.0003	0.0005	0.0004
Co-e'g2	0.0003	0.9507	0.0002	0.0002	0.0001	0.0003	0.0004	0.0005
Co-ag	0.0002	0.0002	0.9492	0.0004	0.0004	0.0002	0.0000	0.0000
Co-eg1	0.0001	0.0002	0.0004	0.9518	0.0001	0.0000	0.0000	0.0002
Co-eg2	0.0002	0.0001	0.0004	0.0001	0.9518	0.0000	0.0002	0.0000
O-pz	0.0003	0.0003	0.0002	0.0000	0.0000	0.9521	0.0000	0.0000
O-pxy1	0.0005	0.0004	0.0000	0.0000	0.0002	0.0000	0.9502	0.0016
O-pxy2	0.0004	0.0005	0.0000	0.0002	0.0000	0.0000	0.0016	0.9502

overlap normal cell with super cell WF

	e'g1	e'g2	ag	eg1	eg2	pz	pxy1	pxy2
Co-e'g1	0.9506	0.0003	0.0002	0.0000	0.0002	0.0000	0.0007	0.0007
Co-e'g2	0.0003	0.9506	0.0002	0.0002	0.0000	0.0000	0.0007	0.0007
Co-ag	0.0002	0.0002	0.9488	0.0004	0.0004	0.0002	0.0007	0.0007
Co-eg1	0.0000	0.0002	0.0004	0.9518	0.0001	0.0000	0.0000	0.0002
Co-eg2	0.0002	0.0000	0.0004	0.0001	0.9518	0.0000	0.0002	0.0000
O-pz	0.0000	0.0000	0.0002	0.0000	0.0000	0.9497	0.0014	0.0014
O-pxy1	0.0007	0.0007	0.0007	0.0000	0.0002	0.0014	0.9494	0.0011
O-pxy2	0.0007	0.0007	0.0007	0.0002	0.0000	0.0014	0.0011	0.9494

Figure 4.4: Consistency Between Normal and Supercell Co-d and O-p Wannier Functions. Shown are the absolute value of the overlap matrix $|\langle rn|rn'\rangle|$ of the Co-d and O-p Wannier functions from the normal cell, compared with overlap matrix of $|\langle rn|R(r)N(r,n')\rangle|$ of the Co-d and O-p Wannier functions from the normal cell and the super cell. The overlap integrals are evaluated in the box shown to the left of figure 4.3 on a 75-75-75 grid.

they respect the symmetry of the local crystal field environment. From the smallness (or complete absence) of the tails of the Wannier functions in the nearest neighboring atoms, it can be seen that the Wannier functions are highly localized. A more quantitative demonstration of the degree of localization is given by the overlap matrices presented in figure 4.3. The Wannier functions for any of the supercell calculations are constructed consistently by projecting the same orbitals on the supercell Bloch states in the same energy window. The degree of consistency between the normal cell $|rn\rangle$ and the corresponding super cell $|R(r)N(r,n)\rangle$ Wannier states, is quantified by the overlap matrix presented in figure 4.4.

The effects of impurities are extracted from three DFT calculations: the undoped Co_2O_4 in the normal cell and $Na(1)Co_8O_{16}$ and $Na(2)Co_8O_{16}$ in $2\times2\times1$ super cells corresponding to $x = \frac{1}{8}$. The quality of our effective Hamiltonian can be verified by benchmarking the spectral function of a test system, against the standard DFT. As a highly non-trivial test case we take the periodic $Na(2)Na(1)_2Co_6O_{12}$(c.f. figure 4.5(c)), which requires a strongly "incommensurate" extrapolation in the partitioning (from $2 \times 2 \times 1$ to $\sqrt{3}\times\sqrt{3}\times1$ cell) and the linearity (from $x = \frac{1}{8}$ to $x = \frac{1}{2}$) of the influence of impurities. As shown in figure 4.5, the effective Hamiltonian manages to reproduce the spectral function of the full DFT calculation with high accuracy (in particular the details around the gap opening), but with only a negligible fraction of the computational effort. (The full DFT calculation involved $\sim$20 self-consistent cycles on a basis of 2019 linear augmented plane waves, while the effective
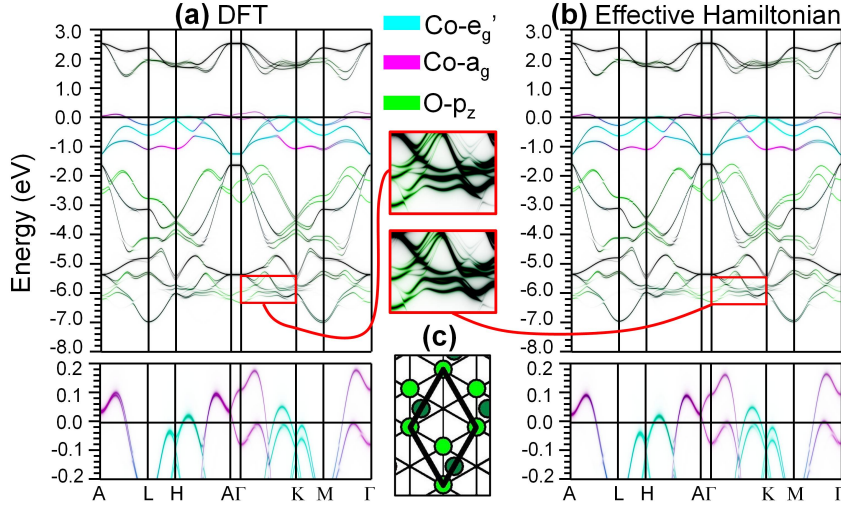
Figure 4.5: Benchmarking the quality of the effective Hamiltonian. Shown are the spectral function of $Na(2)Na(1)_2Co_6O_{12}$ obtained from: (a) the full DFT calculation, on a basis of 2019 LAPW's (b) a single diagonalization of the effective Hamiltonian, on a basis of 66 Wannier functions. (c) Na positions in the super cell, in relation to triangular Co sheet. Light/dark circles denote Na above/below the Co sheet.

Hamiltonian requires only a single diagonalization on a basis of 66 Wannier functions.) Additional benchmarks exploring the potential limitations for large extrapolations are given in appendix G.

In order to estimate the additional influence of the impurities due to lattice relaxation, we perform a relaxation study on the $\sqrt{3} \times \sqrt{3} \times 1$ super cell $Na(1d)_2Na(2u)_2Co_6O_{12}$, by applying the PORT minimization scheme as implemented in WIEN2K[30]. In figure 4.6 we illustrate the spectral functions of three systems: Co_2O_4, $Na(1d)_2Na(2u)_2Co_6O_{12}$ and $Na(1d)_2Na(2u)_2Co_6O_{12}$-relaxed. By comparing the spectral functions of Co_2O_4 and $Na(1d)_2Na(2u)_2Co_6O_{12}$, we can visualize the influence of the Na impurity on the band structure, without relaxation. By comparing the spectral functions of $Na(1d)_2Na(2u)_2Co_6O_{12}$ and $Na(1d)_2Na(2u)_2Co_6O_{12}$-relaxed, we can visualize additional change in the band structure due to relaxation. From figure 4.6 we see that the additional change in the band structure due to relaxation is much smaller in comparison.

Following the considerations laid out in Ref. [56], all the random configurations of Na are assumed comparable in probability, except the high energy case containing two nearest neighboring Na atoms located at Na(1) and Na(2) sites

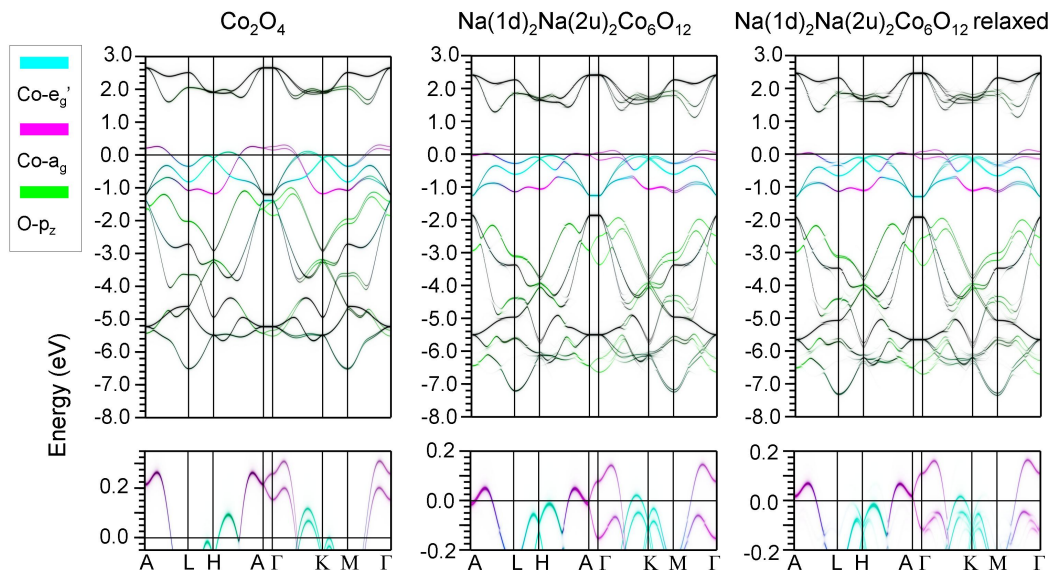Figure 4.6: The additional influence of lattice relaxation. Shown are the spectral functions of Co_2O_4, $Na(1d)_2Na(2u)_2Co_6O_{12}$ and $Na(1d)_2Na(2u)_2Co_6O_{12}$-relaxed.
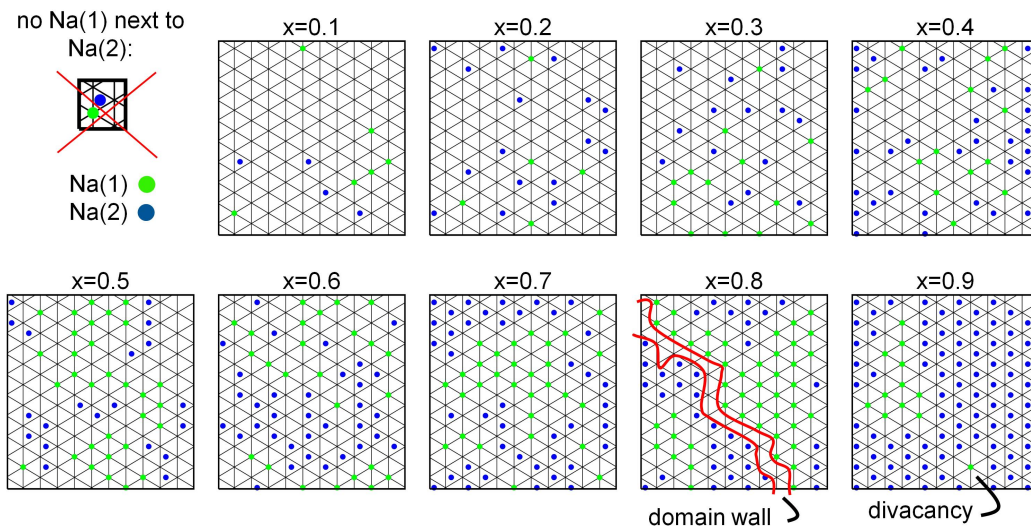

Figure 4.7: Doping dependence of the short range order. The simple rule of excluding configurations in which Na(1) sits next to Na(2), induces a short range order with increasing correlation length as a function of doping.

(see figure 4.7), which is disregarded due to its low probability. Interestingly this simple constraint induces a short range order in the distribution of Na impurities. To illustrate the doping dependence of the short range order of Na impurities as modeled in our work, we present here a series of configurations with increasing doping. Each configuration has the fixed geometry of 10×10 Co atoms. The Na impurities are randomly distributed over Na(1) and Na(2) positions under the constraint that no Na(1) can sit next to a Na(2) (at a distance smaller then 1 lattice constant). As can be seen from figure 4.7 this simple rule induces a short range order with increasing correlation length as a function of doping. This can be easily understood from the fact that the "domain walls" between the Na(1) and Na(2) regions requires more Na vacancies. Therefore, with larger x, the domain must grow in size to reduce such vacancies. Interestingly, at large doping (for example, in the lower right of x=0.9 panel) the recently experimentally proposed "divacancy" [86] start to appear in the configuration as a result of the same consideration.

Physically, since the "domain walls" consists of lower Na concentration, it is reasonable to expect modulation of charge and spin in the nearby Co-ions, consistent with the reported Co^{3+}/Co^{4+} ordering within GGA+U [87], although presumably the long range order of the Na position should not be necessary for the formation of local moment, in our opinion. For example, the above random "divacancy" might already suffice to produce well defined (fluctuating) local moments.

4.3   Results

Having an accurate and efficient method to assemble the effective Hamiltonian of any configuration, we proceed to evaluate the configuration-averaged spectral functions for the case of disordered $Na_{0.3}CoO_2$. Figure 4.8 shows the resulting spectral function converged with respect to the number of configurations (50) and their average size ($\sim$80 normal cells corresponding to $80 \times 22 = 1760$ Wannier functions). Note that it is necessary to consider super cells (e.g.: figure 4.8(a)) of different sizes, orientations, and shapes in order to remove the effects of artificial zone boundaries of the super cell.

A remarkable broadening of oxygen bands can be observed in figure 4.8(d)(g),
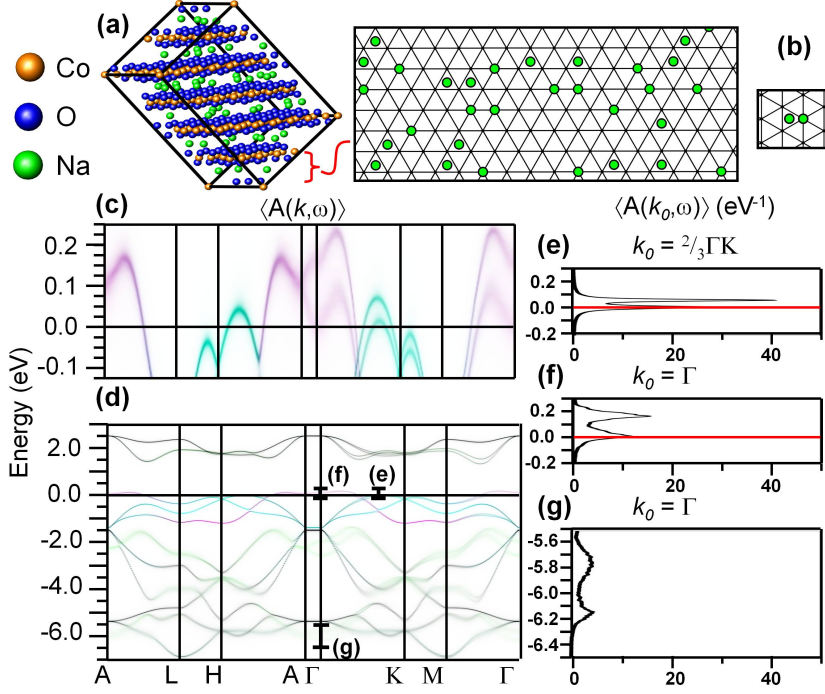
Figure 4.8: Configuration-averaged spectral function of $Na_{0.3}CoO_2$, showing the e'_g states to be the least influenced by disorder. (a) One of the 50 large-sized super cells used for configurational average. (b) A high energy configuration with Na(1) too close to Na(2). $\langle A(k,\omega)\rangle$ (c) around the Fermi-surface (d) in the full low-energy Hilbert space, where the bars correspond to the energy distribution curves (e) at $k_0=2\Gamma K/3$, (f) at $k_0=\Gamma$, (g) at $k_0=\Gamma$. The Wannier orbital character is labeled according to the color scheme of figure 4.5.
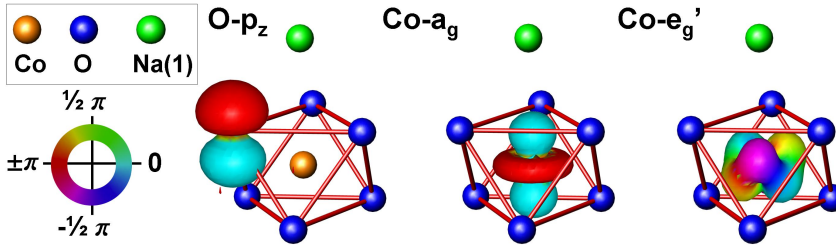
Figure 4.9: Isosurface plot $|\langle x|rn\rangle| = 0.09(bohr)^{-3/2}$ of selected Wannier functions, colored according to the phase of the complex functions.

indicating a short lifetime and mean free path of the quasi-particles due to strong scattering against the disordered Na atoms. This is easily understood considering that the Na atoms are located in the oxygen cages defined by the two oxygen layers, and thus have the largest impact on the oxygen orbitals. Interestingly, this huge spectral broadening and low intensity might explain why some of the oxygen bands are not observed in the ARPES measurements [71, 88], not only in Na_xCoO_2, but also in most doped layered transition metal oxides, where the dopants are introduced between the oxygen layers.

In great contrast, much weaker effects of disorder are found on the Co-d orbitals (c.f.: figure 4.8(c)(e)(f)). Specifically, the a_g orbital picks up some k-*dependent* broadening near the Γ point, while the e'_g orbitals are almost unaffected by the disorder. This somewhat surprising result probably reflects the strong screening of oxygen that shields the cobalt valence orbitals from the influence of the disordered Na, and the metallic nature of the doped electrons which spread throughout the whole system. Clearly, the localization and broadening of the e'_g and a_g bands are not strong enough to shift the e'_g pockets below the Fermi level. Unlike the a_g orbital that points directly toward the doped Na atom (c.f.: figure 4.9), the e'_g orbitals neither point toward the Na atom nor the most affected O-p_z orbitals near the Na, making them the least sensitive to the presence of Na intercalants. This could also explain the negligible effects of lattice relaxation around Na atoms on the e'_g pockets. Obviously, the disorder alone does *not* destroy the six e'_g Fermi pockets of $Na_{0.3}CoO_2$, in contradiction with the claim [56, 79].

On the other hand, the Na impurities do introduce an important physical effect on the Co-d shell, namely on the crystal field splitting (the relative on-site-energy) of the e'_g and a_g orbitals. Indeed, evaluated from H^0 and $\Delta^{Na(1)}$, the crystal field splitting is found to change from 27 meV to -38 meV for Co atoms right below or above the Na intercalants, consistent with the trend estimated previously from the density of states [77]. Considering the tendency of strong orbital polarization of the many-body exchange interactions as demonstrated from the previous DMFT studies [76, 77], the combination of disorder and strong exchange interactions is very likely to give stronger scattering for the e'_g orbitals. Exactly whether this would lead to a resolution of the highly
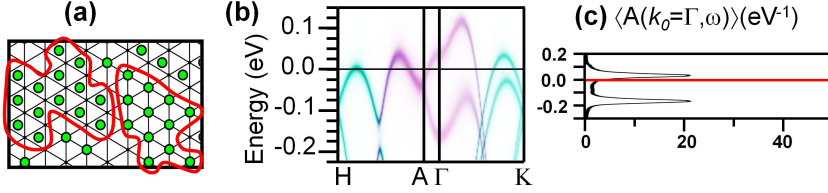
Figure 4.10: Configuration-averaged spectral function of $Na_{0.7}CoO_2$, showing short range order suppressing the spectral broadening of a_g. (a) Small islands of homogeneous Na(1) and Na(2). (b) $\langle A(k, \omega) \rangle$ around the Fermi-surface. (c) energy distribution curve at $k_0 = \Gamma$. The Wannier orbital character is labeled according to the color scheme of figure 4.5.

controversial status of the e'_g pockets of Na_xCoO_2, remains an interesting challenge to the theorists. Interestingly, our results also demonstrate a non-locality of the disorder induced self-energy. Indeed, a strongly k-dependent spectral broadening can be clearly observed in figure 4.8 that correlates well with the inverse of the band velocity rather than the energy. For example, at 25 meV the almost purely a_g bands have large ($\sim$200meV) spectral broadening near the Γ point, but negligible width at $k \sim \frac{1}{2}A\Gamma$. Such a strong k-dependence of the spectral width reflects the intrinsic non-locality of the self-energy, and highlights the advancement of our method over standard mean-field theories in which the self-energy is assumed local.

We also found effects of short-range ordering of Na impurities known to be important for the Na_xCoO_2 [68, 89]. As demonstrated in figure 4.10(a) for $Na_{0.7}CoO_2$, the exclusion of nearest neighbor Na positioning introduces automatically a strong short-range ordering of the Na impurities, due to lack of available locations at high doping (see also figure 4.7). In turn, the resulting spectral function of the a_g orbitals, for example, demonstrates stronger coherence and longer lifetime, as can be seen by comparing figure 4.10(b)(c) with figure 4.8(c)(f). (The e'_g orbitals near the pockets remain perfectly coherent also at this doping level.) This result, while physically intuitive, is actually quite non-trivial, since in the mean-field theories the degree of disorder at 0.7 doping level should be exactly the same as that at 0.3 doping level.

In conclusion, we have investigated from first principles the proposed destruction of the controversial e'_g pockets in the Fermi surface of Na_xCoO_2 due to Na disorder. To this end, we used the Wannier function-based disorder method presented in chapter 3 developed that incorporates the spatial distri-

butions of impurities beyond the mean field. The new method is benchmarked against the full DFT calculation and shown to be efficient and highly accurate. Remarkable k-dependent broadenings of the spectral function are found in the oxygen orbitals due to their vicinity to the Na intercalants. However, the effects of disorder are found to be negligible on the e'_g orbitals. Thus, the disorder alone does not destroy the e'_g pockets, in contradiction with the current claim [56, 79]. Interestingly, against the mean-field perspective, enhanced coherence is found at higher doping where short-range order grows stronger.

Chapter 5

Application 2: Room Temperature Ferromagnetism in Cu Doped ZnO

The work presented in this chapter has been published in reference [90] and was an experimental-theoretical collaboration.

5.1 Introduction

A Dilute Magnetic Semiconductor (DMS) is a non-magnetic semiconductor that is doped with a small percentage of magnetic impurities. The potential of DMS to combine magnetism for memory and semiconductors for logic has generated a lot of interest from science and industry. Specifically the DMS are thought to play an important role for spin-injection into spintronic devices such as the spin-FET [91]. [1] In 1997 Hideo Ohno [92] was the first to discover ferromagnetism in Mn doped GaAs. Unfortunately the ferromagnetic transition temperature (nowadays 190K) is too low for the envisioned industrial applications. In 2000 Thomas Dietl [93] theoretically predicted high ferromagnetic transition temperatures (some of which exceeding room temperature) for a large number of DMS (including ZnO). Dietl's prediction resulted in an ex-

---

[1]The theoretically proposed spin-FET can be turned on and off by flipping the spin of the electrons rather then pushing them in and out of the channel, a process that is much faster and takes much less energy.

plosion of publications reporting new DMS with high ferromagnetic transition temperatures. Unfortunately it turned out that many of the reported high ferromagnetic transition temperatures were the result of magnetic contamination or simply irreproducible. On the one hand this has created a lot of skepticism in the field. On the other hand there seems to be a consensus that room temperature ferromagnetism can be accomplished in dilute magnetic oxides that contain a lot of defects [94]. The current understanding of this phenomena is based on the bound magnetic polaron model [95] in which electrons trapped by the defects and the magnetic impurities form bound magnetic polarons. When the concentration of defects is sufficiently high the bound magnetic polarons percolate and form a ferromagnetically aligned state.

In this chapter we describe the experimental observation [90] of room-temperature ferromagnetism in Cu-doped ZnO by a large range of experimental techniques and the first principles calculations that led us to propose a microscopic picture of the ferromagnetism that explains the main experimental findings.

5.2   Experimental Results

Three representative films were grown: 1) a pure ZnO film, 2) Cu doped ZnO grown under ambient pressure ($P = 1 \times 10^{-3}$torr) and 3) Cu doped ZnO grown at low pressure $P = 5 \times 10^{-6}$torr. Ferromagnetism was observed only in the presence of both Cu impurities and oxygen vacancies. The ferromagnetic transition temperature was obtained from a Curie-Weiss fit of the magnetic susceptibility and found to be 750K [96], thereby far exceeding room temperature. In this section we will present the main experimental observations.

From an extensive materials characterization [96], consisting of secondary ion mass spectroscopy (SIMS), high resolution transmission electron microscopy (HR-TEM), scanning electron microscopy (SEM), the films are found to be homogeneous. The energy of the detected x-ray in the SEM and TEM is further resolved by Energy-dispersive X-ray spectroscopy (EDS) from which the elemental compositions in the SEM and TEM images can be analyzed. From the SEM-EDS and TEM-EDS on the Cu L-edge it is found that the Cu atoms are homogeneously distributed.
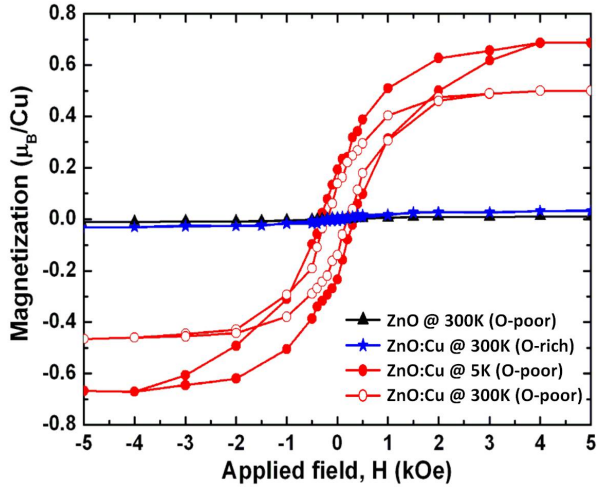
Figure 5.1: Magnetic hysteresis measured by SQUID.

In figure 5.1 the magnetic hysteresis, measured with a Superconducting Quantum Interference Device (SQUID), of the three different samples is compared. As can be seen, only the Cu doped sample that is oxygen poor is ferromagnetic with a saturated moment of $0.7\mu_B/0.5\mu_B$ and a remanence of $0.2\mu_B/0.1\mu_B$ for 5K and 300K respectively. The other two samples, the pure ZnO and the Cu doped ZnO grown at ambient pressure are not ferromagnetic, and are in fact diamagnetic [96]. This is the first evidence that only Cu dopants and oxygen vacancies together can give rise to ferromagnetism.
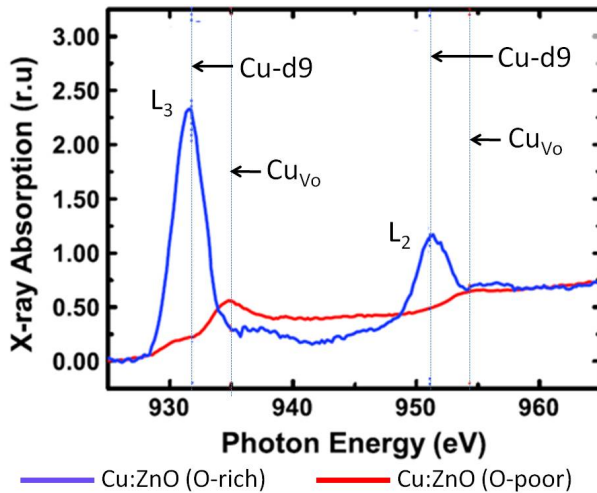
Figure 5.2: XAS on the Cu L-edge.

67

In figure 5.2 the x-ray absorption (XAS) data at the Cu L-edge of the two Cu doped samples is compared. The L-edge process involves an electron excitation from Cu-$2p$ to Cu-$3d$, causing copper to go from d^9 to the filled d-10 final state. In the oxygen rich sample we see that each of the Cu L-edges (L_3 and L_2) consist of a single peak(L_3 at 932eV and L_2 at 952 eV) which is labeled Cu-d^9. If we compare the Cu L-edge of the oxygen poor sample we see that the Cu-d^9 peaks are suppressed approximately by a factor of 7. Furthermore for each L-edge a new peak is induced which is higher in energy. The new peaks are labeled by Cu_{V_O}. Finally we notice that for the oxygen poor sample, the intensity of the Cu_{V_O} peak is roughly 4-7 times more intense then Cu-d^9 peak.
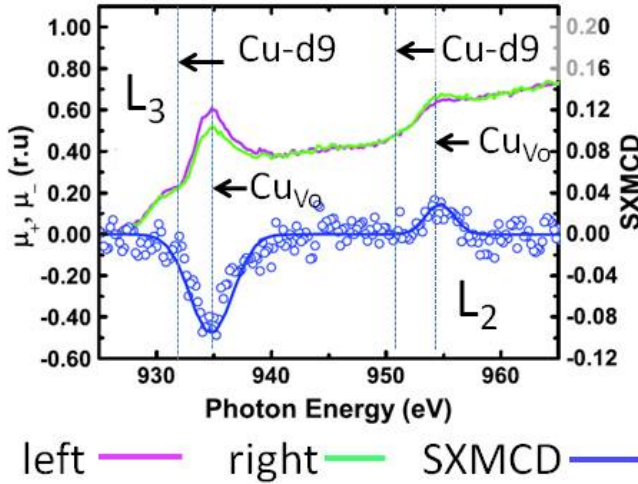
Figure 5.3: XMCD on the Cu L-edge.

In figure 5.3 the x-ray magnetic circular dichroism (XMCD) spectroscopy on the Cu L-edge of the oxygen poor sample is shown. It can be seen that only the oxygen poor sample displays an XMCD signal. More specifically, only the oxygen vacancy induced Cu_{V_O} peaks display an XMCD signal, the Cu-d^9 peaks do not.

Finally in figure 5.4 we display the XMCD signal on the oxygen K-edge (involving an excitation from O-$1s$ to O-$2p$) of the oxygen poor sample. From comparing the sign of the XMCD signal of the O K-edge with that of the Cu L_3- and L_2-edge, it can be concluded that the moment in oxygen is directed
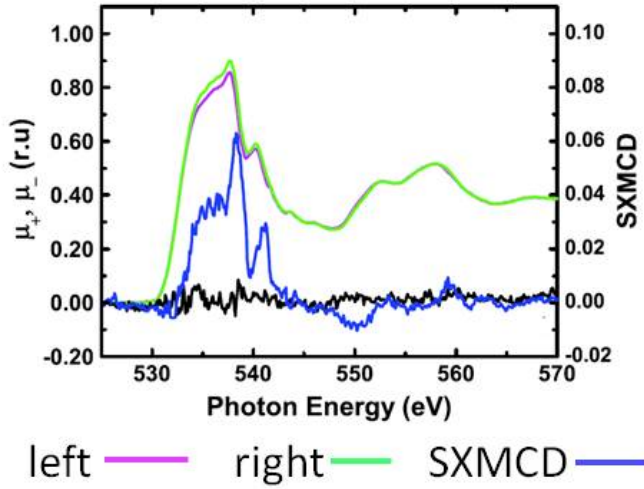
Figure 5.4: XMCD on the O K-edge.

oppositely from the moment in Cu [90].

	experiment(s)	observation
1	SQUID, XMCD	only V_O and Cu impurities together induce RTFM
2	XAS Cu L-edge	V_O suppress Cu L-edge
3	XAS Cu L-edge	V_O induces new peak $Cu_{V_O} \sim 3.4$eV higher then Cu-d^9
4	XMCD Cu L-edge	Cu_{V_O} peak displays XMCD signal, Cu-d^9 peak does not
5	XMCD O K-edge	there is an AFM aligned moment in oxygen

Table 5.1: Summary five main experimental observations

In table 5.1 we summarize once more the five main experimental findings. Together they give rise to one common question, namely what is the influence of the oxygen vacancy? To address this question we perform first principles simulations.

5.3   First Principles Simulation

In order to address the question, "what is the influence of the oxygen vacancy?", we will reformulate it. The oxygen vacancy can be thought to consist of two separate influences. To understand these let us first think about the role of oxygen in ZnO, which is to accept two electrons and thereby also to

induce a repulsive potential. Therefore an oxygen vacancy will have the opposite influence, which is to effectively donate two electrons and effectively to induce an attractive potential. Now to reformulate the question, we will add the the attractive potential of the oxygen vacancy to the system, Cu doped ZnO, and ask the question: "where will the donated electrons go?" This question is formally answered by the one-particle spectral function of Cu-doped ZnO with the attractive potential of the oxygen vacancy, but without its donated electrons.[2] To simulate the properties of ZnO from first principles is notoriously difficult and controversial. Under heavy debate for example are the first pricinciples calculation of the bandgap [97, 98] and the formation energy of oxygen vacancies [99–102]. In this work, rather then addressing these difficulties we will move around them by inserting all the experimental properties into the simulation by hand, such that we can focus on our main question: "where will the donated electrons go?" We will take into account the strong correlations in Zn-d and Cu-d by inserting a Hubbard U=8eV and Hund's coupling J=0.9eV parameters [97] into the simulation by hand within LDA+U approximation [103]. We will not calculate the formation energy of the impurities but we will insert them into the simulation by hand using the experimentally estimated values for the concentrations. We will not predict the ferromagnetism from first principles, instead we will insert it into the simulation by hand. We will not try to obtain the band gap from first principles correctly, instead we will use the scissor operation, or rather the Wannier version of it, to match the experimental band gap. Having done all of that, we are still left with one problem, namely the diluteness of the impurities, which make it necessary to use very large super cells. For example having an oxygen vacancy concentration of about 1 percent, implies that we will need a super cell that (at least) contains 100 oxygen atoms. Of course to handle the big cells is where the effective Hamiltonian method comes in.

We proceed to calculate the spectral function of Cu doped ZnO with the attractive potential of the oxygen vacancies but without the donated electrons. The low-energy Hilbert space is taken within [-10,10] eV consisting of symmetry-respecting complex Wannier orbitals of Zn-d, Cu-d, O-p and Zn-s characters (18/normal cell). The effects of impurities are extracted from three

---

[2]Actually this is not entirely correct. The one-particle spectral function calculates the probability of adding one electron and not a concentration of electrons.
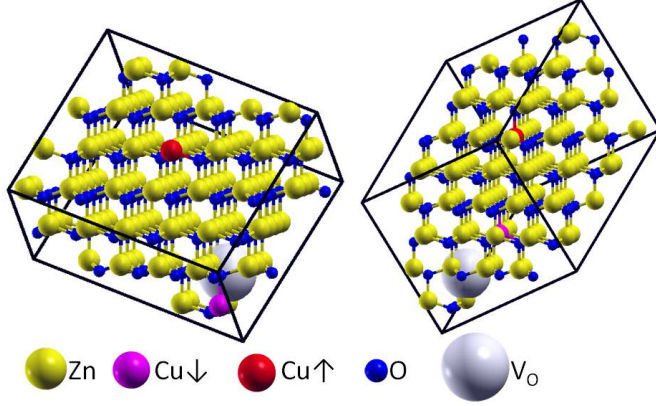
Figure 5.5: Illustration supercells used for configurational average.

DFT calculations: the undoped Zn_2O_2 in the normal cell and Zn_7CuO_8 and Zn_8O_7 in the 2×2×1 super cells. What is different from the Na_xCoO_2 case discussed in the previous chapter 4 is that the ZnO calculations were spin polarized. From the LSDA+U calculation we obtain two bandstructures, one for each spin channel, which we Wannier transform to two tight-binding hamiltonians, from which extract two impurity influences $\Delta^{Cu\uparrow}$ and $\Delta^{Cu\downarrow}$. Then when constructing the effective Hamiltonian depending on whether a Cu impurity has the spin in the minority/majority direction, we apply $\Delta^{Cu\uparrow}/\Delta^{Cu\downarrow}$ to the minority effective Hamiltonian and $\Delta^{Cu\downarrow}/\Delta^{Cu\uparrow}$ to the majority effective Hamiltonian. A 2 eV correction to the on-site energy of the Zn-s orbitals was added to counter the self-interaction problem and to reproduce the physical size of the band gap of 3.4eV [104]. For the configurational average, 10 super cells were used with different shapes, orientation and size (containing 94.8 Zn atoms on average). This change of the supercell boundaries is much more important than in the case of Na_xCoO_2, since the concentrations of impurities is so dilute. The small amount of disordered impurities in the simulation is not as efficient in washing out artificial gap openings in the spectral function at the configuration-supercell zone boundaries. Within in each cell 1 oxygen vacancy and 2 Cu impurities were randomly distributed. The moments of the Cu ions that are nearby the oxygen vacancy were aligned ferromagnetically, while the Cu ions beyond a certain radius were orientated randomly. This radius was chosen in such a way that the average moment agrees with the remanence of 0.4 μ_B as measured by the SQUID. In figure 5.5 two of such supercells are

illustrated.
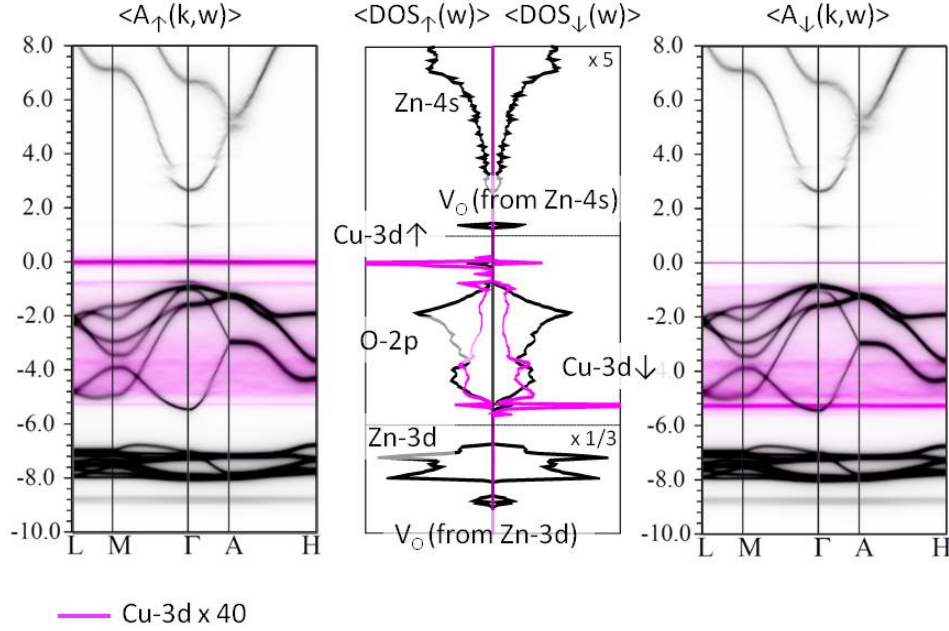
Figure 5.6: Configurational-averaged spectral function of Cu doped ZnO, with $\sim 2\%$ Cu impurities and $\sim 1\%$ of O vacancies (without their donated electrons) within the "LDA+U" approximation. The intensity of the Cu-3d band has been marked with a pink color and multiplied by a factor of 40 to make the impurity states more visible. For the same reason, the intensity of the DOS panels [-10eV, -6eV] and [1eV, 8eV] have been rescaled by a factor of 1/3 and 5 respectively.

The resulting spectral function $\langle A(k,\omega) \rangle$ is illustrated in figure 5.6. On the left side the spin minority is shown and on the right side the spin majority and in the middle the density of states. The valence band consists of O-p and the conduction band of Zn-s. The pink intensity correpsonds to the spectral weight of Cu$-d$ and is enhanced by a factor 40 to make it more visible. The Cu impurity level is splitted in an Cu upper Hubbard level within the band gap and a Cu lower Hubbard that is at the bottom of the O-p band. [3] Most

---

[3] Note that the Cu upper Hubbard level is actually double degenerate. The tetrahedral coordination of the oxygens around the Zn/Cu atoms results in a splitting between e_g and t_{2g}. The stretching of the tetrahedron along the z-axis in the wurtzite lattice further splits the t_{2g} resulting into the doublet. Finally the small crystal field splittings will be dramatically enhanced by the enormous Hubbard U of 8eV.

interesting is the feature above the pink Cu upper Hubbard level the intensity of which corresponds to the oxygen vacancy state as we shall further discuss.

Before discussing the impurity levels let us first note that the upper and lower Hubbard level are not fully spin polarized. Of course this is not surprising because as mentioned a fraction of the moments were chosen to be randomly orientated. However, this result is in contradiction with a common misconception that LDA+U cannot describe a paramagnetic insulator. This latter statement is only true if a small cell is used. If a bigger supercell is used, that allows for the right ensemble, a PM-insulator can also be described within LDA+U.

Now let us go back to the original question: "where does the electron go?" As we can see the Cu upper Hubbard level is about 1.5eV lower in energy than the oxygen vacancy level. Therefore the electrons will go into the Cu upper Hubbard level leaving the oxygen vacancy state empty. This means that the bound magnetic polaron picture [95] in which a down electron in the oxygen vacancy level forms a bound magnetic polaron with an up electron in the Cu does not apply, since there is no down electron in the oxygen vacancy level.

So we looked at the energy levels of the impurity states, now what about their wave function? For this information we take a closer look at the k-dependence of the spectral function. If we look at the Cu upper Hubbard level, we see that its intensity spreads out over the entire Brillouin zone , which means that in real space its wave function is localized within one unit cell. On the other hand if we look at the oxygen vacancy level, we notice that its intensity is only around Γ, which means in real space that its wave function spreads out over multiple unit cells. To be more specific, the full width at half maximum of the intensity is roughly $\sim 1/5\Gamma M$, which by a simple Fourier transform H can be estimated to correspond in real space to a wave function with a radius of about 2.25 lattice constants (see appendix H).

Finally let us understand why the oxygen vacancy state is so big. Remember that the oxygen vacancy state has two influences, besides donating two electrons it will also induce an attractive potential. This attractive potential will be most dramatic in the four neighboring zinc atoms. With this in mind we now identify the oxygen vacancy state consisting of the four neighboring

Zn-s states whoses energy is lowered by the attractive potential:

$$|V_O\rangle \propto |\text{Zn1} - \text{s}\rangle + |\text{Zn2} - \text{s}\rangle + |\text{Zn3} - \text{s}\rangle + |\text{Zn4} - \text{s}\rangle \tag{5.1}$$

Note that we identified the oxygen vacancy state as being a symmetric combination of Zn-s states. This is because the oxygen vacancy states has most of the spectral weight at Γ as can be seen from 5.6. Also note that there are more than one kind of "oxygen vacancy state". For example the flat level around -9eV corresponds are clearly derived from the Zn-d states at [-7eV,-6eV]. The Zn-d "oxygen vacancy states" however have their spectral weight extending over the entire Brillouin zone indicating that they are localized in one unit cell. This is of course because the Zn-d Wannier functions, unlike the Zn-s Wannier functions, are very localized. Another "oxygen vacancy state" can be found around -0.8eV in the spin minority spectral function which is derived from the Cu upper Hubbard level.

5.4   Microscopic Picture of the Ferromagnetism

The main findings from the first principles simulation are 1) the electrons donated by the oxygen vacancy will go into the Cu upper Hubbard level and 2) that the oxygen vacancy states are big. From these two findings we can construct the following picture. Without the oxygen vacancies there are lot of magnetic moments but they are isolated and therefore dont talk to each other and do not form a ferromagnetic state. With the oxygen vacancies a lot of the Cu-d^9 states will be filled turning them into seemingly magnetically inert Cu-d^{10} states. However some of the Cu-d^9 states remain unoccupied and therefore some of the moments remain. Due to the large radius of the oxygen vacancy states, most of the Cu-d^9 and Cu-d^{10} states will now be connected allowing them to form a coherent many-body state. If the moments in the Cu-d^9 states align ferromagnetically this many-body state can gain kinetic energy from hopping through the oxygen vacancy states, like depicted in the cartoon to the right of figure 5.7. With this picture in mind let us now go back to the five main experimental observations that were summarized in table 5.1:

1. The picture explains why one needs oxygen vacancies for the ferromag-
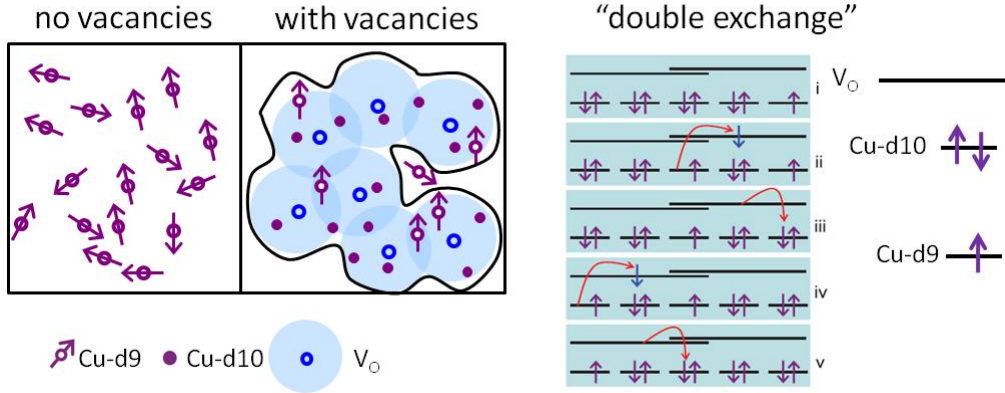
Figure 5.7: Microscopic picture of the ferromagnetism. (Left) The light blue circles represent the size of the vacancy orbitals within which Cu atoms receive two doped electrons per V_O and their moments are aligned ferromagnetically. (Right) Example of the hopping process that will lower the kinetic energy with snapshots in panel (i)-(v). The long lines represent two overlapped V_O orbitals. The short lines below represent individual Cu ions inside the blue circles (V_O orbitals) with its upper Hubbard band fully filled (Cu-d^{10}) or partially filled (Cu-d^9). The red arrows illustrate the spin-polarized electron hopping process.

netic state to form, because without those the Cu-d^9 moments can not talk to each other.

2. The fact that most of the Cu-d^9 are filled by the donated electron and turned into Cu-d^{10} explains why the Cu-L edge is suppressed because the donated electron will Pauli block the Cu-$2p$ to Cu-$3d$ excitation.

3. The observed oxygen vacancy induced peak labelled as Cu_{V_O} is indentified with ferromagnetic many-body state. Its higher energy is attributed to the repulsion of the donated electrons.

4. The remaining Cu-d^9 peak is associated with the Cu-d^9 states that are spatially too far from the oxygen vacancy states to participate in the ferromagnetic many-body state. These states will remain paramagnetic which explains why they show no signal in the XMCD measurement.

5. As can be see from figure 5.7, the hopping process that is stabilizing the ferromagnetic moment, necessarily has the moments in Cu-d^9 oriented in opposite direction of the moments in the oxygen vacancies. Since the

oxygen vacancies hybridize with the O-2p states this explains why an opposite XMCD signal was observed in the O K-edge.

5.5 Conclusion

Room temperature ferromagnetism has been observed in oxygen deficient Cu doped ZnO. Neither ZnO or Cu doped ZnO displays magnetic hysteresis indicating that the oxygen vacancies play a critical role in the formation of the ferromagnetic state. To investigate the role of the oxygen vacancies we apply the Wannier function based disorder methods presented in chapter 3 to compute the configuration averaged spectral function of oxygen deficient Cu doped ZnO. The main findings are that the electrons donated by the oxygen vacancies will go to the Cu-d^9 states and that the oxygen vacancies will turn Zn-s states into large sized oxygen vacancy states. Based on these findings we propose a picture of the ferromagnetism that explains all the main experimental findings.

Chapter 6

Application 3: Carrier Doping and Charge Localization in Transition Metal Doped Iron Based Superconductors

The work presented in this chapter is based on unpublished work in progress.

6.1 Introduction

Doping is one of the most powerful ways of tuning the electronic properties of functional materials. As we discussed in chapter 1, the influence of doping in general consists of several effects: to introduce carriers, to vary the chemical pressure and to introduce quenched disorder. Disentangling the influences of such effects is important for a scientific understanding and further improving of the desired functional properties.

In this respect, the discovery that isovalent substitutions in $FeTe_{1-x}Se_x$ [105], $BaFe_2(As_{1-x}P_x)_2$ [106] and $Ba(Fe_{1-x}Ru_x)_2As_2$ [107] can induce superconductivity provided an important clue: it seems to suggest that carrier doping is perhaps not an essential tuning parameter in iron based superconductors. The role of carrier doping, or rather its absence, took yet another turn when [108] reported from a density functional theory (DFT) study that the doped electrons in $Ba(Fe_{1-x}M_x)_2As_2$ and $Fe_{1-x}M_x Te$, with M=(Co, Ni, Cu, Zn, Ru, Rh,

and Pd) are fully localized at the transition metal dopant site. This lead [108] to the surprising conclusion that the non-isovalent TM substitions do not dope carriers into the iron based superconductors. If this conclusion was indeed correct it would be a significant contribution towards the understanding of Fe based superconductors.

The reported absence of carrier doping in non-isovalent TM substitions in iron based superconductors however, seems to be in contradiction with several experimental observations and theoretical calculations. From angle resolved photoemission spectroscopy (ARPES) it was found [109, 110] that the non-isovalent substitutions $Ba_{1-x}K_xFe_2As_2$ and $Ba(Fe_{1-x}Co_x)_2As_2$ induce a chemical potential shift consistent with the doping of hole and electron cariers. From Hall measurements [111] it was found in $Ba(Fe_{1-x}Ni_x)_2As_2$ that for large dopings the Hall number is proportional to $2x$, confirming that each Ni donates two electrons. Furthermore, from theoretical calculations [109, 110, 112] within the same framework of DFT, a systematic rigid shift of the band structure around the Fermi level was found consistent with carrier doping. Together these experimental and theoretical findings raise the following question: do the non-isovalent substitutions dope carriers into the iron based superconductors and if so how can this be reconciled with the doped electron being fully localized at the TM dopant site?

In this chapter we reproduce both the carrier doping and the charge localization for in Co doped $BaFe_2As_2$ and explain the apparent contradiction. Furthermore we investigate Zn doped $BaFe_2As_2$ in order to contrast the influence of the weak impurity potential of Co with the strong impurity potential of Zn. Due to some technical constraints, at the time of writing this thesis we are not capable of calculating the Fermi surface of disordered systems. Therefore the first part of the analysis in which the Fermi surface is calculated, we approximate the disordered Co's within the commonly used [108, 109] small supercell approximation which allows for the use of ordinary DFT. In the second part of the analysis we compute the disordered bandstructures of Co and Zn doped $BaFe_2As_2$ using the effective Hamiltonian method described in section 3.3.
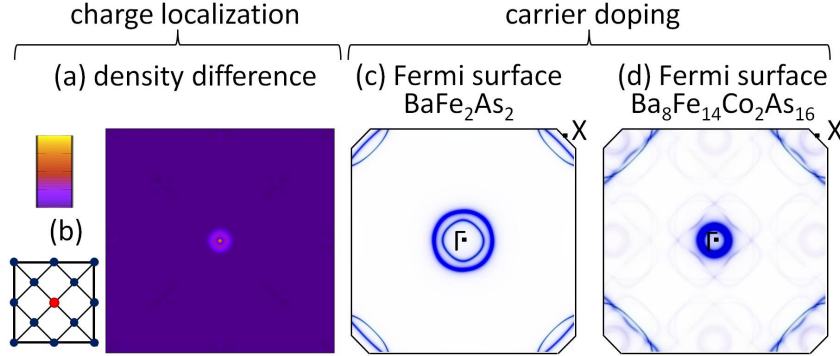
6.2 Ordered Dopant Analysis

Figure 6.1: Two seemingly contradicting results, charge localization and carrier doping, obtained from DFT simulations of $BaFe_2As_2$ and $Ba_8Fe_{14}Co_2As_{16}$. (a) density difference plot between $BaFe_2As_2$ and $Ba_8Fe_{14}Co_2As_{16}$, showing the doped electron to be fully localized at the Co site. (b) atomic positions of Fe(blue) and Co(red) in relationship to the contour plot. From comparing (c) the Fermi surface of $BaFe_2As_2$ and (d) the Fermi surface of $Ba_8Fe_{14}Co_2As_{16}$ (unfolded to the normal cell Brillouin zone), carier doping is observed: the hole pocket at Γ is shrinking where as the electron pocket at X is growing.

To investigate the influence of non-isovalent transition metal substitutions in iron based superconductors, we focus on $Ba(Fe_{1-x}Co_x)_2As_2$. Specifically we performed DFT calculations [113] on two unit cells: the undoped normal cell $BaFe_2As_2$ and the doped $x = 1/8$ supercell $Ba_8Fe_{14}Co_2As_{16}$ that was also studied by [108] and is depicted in figure 1(b). In figure 1(a) the density of the doped and undoped case are compared by plotting the density difference in the lower Fe_7Co plane (see figure 1(b)), integrated from 1.32Å(roughly corresponding to the atomic radius of Fe and Co) below the plane to 1.32Å above the plane in the direction perpendicular to the plane. In agreement with [108], we find that the doped electron is entirely localized around the Co, seemingly implying that Co does not dope carriers.

Next we investigate the influence of Co doping on the Fermi surface by using of the unfolding method presented in section 3.2. By representing the spectral function $A(k, \omega = \varepsilon_f)$ of the super cell configuration on the normal cell k-basis, we can remove the artificial band folding effect from our arbitrary choice of super cell and better focus on the influence of the Co dopant. Furthermore the spectral function on the normal cell k-basis can be directly compared with the

ARPES experiments as discussed in 3.2.1. From comparing the Fermi surface of the undoped (figure 6.1(c))and doped (figure 6.1(d)) case, we clearly see that the hole pocket at Γ is shrinking and the electron pocket at X is growing, in other words that Co substitution is doping electron carriers, in agreement with the previous experimental [109–111] and theoretical findings [109, 110, 112]. We note that the sharp shadow Fermi sheets and the gap-openings in the unfolded Fermi surface (figure 6.1(d)) are an artifact of the smallness of the supercell and that in a crude way represent the scattering strength of the Bloch states from the disordered Co impurities.
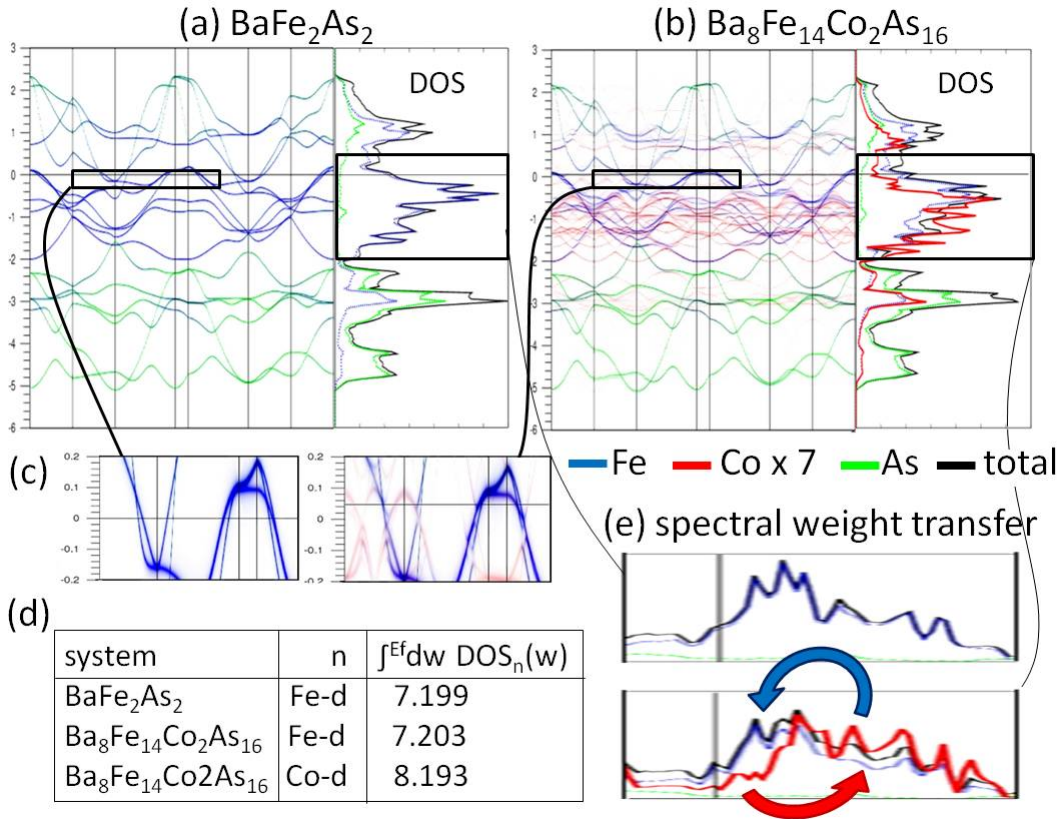
Figure 6.2: Comparing the bandstructures of $BaFe_2As_2$ and $Ba_8Fe_{14}Co_2As_{16}$. The orbital resolved density of states (DOS) showing Co/Fe spectral weight transfer to the lower/higher (more/less occupied) frequencies. Carrier doping is again confirmed by comparing the bandstructure of $BaFe_2As_2$ with the bandstructure $Ba_8Fe_{14}Co_2As_{16}$ (unfolded to the normal cell Brillouin zone) around the Fermi surface.

To reconcile the seemingly contradicting charge localization and electron

doping obtained in our first principles analysis of $Ba(Fe_{1-x}Co_x)_2As_2$, we will now focus on the frequency dependence of the Wannier orbital n resolved spectral function $A_n(k,\omega)$ and its k integration, i.e. the orbital n resolved density of states $DOS_n(\omega)$. In figure 6.2 we show the spectral functions of the undoped (figure 6.2(a)) and doped (figure 6.2(b)) spectral functions and represent the Wannier orbitals by different colors: blue for Fe and red for Co. We enhance the intensity of the Co-character by a factor 7, such that we directly compare it with the Fe character.

First of all, we establish once again what we already know. If we zoom in around the Fermi energy(figure 6.2(c)), we see that the Co substitution clearly electron dopes the system: the hole pocket at Γ shrinks and the electron pocket at X grows. At the same time if we compare the occupied orbital resolved spectral weights (figure 6.2(d)) we see that the occupation of the Fe spectral weight remains constant under substitution and that the Co spectral weights contain the doped electron. However, if we now focus on the frequency dependence of the orbital resolved density of states(figure 6.2(e)) it becomes clear how charge localization and carrier doping can coexist. On the one hand the Co spectral weight (red) is transferred from the higher unoccupied to the occupied frequencies and for the Fe spectral weight (blue) the opposite is happening. For example around the Fermi level the spectral weight contains more Fe character than 7 times the amount of Co character. This will obviously result in a larger spectral weight occupation for Co than for Fe. However somewhat below the center of mass of the Fe band, around -4eV, the spectral weight contains less Fe than 7 times the amount of Co character. On the other hand the total DOS is remaining more or less constant, meaning that adding electrons will result in raising the chemical potential. The spectral weight transfer explains the coexistence of charge localization and the carrier doping, but it raises yet another question, what is its origin?

To get an understanding of the spectral weight transfer, we will now consider a very simple model and assess qualitatively the consequence of Bloch states being coupled by an attractive potential. Specifically we consider a one-dimensional one band tight binding model and periodically introduce a negative onsite shift for 1 out of 8 sites, corresponding to the donor impurity substitution. We focus our attention further on two particular unperturbed
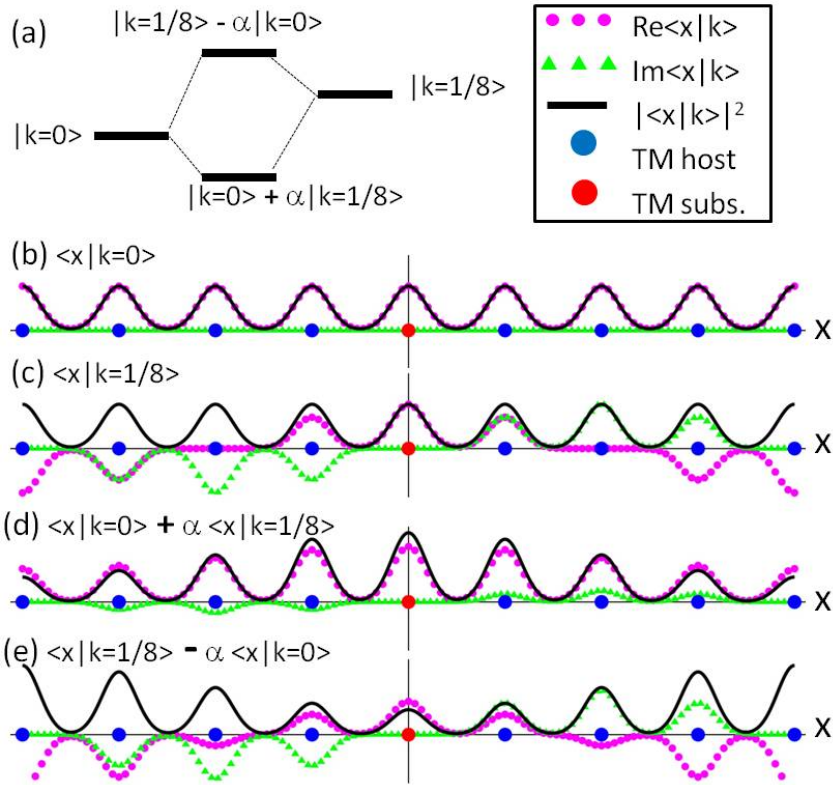
Figure 6.3: Simple cartoon to explain the coexistence of charge localization and carrier doping, where (b) and (c) are the unperturbed states and (d) and (e) are the true states of the perturbed system. The host/impurity spectral weight transfer to higher/lower energy happens naturally as the consequence of Bloch states mixing by an attractive impurity potential.

Bloch states at the bottom of the band: one non-propagating state $|k{=}0\rangle$ and one propagating state $|k{=}1/8\rangle$. The real, imaginary and absolute value squared of these unperturbed wave functions are illustrated in figure 6.3(b) and 6.3(c) respectively. If for convenience we chose our origin at the donor impurity site, the matrix element coupling those two states will be real and negative: $\langle k{=}0|\Delta|k{=}1/8\rangle < 0$. This coupling will result in a lower energy bonding state $|k{=}0\rangle + \alpha|k{=}1/8\rangle$ and a higher energy anti-bonding state $|k{=}1/8\rangle - \alpha|k{=}0\rangle$, where $\alpha > 0$, as illustrated in figure 6.3(a). If we now focus on the wave functions of bonding and anti-bonding states, we can understand the spectral weight transfer. For example if we look at the energetically lower bonding state, we see that at the donor impurity site the interference of the propagating $|k{=}1/8\rangle$ and non-propagating $|k{=}0\rangle$ state is maximally constructive, while 4 sites away from the donor impurity, the interference of the propagating and non-propagating state is maximally destructive. In other words, under the influence of the attractive potential the energetically lower Bloch state is losing host character (Fe) and gaining impurity character (Co). For the energetically higher anti-bonding state the character change is opposite. Of course the above picture is highly oversimplified compared to the realistic first principles Bloch states, but as long as the coupling potential Δ is weak compared with the bandwidth W it is qualitatively correct.

6.3 Disordered Dopant Analysis

In the previous section we found that the impurity potential of Co remixes the Co and Fe characters in the bands, but that it is too weak to remove Bloch states from the hole and electron pockets. It is therefore very interesting to contrast the weak Co impurity potential with the strong Zn impurity potential such as was also investigated by [109] for Zn doped LaFeAsO and [108] for Zn doped $BaFe_2As_2$. To investigate the influence of disordered impurities with strong impurity potentials such as induced by Zinc, it is essential to go beyond the small supercell approximation that we have been applying so far in this chapter and that has been applied in the literature [108, 109]. The periodic potential of the strong impurity potentials will induce gap openings and shadow bands that strongly depend on the artificial choice of the supercell. Therefore

we now continue the analysis using the effective Hamiltonian to treat disorder properly with big supercells. The high quality of the effective Hamiltonian for Zn doped BaFe$_2$As$_2$, was already demonstrated in section 3.3.4. A similar high quality is found for the effective Hamiltonian of Co doped BaFe$_2$As$_2$. We perform for both Co and Zn doped BaFe$_2$As$_2$ a configurational average over 10 supercells with different shapes, orientations and size, containing 140 Fe and 20 Co/Zn atoms on average. The resulting configuration-averaged spectral functions are displayed in figures 6.4 and 6.5.
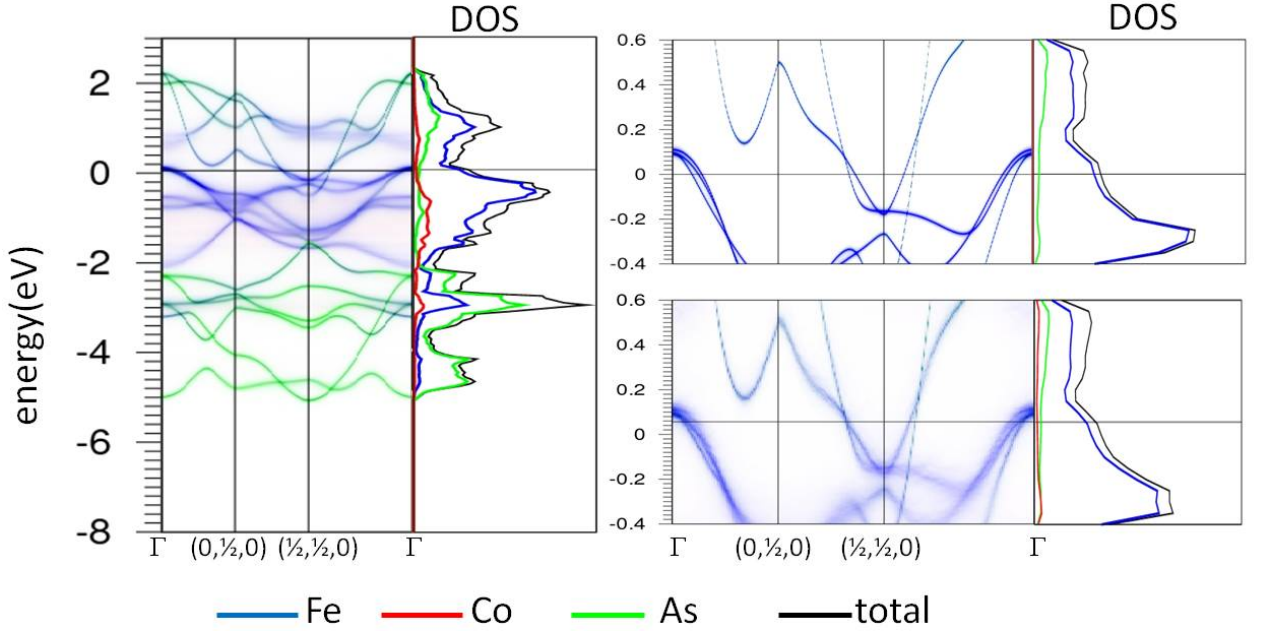
Figure 6.4: Configuration averaged spectral function and density of states of Ba(Fe$_{7/8}$Co$_{1/8}$)$_2$As$_2$ (Left) in the entire low energy Hilbert space, (Right down) around the Fermi energy and of (Right up) BaFe$_2$As$_2$.

First let us look at Co doped BaFe$_2$As$_2$ in figure 6.4. We once again reconfirm the findings of the previous section, namely a growth of the electron pocket at $k = (\frac{1}{2}, \frac{1}{2}, 0)$ and a shrinkage of the hole pocket at Γ and a spectral weight shift downward in energy of Co with respect to Fe. If we focus on the Co weight we see no indication of localized Co impurity states. Instead we see a structureless blurry Co region with a "band width" that follows the band width of the Fe band complex. This indicates that each of the Fe Bloch states in the "blurry Co region" roughly speaking picks up an equal amount of Co character. This again indicates that the localized charge at the Co site does not

84

belong to one localized impurity state but to many Bloch states instead. We notice the absence of the "Co blur" at the bands at the Fermi surface and also that these bands remain relatively sharp and coherent contrary to the scenario of a "washed out Fermi surface" that was suggested in reference [108].
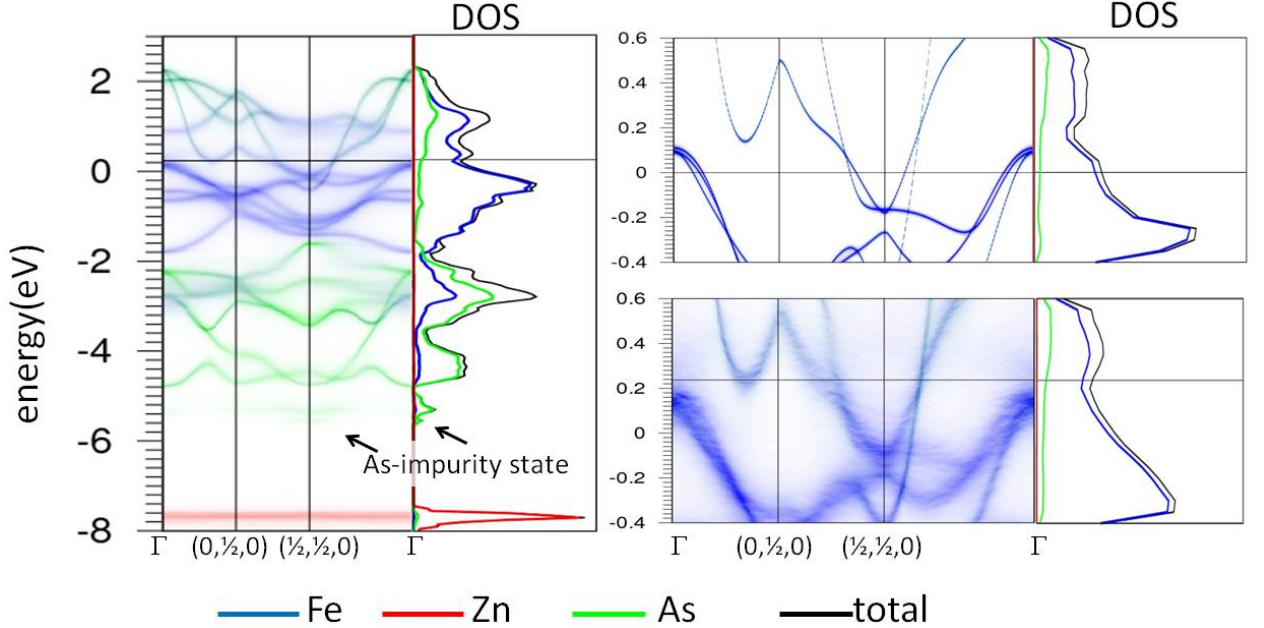
Figure 6.5: Configuration averaged spectral function and density of states of $Ba(Fe_{1-x}Zn_x)_2As_2$ (Left) in the entire low energy Hilbert space, (Right down) around the Fermi energy and of (Right up) $BaFe_2As_2$.

Now we turn our attention to Zn doped $BaFe_2As_2$. Clearly the impurity potential of Zn is capable of removing carriers from the hole pockets and electron pockets. A strong shift of -8eV completely removes the Zn-d states from the Fe-d/As-p band complex. The Zn-d impurity states are very flat indicative of localization. [1] Despite the removal of Zn-d states we find in agreement with [109] that the Zn substitutions again dope electron carriers. If we zoom in on the Fermi level we see that the electron pocket at $k = (\frac{1}{2}, \frac{1}{2}, 0)$ grows, that the hole pocket at Γ sinks below the Fermi level and that a new electron pocket is forming around $k = (0, \frac{1}{2}, 0)$. The number of doped carriers is the result of the additional doped electrons from Zn, the removal of Fe states, and the change of the density of states under the influence of the disordered

[1]The Zn-d impurity states do not overlap with the semi-core states As-p at -11eV and Ba-p at -13.5eV

85

impurities. To separate the relative importance of all these influences is left for future investigations.

It is important to keep in mind that when counting the number of carriers in a disordered band structure, one cannot only rely on the size of the hole and electron pockets in k-space. For this specific case of Zn doped $BaFe_2As_2$ for example it should not be forgotten that 1/8 of the Fe spectral weight is removed from the Fe-d/As-p complex. One could expect that the bands decreased their intensity by a same amount. However, if we compare the DOS of Zn doped and undoped $BaFe_2As_2$ around the Fermi surface we see that the DOS in that region is roughly speaking constant, meaning that the disordered bands around the Fermi surface roughly contain the same amount of states as the ordered ones. Of course the big difference is that the states in the disordered bands are very decoherent with big broadenings in momentum and frequency corresponding to small scattering lengths and small lifetimes.

Finally we want to point out an interesting impurity state emerging from the As bands around $k = (\frac{1}{2}, \frac{1}{2}, 0)$ and -5eV. This state is induced by the attractive potential of Zn impurity in the neighboring As atoms. The whole situation is very reminiscent of the oxygen vacancy states in chapter 5, where the Zn substitution plays the role of the oxygen vacancy and the As impurity state the role of the oxygen vacancy state. In analogy with the oxygen vacancy state the intensity of the As impurity state spreads over a small region in k-space implying that in real space it spans over multiple normal cells. What is different though is that unlike the oxygen vacancy state, the As impurity state is not at Γ, but around $k = (\frac{1}{2}, \frac{1}{2}, 0)$, implying that it is not a simple symmetric combination of As states, but a mixture with a complex phase. The As impurity state demonstrates the value of the effective Hamiltonian method presented in this thesis over the common practice of focusing on a few numbers (onsite energy, nearest neighbor hopping). It has only been discovered because all the influences of the impurity (all the matrix elements of $\langle rn|\Delta|r'n'\rangle$) have been included in the analysis.

Bibliography

[1] S. Curtarolo *et al. Phys. Rev. Lett.* **91** (2003) 135503.

[2] P. W. Anderson *Phys. Rev.* **109** (1957) 1492.

[3] M. Tinkham, *Introduction to Superconductivity*. Mcgraw-Hil, New York, 1996.

[4] A. A. M. Pruisken, *Field theory, scaling and the localization problem*, in *The Quantum Hall Effect* (R. E. Prange and S. M. Girvin, eds.), ch. 5, p. 117. Springer, Berlin, 1987.

[5] P. W. Anderson *Phys. Rev.* **124** (1961) 41.

[6] S. S. M. Milovanovic and R. N. Bhatt *Phys. Rev. Lett.* **63** (1989) 82.

[7] P. A. Wolff *Phys. Rev.* **124** (1961) 1030.

[8] T.-M. Chuang *et al. Science* **327** (2010) 181.

[9] E. Dagotto *Science* **309** (2005) 257.

[10] J. Kohanoff and N. Gidopoulos, *Density functional theory: Basics, new trends and applications*, in *Handbook of Molecular Physics and Quantum Chemistry* (S. Wilson, ed.), ch. 26, p. 532. John Wiley and Sons, Chichester, 2003.

[11] R. M. Dreizler and E. K. U. Gross, *Density Functional Theory: An approach to the Many-Body Problem*. Springer-Verlag, 1990.

[12] S. Cottenier, *Density functional theory and the family of (l)apw-methods: a step-by-step introduction*, 2002.

[13] D. Singh and L. Nordström, *Planewaves, Pseudopotentials and the LAPW method.* Springer, second ed., 2006.

[14] R. M. Martin, *Electronic Structure: Basic Theory and Practical Methods.* Cambridge University Press, 2004.

[15] W. Kohn *Rev. Mod. Phys.* **71** (1999) 1253.

[16] P. Hohenberg and W. Kohn *Phys. Rev.* **136** (1964) 864.

[17] W. Kohn and L. J. Sham *Phys. Rev.* **140** (1965) 1133.

[18] J. P. Perdew and A. Zunger *Phys. Rev. B* **23** (1981) 5048.

[19] D. M. Ceperley and B. J. Alder *Phys. Rev. Lett.* **45** (1980) 566.

[20] M. Levy, J. P. Perdew, and V. Sahni *Phys. Rev. A* **30** (1984) 2745.

[21] T. Yoshida *J. Phys. Condens. Matter* **19** (2007) 125209.

[22] W. Meevasana *et al. Phys. Rev. B* **77** (2008) 104506.

[23] D. H. Lu *et al. Nature* **81** (2008) 455.

[24] M. Yi *et al. Phys. Rev. B* **80** (2009) 024515.

[25] J. M. Luttinger *Phys. Rev.* **119** (1960) 1153.

[26] W.-G. Yin, D. Volja, and W. Ku *Phys. Rev. Lett.* **96** (2006) 116405.

[27] C.-C. Lee, W.-G. Yin, and W. Ku *Phys. Rev. Lett.* **103** (2009) 267001.

[28] J. C. Slater *Phys. Rev.* **51** (1937) 846.

[29] O. K. Andersen *Phys. Rev. B* **12** (1975) 3060.

[30] P. Blaha *et al. Comput Phys. Commun.* **147** (2002) 71.

[31] F. Giustino *et al. Phys. Rev. Lett.* **98** (2007) 047005.

[32] R. D. King-Smith and D. Vanderbilt *Phys. Rev. B* **47** (1993) 1651.

[33] T. Thonhauser, D. Ceresoli, D. Vanderbilt, and R. Resta *Phys. Rev. Lett.* **95** (1993) 137205.

[34] R. L. Barnett, A. Polkovnikov, E. Demler, W.-G. Yin, and W. Ku *Phys. Rev. Lett.* **96** (2006) 026406.

[35] A. C. Walters, T. G. Perring, J. S. Caux, A. Savici, G. D. Gu, C. C. Lee, W. Ku, and I. Zaliznyak *Nat. Phys.* **5** (2009) 867.

[36] A. Calzolari, N. Marzari, I. Souza, and M. B. Nardelli *Phys. Rev. B* **69** (2004) 035108.

[37] V. I. Anisimov *et al. Phys. Rev. B* **71** (2005) 125119.

[38] C. Weber, K. Haule, and G. Kotliar *Phys. Rev. B* **78** (2008) 134519.

[39] F. Lechermann *Phys. Rev. Lett.* **102** (2009) 046403.

[40] C.-C. Lee, H. C. Hsueh, and W. Ku *Phys. Rev. B* **82** (2010) 081106(R).

[41] W.-G. Yin and W. Ku *Phys. Rev. B* **79** (2009) 214512.

[42] X. Deng, X. Dai, and Z. Fang *Europhys. Lett.* **83** (2008) 37008.

[43] W. Kohn *Phys. Rev.* **115** (1959) 809.

[44] D. J. Thouless *J. Phys. C* **17** (1984) L325.

[45] C. Brouder, G. Panati, M. Calandra, C. Mourougane, and N. Marzari *Phys. Rev. Lett.* **98** (2007) 046402.

[46] N. Marzari and D. Vanderbilt *Phys. Rev. B* **56** (1997) 12847.

[47] W. Ku *et al. Phys. Rev. Lett.* **89** (2002) 167204–1.

[48] I. Mayer *International Journal of Quantum Chemistry* **90** (2002) 63.

[49] W. Ku, T. Berlijn, and C.-C. Lee *Phys. Rev. Lett.* **104** (2010) 216401.

[50] V. Popescu and A. Zunger *Phys. Rev. Lett.* **104** (2010) 236403.

[51] T. Berlijn, D. Volja, and W. Ku *Phys. Rev. Lett.* **106** (2011) 077005.

[52] E. N. Economou, *Green's Functions in Quantum Mechanics.*

[53] A. Gonis, *Green Functions for Ordered and Disordered Systems.* North Hollad, Amsterdam, 1992.

[54] N. W. Ashcroft and N. D. Mermin, *Solid State Physics.* Holt, Rinehart, and Winston, New York, 1976.

[55] M. Lindroos, S. Sahrakorpi, and A. Bansil *Phys. Rev. B* **65** (2002) 054514.

[56] D. Singh *et al. Phys. Rev. Lett.* **97** (2006) 016404.

[57] D. Pillay *et al. Phys. Rev. Lett.* **101** (2008) 246808.

[58] C. H. Bates, W. B. White, and R. Roy *Science* **137** (1962) 993.

[59] S. Desgreniers *Phys. Rev. B* **58** (1998) 14102.

[60] M. J. Frisch *et al.*, "Gaussian 09." Revision A.1,Gaussian Inc. Wallingford CT 2009.

[61] V. Blum *et al. Comput. Phys. Commun.* **180** (2009) 2175.

[62] M. Rotter, M. Tegel, and D. Johrendt *Phys. Rev. B* **78** (2008) 020503(R).

[63] K. Takada *et al. Nature* **422** (2003) 53.

[64] G.-Q. Zheng *et al. J. Phys.: Condens. Matter* **18** (2006) L63.

[65] M. L. Foo *et al. Phys. Rev. Lett.* **92** (2004) 247001–1.

[66] I. Terasaki *et al. Phys. Rev. B* **56** (1997) R12685.

[67] S. P. Bayrakci *et al. Phys. Rev. Lett.* **94** (2005) 157205.

[68] H. W. Zandbergen *et al. Phys. Rev. B* **70** (2004) 024101.

[69] D. Singh *Phys. Rev. B* **61** (2000) 13397.

[70] M. Hasan *et al. Phys. Rev. Lett.* **92** (2004) 246402.

[71] H.-B. Yang *et al. Phys. Rev. Lett.* **95** (2005) 146401.

[72] L. Balicas *et al. Phys. Rev. Lett.* **97** (2006) 126401.

[73] R. G. Ueland *et al. Physica C* **402** (2004) 27.

[74] J. Laverock *et al. Phys. Rev. B* **76** (2007) 052509.

[75] A. Liebsch *et al. Eur. Phys. J. B.* **61** (2008) 405.

[76] F. Lechermann *et al. Prog. Theo. Phys. Supp.* **160** (2005) 233.

[77] C. Marianetti *et al. Phys. Rev. Lett.* **98** (2007) 176405.

[78] D. Pillay *et al. Phys. Rev. B* **78** (2008) 012501.

[79] D. Singh *et al. Solid State Sciences* **9** (2007) 604.

[80] Q. Huang *et al. Phys. Rev. B* **70** (2004) 184110.

[81] J. Lynn *et al. Phys. Rev. B* **68** (2003) 214516.

[82] L. Viciu *et al. Phys. Rev. B* **73** (2006) 212107.

[83] V. Poltavets *et al. Phys. Rev. B* **74** (2006) 125103.

[84] C. Lin *et al. J. of Crystal Growth* **292** (2006) 422.

[85] G. Shu *et al. Phys. Rev. B* **76** (2007) 184115.

[86] F. C. Chou, M. W. Chu, G. J. Shu, F.-T. Huang, W. W. Pai, H. S. Sheu, and P. A. Lee *Phys. Rev. Lett.* **101** (Sep, 2008) 127404.

[87] Y. S. Meng, A. Van der Ven, M. K. Y. Chan, and G. Ceder *Phys. Rev. B* **72** (Nov, 2005) 172103.

[88] D. Qian *et al. Phys. Rev. Lett.* **97** (2006) 186405.

[89] Y. Y. Hinuma *et al. Phys. Rev. B* **77** (2008) 224111.

[90] T. S. Herng, D.-C. Qi, T. Berlijn, J. B. Yi, K. S. Yang, Y. Dai, Y. P. Feng, I. Santoso, C. Sanchez-Hanke, X. Gao, A. T. S. Wee, W. Ku, J. Ding, and A. Rusydi *Phys. Rev. Lett.* **105** (2010) 207201.

[91] S. Datta and B. Das *Appl. Phys. Lett.* **56** (1990) 665.

[92] H. Ohno, A. Shen, F. Matsukura, A. Oiwa, A. Endo, S. Katsumoto, and Y. Iye *Appl. Phys. Lett.* **69** (1996) 363.

[93] T. Dietl, H. Ohno, F. Matsukura, J. Cibert, and D. Ferrand *Science* **287** (2000) 1019.

[94] S. Chambers *Nat. Mat.* **9** (2010) 956.

[95] M. V. J. M. D. Coey and C. B. Fitzgerald *Nat. Mater.* **4** (2005) 173.

[96] See supplementary material at http://link.aps.org/ supplemental/10.1103/PhysRevLett.105.207201 for details of sample preparation, material characterizations, and theoretical calculations.

[97] B.-C. Shih, Y. Xue, P. Zhang, M. L. Cohen, and S. G. Louie *Phys. Rev. Lett.* **105** (2010) 146401.

[98] C. Friedrich, M. C. Mueller, and S. Bluegel *Phys. Rev. B* **83** (2011) 081101(R).

[99] S. Lany and A. Zunger *Phys. Rev. Lett.* **98** (2007) 045501.

[100] P. Agoston, K. Albe, R. M. Nieminen, and M. J. Puska *Phys. Rev. Lett.* **103** (2009) 245501.

[101] S. Lany and A. Zunger *Phys. Rev. Lett.* **106** (2011) 069601.

[102] P. Agoston, K. Albe, R. M. Nieminen, and M. J. Puska *Phys. Rev. Lett.* **106** (2011) 069602.

[103] V. I. Anisimov, I. V. Solovyev, M. A. Korotin, M. T. Czyzyk, and G. A. Sawatzky *Phys. Rev. B* **48** (1993) 16929.

[104] U. Ozgur *et al. J. Appl. Phys.* **98** (2005) 041301.

[105] K.-W. Yeh *et al. Eurohys. Lett.* **84** (2008) 37002.

[106] S. Jiang *et al. J. Phys. Condens. Matter* **21** (2009) 382203.

[107] S. Sharma *et al. Phys. Rev. B* **81** (2010) 174512.

[108] H. Wadati, I. Elfimov, and G. A. Sawatzky *Phys. Rev. Lett.* **105** (2010) 157004.

[109] K. Nakamura, R. Arita, and H. Ikeda *Phys. Rev. B* **83** (2011) 144512.

[110] M. Neupane *et al.* *Phys. Rev. B* **83** (2011) 094522.

[111] A. Olariu *et al.* *Phys. Rev. B* **83** (2011) 054518.

[112] W. Maleab *et al.* *J. Phys. Soc. Jpn.* **78** (2009) 123706.

[113] The DFT calculations were performed with the WIEN2K [30] implementation of the full potential linearized augmented plane wave method in the Perdew-Burke-Ernzerhof generalized gradient approximation. The k-point meshes were chosen to be 10-10-10 for the normal cell and 6-6-4 for the supercell. The basis size was determined by RKmax=7. The space group I4/mmm and the values of the lattice parameters a=b=3.9625Åand c=13.0168Åand the As height z=0.3545, were taken from [62].

Appendix A

Notation

We reserve lower case symbols for the normal cell quantities and upper case symbols for the supercell quantities.

Quantity	normal cell	supercell
primitive vector	a_1, a_2, a_3	A_1, A_2, A_3
lattice vector	r	R
primitive reciprocal vectors	b_1, b_2, b_3	B_1, B_2, B_3
reciprocal vectors	g	G
crystal momentum	k	K
band index	j	J
band	ε_{kj}	ε_{KJ}
Bloch state	$|kj\rangle$	$|KJ\rangle$
lattice vector	r	R
Wannier orbital index	n	N
Wannier state	$|rn\rangle$	$|RN\rangle$
k-state	$|kn\rangle$	$|KN\rangle$
impurity index	m	M
number of cells	l	L
volume of cell	v	V

Table A.1: Notation

Appendix B

The Map

The quantities of the normal cell and supercell are related to each other by a prescription to what we shall refer to as "the map". The map is the fundamental building block of the developed methodology presented in this thesis.

B.1 Definition

The map consist of 2 components:

1. An integer matrix M which expresses the super cell primitive vectors A_i in terms of the normal cell primitive vectors a_i:

$$\vec{A}_i = \sum_j M_{ij} \vec{a}_j \tag{B.1}$$

2. A list of super cell orbitals N belonging to the zeroth super cell $R = (0,0,0)$ and their corresponding normal cell lattice vectors r and normal cell orbitals n

Once the map is known each super cell lattice vector R and super cell orbital index N can be mapped to a normal cell vector r and normal cell orbital index n and vice versa:

$$R(r) , \ N(r,n) \leftrightarrow r(R,N) , \ n(N) \tag{B.2}$$

B.2   Examples

To get a better feeling for the map in figureB.1 we give some examples for a simple 2 dimensional square lattice with 2 orbitals per normal cell and a $\sqrt{2} \times \sqrt{2}$ super cell. Notice in this example that the orbitals do not need to lie within the cell.

$M =$	1	1
	-1	1

R	N	r	n
(0,0)	0	(0,0)	0
(0,0)	1	(0,0)	1
(0,0)	2	(1,0)	0
(0,0)	3	(1,0)	1

Example:
R=(1,1) N=3 $\leftrightarrow$ r=(3,1) n=1
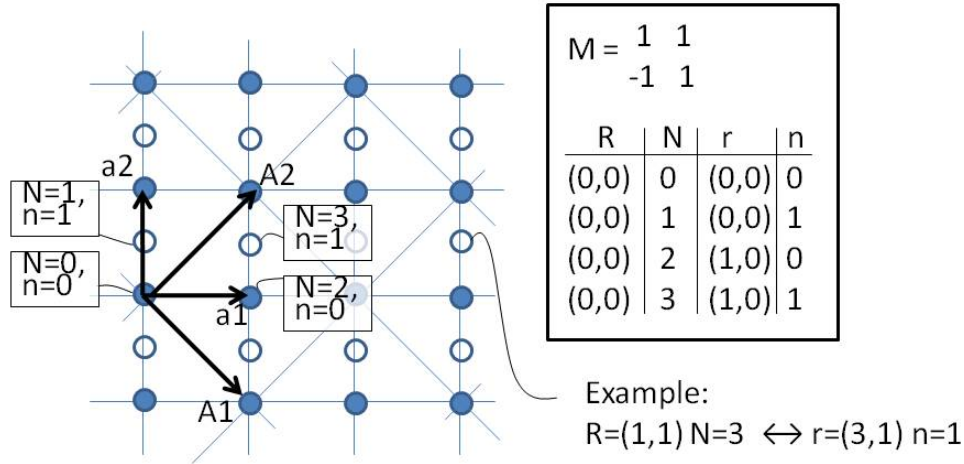
Figure B.1:   Example of a map without substitutions or vacancies.

In figures B.2 and B.3 we illustrate examples of substitutions and vacancies. The substitution in B.2 can equivalently be regarded as 2 vacancies with respect to a normal cell lattice with 3 orbitals per normal cell. The vacancy in B.3 can equivalently be regarded as an interstitial with respect to a normal cell lattice with 1 orbital per normal cell.
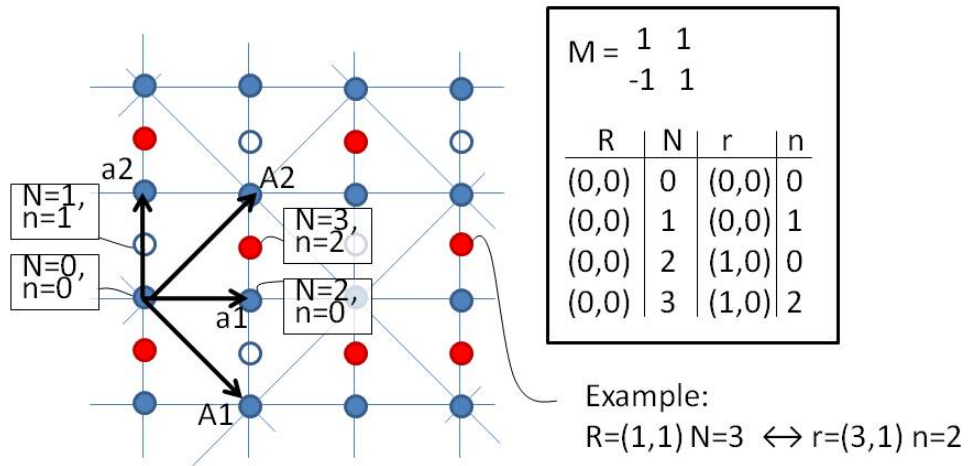
Figure B.2: Example of a map with substitution.
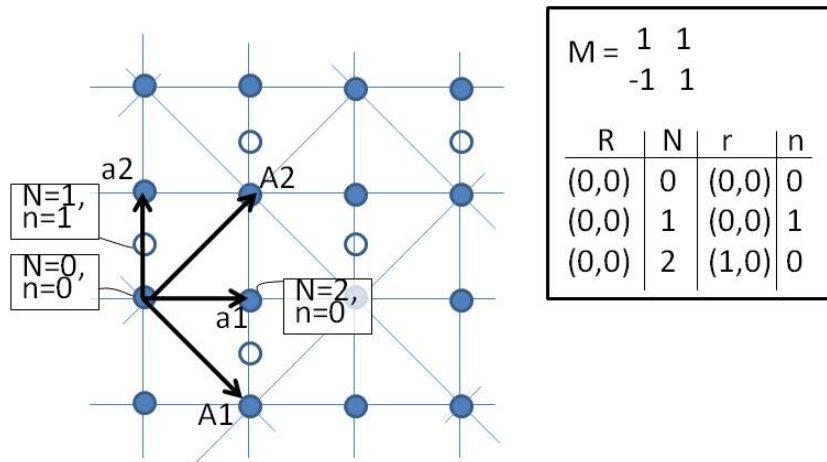
Figure B.3: Example of a map with vacancy.

Appendix C

Reciprocal States
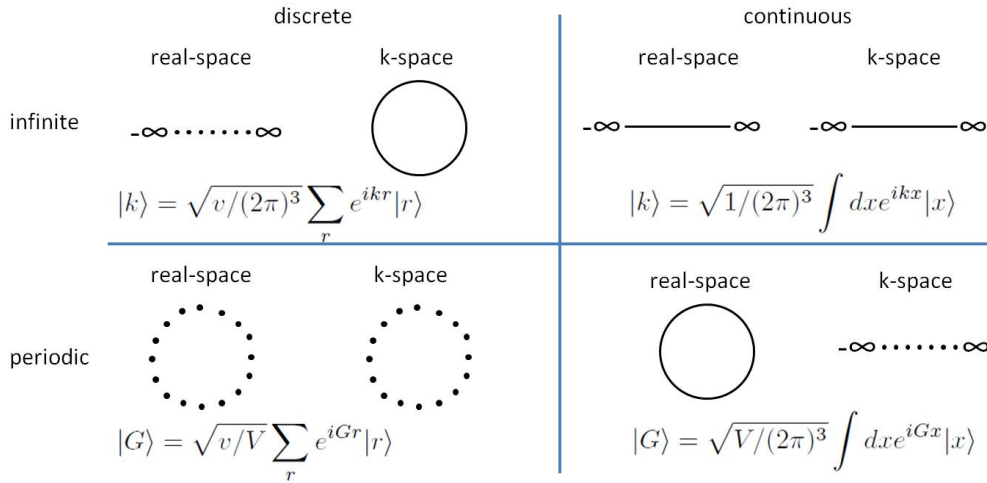
Figure C.1: Four different Hilbert spaces together with their reciprocal spaces.

C.1 Orthonormality and Completeness

For each of the four Hilbert spaces, we need to check the orthonormality and completeness of the reciprocal states. These properties follow directly from the mathematical identities in the next subsection. Lets check the orthonormality and completeness for the states in the "infinite discrete" Hilbert space, which for example could be Wannier states $|rn\rangle$ or phonons. From (C.15) we find

the orthonormality of the reciprocal states:

$$\langle k'|k\rangle = v/(2\pi)^3 \sum_{r'} e^{-ik'r'}\langle r'| \sum_{r} e^{ikr}|r\rangle = v/(2\pi)^3 \sum_{r} e^{ir(k-k')} = \delta(k - k') \quad (C.1)$$

To check the completeness we use (C.6):

$$1 = \int dk|k\rangle\langle k| \Leftrightarrow \delta_{r,r'} = \int dk\langle r|k\rangle\langle k|r'\rangle = v/(2\pi)^3 \int dk e^{ik(r-r')} \quad (C.2)$$

The orthornormality and completeness for the three other Hilbert spaces "infinite continuous", "periodic discrete" and "periodic continuous" can be checked from the rest of the identities.

C.2 Mathematical Identities

claim 9

$$\int_{\text{supercell}} d^3x e^{iGx} = V\delta_{G,0} \; ; \; G \in \text{super reciprocal lattice} \quad (C.3)$$

proof 9 *The integrand e^{iGx} satisfies periodic boundary conditions at the supercell. Because of this the translation $x \to x' + \epsilon$ will merely reorder the integral without changing its value.[1] Therefore we find*

$$\int_{\text{supercell}} d^3x e^{iGx} = e^{iG\epsilon} \int_{\text{supercell}} d^3x' e^{iGx'} \Leftrightarrow e^{iG\epsilon} = 1 \text{ or } \int_{\text{supercell}} d^3x e^{iGx} = 0 \quad (C.5)$$

Since $e^{iG\epsilon} = 1 \Leftrightarrow G = 0$ and $\int_{\text{supercell}} d^3x = V$ this completes the proof.

claim 10

$$\int_{\text{normal brillouin zone}} d^3k e^{irk} = (2\pi)^3/v\delta_{r,0} \quad (C.6)$$

---

[1]To make this a bit more explicit we follow the integration along one of the directions

$$
\begin{aligned}
\int_{\epsilon}^{A+\epsilon} dx' e^{iGx'} &= \int_{\epsilon}^{A} dx' e^{iGx'} + \int_{A}^{A+\epsilon} dx' e^{iGx'} = \int_{\epsilon}^{A} dx' e^{iGx'} + \int_{0}^{\epsilon} dx'' e^{iG(x''-A)} \\
&= \int_{\epsilon}^{A} dx' e^{iGx'} + \int_{0}^{\epsilon} dx'' e^{iGx''} = \int_{0}^{A} dx' e^{iGx'} \quad (C.4)
\end{aligned}
$$

where we used $G \cdot A = 2\pi n$

proof 10 *See proof 9*

claim 11

$$\sum_{r\in\text{supercell}} e^{irG} = (V/v) \sum_{g\in\text{normal reciprocal}} \delta_{G,g} \qquad (C.7)$$

proof 11 *Similar as in proof 9 the shift $r \to r' + a$ will merely reorder the sum without changing its value.*

$$\sum_{r\in\text{supercell}} e^{irG} = e^{iGa} \sum_{r'\in\text{supercell}} e^{ir'G} \Leftrightarrow e^{iGa} = 1 \text{ or } \sum_{r\in\text{supercell}} e^{irG} = 0 \quad (C.8)$$

Since $e^{iGa} = 1 \Leftrightarrow G \in$normal reciprocal lattice and $\sum_{r\in\text{supercell}} = V/v$ this completes the proof.

claim 12

$$\sum_{G\in\text{normal brillouin zone}} e^{irG} = (V/v) \sum_{R\in\text{super lattice}} \delta_{R,r} \qquad (C.9)$$

proof 12 *See proof 11*

claim 13

$$\int_{-\infty}^{+\infty} d^3x e^{ikx} = (2\pi)^3 \delta(k) \qquad (C.10)$$

proof 13 *We use (C.3) to find:*

$$\sum_{G} f(G) \left(\int_{\text{supercell}} d^3x e^{iGx} \right) = Vf(0) \qquad (C.11)$$

next we simply multiply both sides with the finite volume element $(2\pi)^3/V$

$$(2\pi)^3/V \sum_{G} f(G) \left(\int_{\text{supercell}} d^3x e^{iGx} \right) = (2\pi)^3 f(0) \qquad (C.12)$$

Then we take the infinite supercell limit, i.e. continuum k-space limit $(2\pi)^3/V \sum_{G}(...) \to$

$\int d^3k(...)$

$$\int d^3k f(k) \left(\int_{-\infty}^{+\infty} d^3x e^{ikx} \right) = (2\pi)^3 f(0) \tag{C.13}$$

which completes the proof

claim 14

$$\int_{-\infty}^{+\infty} d^3k e^{ikx} = (2\pi)^3 \delta(x) \tag{C.14}$$

proof 14 *See proof 13*

claim 15

$$\sum_{r \in \text{normal lattice}} e^{ikr} = (2\pi)^3/v \sum_{g \in \text{normal reciprocal}} \delta(k+g) \tag{C.15}$$

proof 15 *See proof 13*

claim 16

$$\sum_{G \in \text{super reciprocal}} e^{iGx} = (1/v) \sum_{R \in \text{super lattice}} \delta(x+R) \tag{C.16}$$

proof 16 *See proof 13*

Appendix D

Toy Example Unfolding

D.1 Hamiltionan on Normal Cell k-basis

Consider the 1 dimensional 1 band tight binding Hamiltonian with nearest neighbor hopping only:

$$\langle r|H^0|r\rangle = \epsilon \; ; \; \langle r+a|H^0|r\rangle = \langle r|H^0|r+a\rangle = -t \; ; \; t > 0 \tag{D.1}$$

By transforming to the normal cell k-basis, the system is diagonalized:

$$\langle k|H^0|k'\rangle =$$
$$= \left(\sqrt{a/2\pi}\sum_r e^{-ikr}\langle r|\right) H^0 \left(\sqrt{a/2\pi}\sum_{r'} e^{ik'r'}|r'\rangle\right)$$
$$= \left(\sqrt{a/2\pi}\sum_r e^{-ikr}\langle r|\right) H^0 \left(\sqrt{a/2\pi}e^{ik'(r-a)}|r-a\rangle + e^{ik'(r)}|r\rangle + e^{ik'(r+a)}|r+a\rangle\right)$$
$$= (a/2\pi)\sum_r e^{-i(k-k')r}(\epsilon + e^{-ik'a}t + e^{i'k'a}t) = \delta(k-k')(\epsilon + 2t\cos ka) \tag{D.2}$$

D.2 Impurity Hamiltionan on Supercell K-basis

Now we rewrite the problem on supercell basis (two normal cells per supercell). The tight binding model in this basis becomes

$$\langle RN{=}0|\mathrm{H}^0|RN{=}0\rangle = \langle RN{=}1|\mathrm{H}^0|RN{=}1\rangle = \epsilon$$
$$\langle R-A, N{=}1|\mathrm{H}^0|RN{=}0\rangle = \langle RN{=}0|\mathrm{H}^0|RN{=}1\rangle = -\mathrm{t} \tag{D.3}$$

Furthermore we introduce the impurity potential:

$$\langle RN{=}0|\Delta|RN{=}0\rangle = -\Delta \ ; \ \langle RN{=}1|\Delta|RN{=}1\rangle = \Delta \qquad (D.4)$$

Representing the total on the super cell K-basis block diagonalizes the system:

$$
\begin{aligned}
&< KN{=}0|H^0 + \Delta|K'N'{=}0 > \\
&= \left(\sqrt{A/2\pi}\sum_R e^{-iKR}\langle RN{=}0|\right) H^0 + \Delta \left(\sqrt{A/2\pi}\sum_{R'} e^{iK'R'}|R'N'{=}0\rangle\right) \\
&= \left(\sqrt{A/2\pi}\sum_R e^{-iKR}\langle RN{=}0|\right) H^0 + \Delta \left(\sqrt{A/2\pi}e^{iK'R}|RN{=}0\rangle\right) \\
&= (A/2\pi)\sum_R e^{-i(K-K')R}\left(\epsilon - \Delta\right) = \delta(K - K')\left(\epsilon - \Delta\right) \qquad (D.5)
\end{aligned}
$$

similarly

$$\langle KN{=}1|H^0 + \Delta|K'N'{=}1\rangle = \delta(K - K')\left(\epsilon + \Delta\right) \qquad (D.6)$$

For the off-diagonal terms we find

$$
\begin{aligned}
&\langle KN{=}0|H^0|K'N'{=}1\rangle \\
&= \left(\sqrt{A/2\pi}\sum_R e^{-iKR}\langle RN{=}0|\right) H^0 \left(\sqrt{A/2\pi}\sum_{R'} e^{iK'R'}|R'N'{=}1\rangle\right) \\
&= \left(\sqrt{A/2\pi}\sum_R e^{-iKR}\langle RN{=}0|\right) H^0 \left(\sqrt{A/2\pi}(e^{iK'R}|R,1\rangle + e^{iK'(R-A)}|R - A, 1\rangle)\right) \\
&= -(A/2\pi)\sum_R e^{-i(K-K')R}t(1 + e^{-iKA}) \\
&= -\delta(K - K')(1 + e^{-iKA}) = -\delta(K - K')2t\cos(Ka)e^{-iKa}
\end{aligned}
$$

$$(D.7)$$

where in the last step we used $1 + e^{i2x} = 2\cos x e^{ix}$. Similarly we have

$$\langle KN{=}1|H|K'N'{=}0\rangle = -\delta(K - K')2t\cos(Ka)e^{iKa} \qquad (D.8)$$

103

So we have the following block-diagonalized form

$$\langle KN|H^0 + \Delta|K'N'\rangle = \delta(K - K') \begin{pmatrix} \epsilon - \Delta & -2t\cos(Ka)e^{-iKa} \\ -2t\cos(Ka)e^{iKa} & \epsilon + \Delta \end{pmatrix} \text{(D.9)}$$

Using (D.17) we find:

$$\varepsilon_{KJ=0,1} = \epsilon \mp \sqrt{\Delta^2 + 4t^2\cos^2(Ka)} \tag{D.10}$$

and from (D.18) we find:

$$\langle KN|KJ{=}0,1\rangle = \sqrt{1/2}\begin{pmatrix} \sqrt{1 \pm \Delta/\sqrt{\Delta^2 + 4t^2\cos^2(Ka)}} \\ \pm e^{iKa}\sqrt{1 \mp \Delta/\sqrt{\Delta^2 + 4t^2\cos^2(Ka)}} \end{pmatrix} \tag{D.11}$$

where the compononents of the eigenvectors correspond to the supercell orbitals $N = 0$ and $N = 1$, which are located at $r(N{=}0) = 0$ and $r(N{=}1) = $ a within the supercell. Now we use the unfolding formula (3.6) to find

$$\begin{aligned}
|\langle k{=}K|KJ{=}0\rangle|^2 &= \left|\frac{1}{2}\sum_N e^{-iKr(N)}\langle KN|KJ{=}0\rangle\right|^2 \\
&= \frac{1}{4}\left|\sqrt{1 + \Delta/\sqrt{\Delta^2 + 4t^2\cos^2(Ka)}} + \sqrt{1 - \Delta/\sqrt{\Delta^2 + 4t^2\cos^2(Ka)}}\right|^2 \\
&= \frac{1}{2}\left(1 + \sqrt{1 - \Delta^2/(\Delta^2 + 4t^2\cos^2(Ka))}\right) = \frac{1}{2}\left(1 + \sqrt{4t^2\cos^2(Ka)/(\Delta^2 + 4t^2\cos^2(Ka))}\right)
\end{aligned}$$
$$\tag{D.12}$$

and

$$\begin{aligned}
|\langle k{=}K \pm \underbrace{G}_{\pi/a}|KJ{=}0\rangle|^2 &= \left|\frac{1}{2}\sum_N e^{-i(K+\pi/a)r(N)}\langle KN|KJ{=}0\rangle\right|^2 \\
&= \frac{1}{4}\left|\sqrt{1 + \Delta/\sqrt{\Delta^2 + 4t^2\cos^2(Ka)}} - \sqrt{1 - \Delta/\sqrt{\Delta^2 + 4t^2\cos^2(Ka)}}\right|^2 \\
&= \frac{1}{2}\left(1 - \sqrt{4t^2\cos^2(Ka)/(\Delta^2 + 4t^2\cos^2(Ka))}\right)
\end{aligned}$$
$$\tag{D.13}$$

Combining (D.12) and (D.13) we find

$$|\langle k|KJ{=}0\rangle|^2 = \left(1/2 + \mathrm{t}\cos(\mathrm{ka})/\sqrt{\Delta^2 + 4\mathrm{t}^2\cos^2(\mathrm{ka})}\right) \qquad (D.14)$$

Similarly we can find

$$|\langle k|KJ{=}1\rangle|^2 = \left(1/2 - \mathrm{t}\cos(\mathrm{ka})/\sqrt{\Delta^2 + 4\mathrm{t}^2\cos^2(\mathrm{ka})}\right) \qquad (D.15)$$

In figure D.1 and D.2 the spectral weight and the spectral function are plotted for different values of t and Δ.
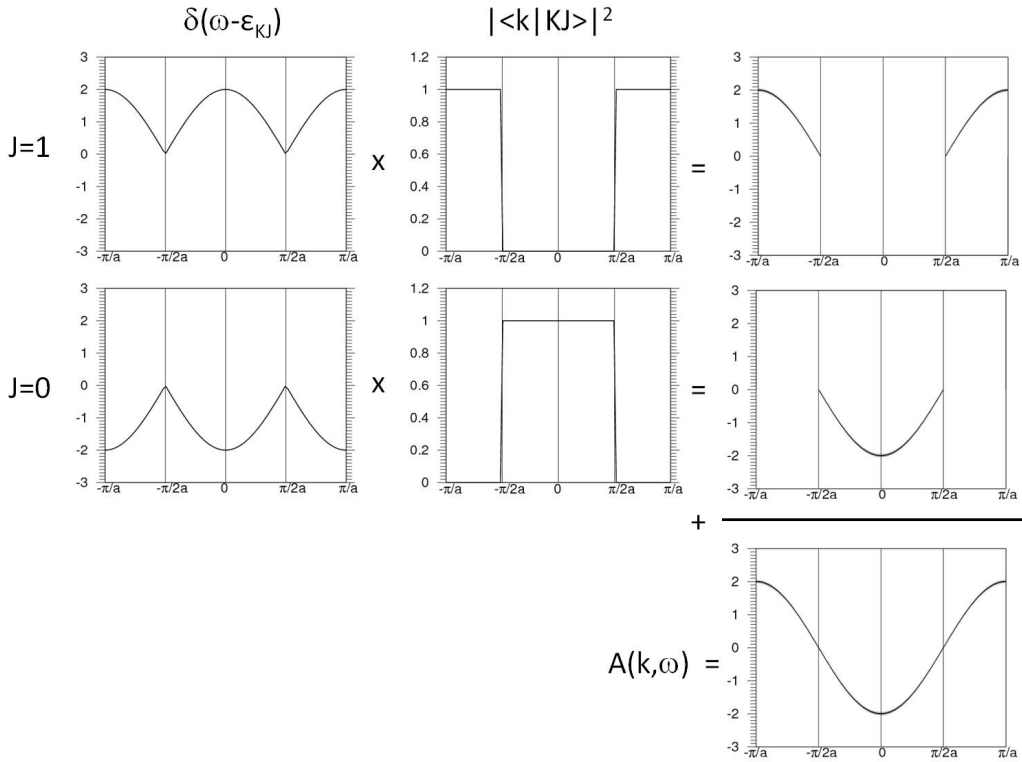

Figure D.1: Spectral function for $t = 1$ and $\Delta = 0$.
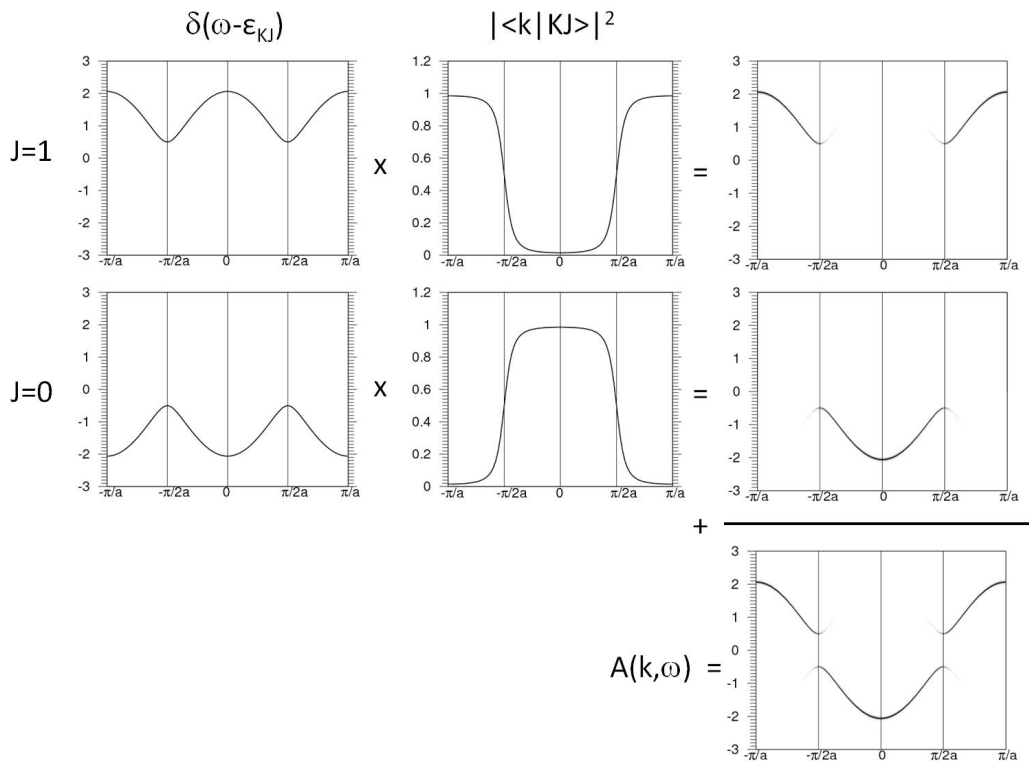
Figure D.2: Spectral function for $t = 1$ and $\Delta = 0.5$.

106

D.3   Ever Diagonalized a 2 by 2 Matrix?

claim 17 *Given the matrix*

$$\begin{pmatrix} A - B & \pm C e^{i\alpha} \\ \pm C e^{-i\alpha} & A + B \end{pmatrix} \tag{D.16}$$

where A, B and C are real and positive and $\alpha \in [0, 2\pi)$, the eigenvalues are given by

$$\lambda_1 = A - \sqrt{B^2 + C^2} \; ; \; \lambda_2 = A + \sqrt{B^2 + C^2} \tag{D.17}$$

and the eigenvectors (up to an overall phase) are given by

$$\vec{\lambda_1} = \frac{1}{\sqrt{2}} \begin{pmatrix} \mp e^{i\alpha} \sqrt{1 + B/\sqrt{B^2 + C^2}} \\ \sqrt{1 - B/\sqrt{B^2 + C^2}} \end{pmatrix} \; ; \; \vec{\lambda_2} = \frac{1}{\sqrt{2}} \begin{pmatrix} \pm \sqrt{1 - B/\sqrt{B^2 + C^2}} \\ e^{-i\alpha} \sqrt{1 + B/\sqrt{B^2 + C^2}} \end{pmatrix} \tag{D.18}$$

proof 17 *Solving for the eigenvalues*

$$0 = \begin{vmatrix} A - B - \lambda & \pm C e^{-i\alpha} \\ \pm C e^{i\alpha} & A + B - \lambda \end{vmatrix} = (A - \lambda)^2 - B^2 - C^2$$

$$\Rightarrow \quad (A - \lambda) = \pm \sqrt{B^2 + C^2}$$

$$\Rightarrow \quad \lambda_1 = A - \sqrt{B^2 + C^2} \; ; \; \lambda_2 = A + \sqrt{B^2 + C^2} \tag{D.19}$$

Solving for the eigenvector with eigenvalue λ_1

$$(\pm C e^{-i\alpha}) \langle 1 | \lambda_1 \rangle + (A + B - \lambda_1) \langle 2 | \lambda_1 \rangle = 0$$

$$\Rightarrow \quad \langle 1 | \lambda_1 \rangle = \mp \langle 2 | \lambda_1 \rangle \frac{A + B - \lambda_1}{C e^{-i\alpha}} = \mp \langle 2 | \lambda_1 \rangle \frac{B + \sqrt{B^2 + C^2}}{C e^{-i\alpha}}$$

$$\Rightarrow \quad \vec{\lambda_1} = \begin{pmatrix} \langle 1 | \lambda_1 \rangle \\ \langle 2 | \lambda_1 \rangle \end{pmatrix} \propto \begin{pmatrix} \mp e^{i\alpha} (B + \sqrt{B^2 + C^2})/C \\ 1 \end{pmatrix} \tag{D.20}$$

normalizing

$$\vec{\lambda_1} = \begin{pmatrix} \dfrac{\mp e^{i\alpha}(B+\sqrt{B^2+C^2})/C}{\sqrt{1+(B+\sqrt{B^2+C^2})^2/C^2}} \\[2ex] \dfrac{1}{\sqrt{1+(B+\sqrt{B^2+C^2})^2/C^2}} \end{pmatrix} \tag{D.21}$$

Now lets simplify first the second coefficient of this vector:

$$\langle 2|\lambda_1\rangle^{-2}\left(1 - B/\sqrt{B^2+C^2}\right)$$

$$= \left(1 + (B+\sqrt{B^2+C^2})^2/C^2\right)\left(1 - B/\sqrt{B^2+C^2}\right)$$

$$= \left(C^2\sqrt{B^2+C^2}\right)^{-1}\left(C^2 + (B+\sqrt{B^2+C^2})^2\right)\left(\sqrt{B^2+C^2} - B\right)$$

$$= \left(C^2\sqrt{D^2+C^2}\right)^{-1}\left(2(C^2+B^2) + 2B\sqrt{B^2+C^2}\right)\left(\sqrt{B^2+C^2} - B\right)$$

$$= 2\left(C^2\right)^{-1}\left(\sqrt{B^2+C^2} + B\right)\left(\sqrt{B^2+C^2} - D\right)$$

$$= 2\left(C^2\right)^{-1}\left((B^2+C^2) - B^2\right) = 2$$

$$\Rightarrow \langle 2|\lambda_1\rangle = \frac{1}{\sqrt{2}}\sqrt{1 - B/\sqrt{B^2+C^2}} \tag{D.22}$$

Now the absolute value of the first coefficient follows:

$$|\langle 1|\lambda_1\rangle| = \sqrt{1 - \langle 2|\lambda_1\rangle^2}$$

$$= \sqrt{1 - \frac{1}{2}(1 - B/\sqrt{B^2+C^2})}$$

$$= \frac{1}{\sqrt{2}}\sqrt{1 + B/\sqrt{B^2+C^2}} \tag{D.23}$$

The second eigenvector follows from orthonormality.

Appendix E

Toy Model Example Partitioning

Lets work out the partitioning by hand for a simple toy model with some arbitrary numerical values. For the undoped Hamiltonian H^0 we take a square lattice, with lattice constant a, with one Wannier orbital per site, with an onsite energy of 2eV, a real nearest neighbor hopping of 1eV and a real second nearest neighbor hopping of 0.5eV. In addition we consider a $\sqrt{2} \times \sqrt{2}$ superlattice of impurities, the influence of which we model with some more arbitrary numbers. We raise the onsite energies of the impurity sites from 2eV to 2.1eV and we lower the rest of the onsite energies from 2eV to 1.9eV. We lower the nearest neighbor hopping from 1eV to 0.9eV. The second nearest neighbor hopping from impurity to impurity site we lower from 0.5eV to 0.4eV and the second nearest neighbor hopping from non-impurity to non-impurity site we raise from 0.5eV to 0.6eV.

All the hopping elements of the undoped/single-impurity model are summarized in the blocks on left/right side of figure E.1. Each block corresponds to a pair of lattice vectors, which is specified above the block. Only those hopping elements are listed that hop from the zeroth unit cell, all the other hopping elements follow from the translational symmetry. The row and column index corresponds to the "from" and "to" Wannier orbital indices respectively.

Having the undoped and single impurity Hamiltonians, the impurity influence can be calculated. If we choose the partitioning radius to be two lattice constants $2a$, then the particular form of the interpolation function is irrele-

H^0 (undoped)

-1 1   0 1   1 1
-1 0   0 0   1 0
-1 -1   0 -1   1 -1

map

$M = \begin{matrix} 1 & 1 \\ -1 & 1 \end{matrix}$

R	N	r	n
(0,0)	0	(0,0)	0
(0,0)	1	(1,0)	0

H^1 (single impurity)

-1 0   0 1
-1 -1   0 0   1 1
0 -1   1 0

(0 0) (0 0)
| 2 |

(-1 0) (0 0)
| 1 |

(0 -1) (0 0)
| 1 |

(1 0) (0 0)
| 1 |

(0 1) (0 0)
| 1 |

(-1 -1) (0 0)
| 0.5 |

(1 -1) (0 0)
| 0.5 |

(-1 1) (0 0)
| 0.5 |

(1 1) (0 0)
| 0.5 |

(-1 -1) (0 0)
| | |
| 0.9 | |

(-1 0) (0 0)
| 0.4 | |
| 0.9 | 0.6 |

(0 -1) (0 0)
| 0.4 | |
| 0.9 | 0.6 |

(0 1) (0 0)
| 0.4 | 0.9 |
| | 0.6 |

(1 0) (0 0)
| 0.4 | 0.9 |
| | 0.6 |

(1 1) (0 0)
| | 0.9 |
| | |

(0 0) (0 0)
| 2.1 | 0.9 |
| 0.9 | 1.9 |

<r'=(-1,1) n'=0| H^0|r=(0,0) n=0> = 0.5eV
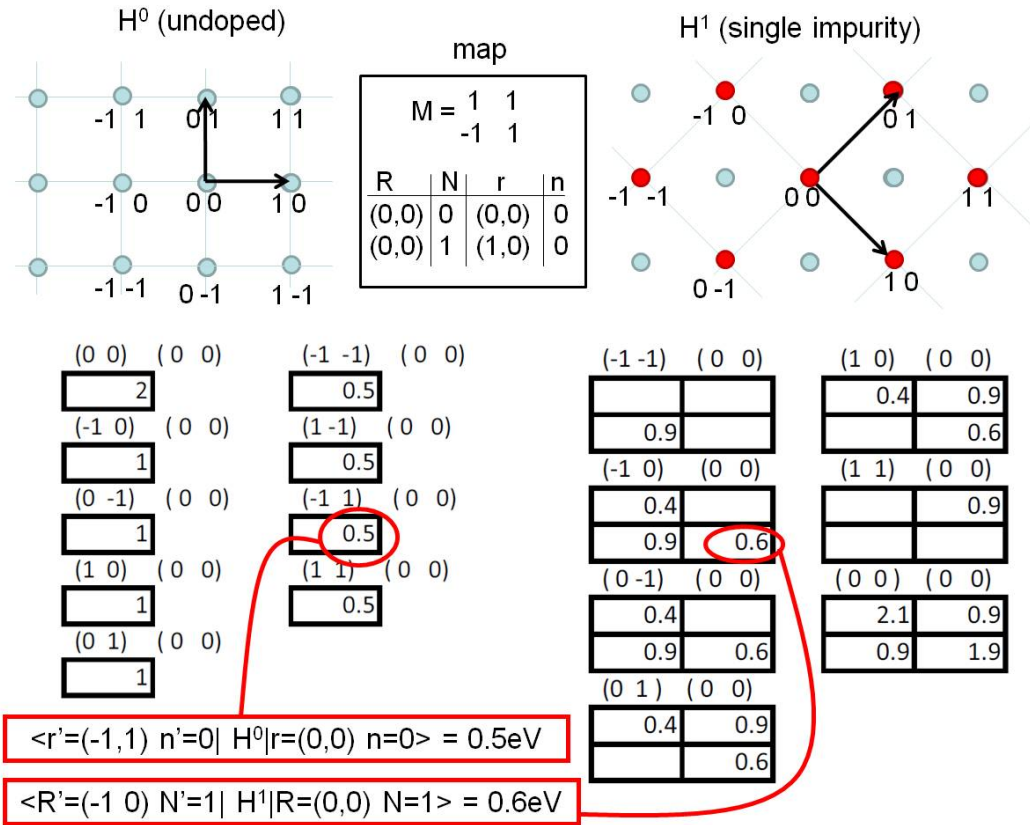
<R'=(-1 0) N'=1| H^1|R=(0,0) N=1> = 0.6eV

Figure E.1: Tight binding Hamiltonians of the undoped and single impurity toy models. The hopping elements of the undoped/single-impurity toy models are summarized by the blocks on the left/right.

110

H¹-H⁰ = +0.1eV

$H^1\text{-}H^0 = +0.1\text{eV}$
NN distance = 0
NNN distance = 2√2a
weight = 1
Δ = +0.1eV

0 1

$H^1\text{-}H^0 = -0.1\text{eV}$
NN distance = 2a
NNN distance = 2√5a
weight = 0.25
Δ = -0.025eV

$H^1\text{-}H^0 = -0.1\text{eV}$
NN distance = a
NNN distance = (1+√2)a
weight = 1
Δ = -0.025eV

0 1

$H^1\text{-}H^0 = -0.1\text{eV}$
NN distance = √2a
NNN distance = (2+√2)a
weight = 0.5
Δ = -0.05eV

0 1

$H^1\text{-}H^0 = +0.1\text{eV}$
NN distance = 2a
NNN distance = (1+√5)a
weight = 0.5
Δ = +0.05eV

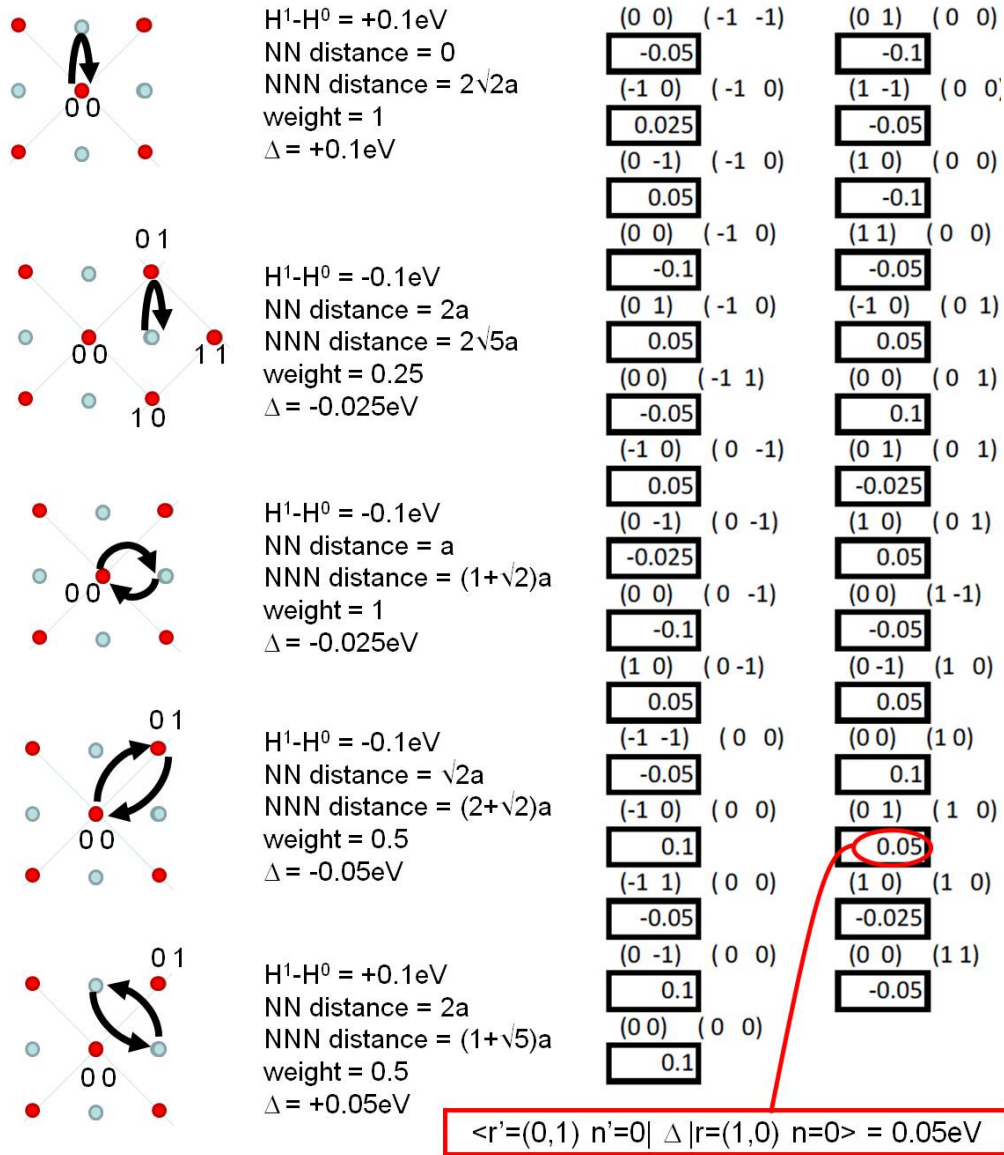| (0 0) (-1 -1)	(0 1) (0 0)
-0.05	-0.1
(-1 0) (-1 0)	(1 -1) (0 0)
0.025	-0.05
(0 -1) (-1 0)	(1 0) (0 0)
0.05	-0.1
(0 0) (-1 0)	(1 1) (0 0)
-0.1	-0.05
(0 1) (-1 0)	(-1 0) (0 1)
0.05	0.05
(0 0) (-1 1)	(0 0) (0 1)
-0.05	0.1
(-1 0) (0 -1)	(0 1) (0 1)
0.05	-0.025
(0 -1) (0 -1)	(1 0) (0 1)
-0.025	0.05
(0 0) (0 -1)	(0 0) (1 -1)
-0.1	-0.05
(1 0) (0 -1)	(0 -1) (1 0)
0.05	0.05
(-1 -1) (0 0)	(0 0) (1 0)
-0.05	0.1
(-1 0) (0 0)	(0 1) (1 0)
0.1	0.05
(-1 1) (0 0)	(1 0) (1 0)
-0.05	-0.025
(0 -1) (0 0)	(0 0) (1 1)
0.1	-0.05
(0 0) (0 0)	
0.1	

<r'=(0,1) n'=0| Δ |r=(1,0) n=0> = 0.05eV

Figure E.2: Tight binding Hamiltonian of the impurity influence, obtained from partitioning the difference of the undoped and single-impurity Hamiltonian. The impurity influence tight binding elements are summarized by the blocks on the right. The five different partitioning scenarios are illustrated on the left.

vant for the case of the square lattice as we shall see. The resulting impurity influence is summarized in figure E.2. The impurity influence tight binding elements are summarized by the blocks on the right. The five different partitioning scenarios are illustrated on the left.

Lets work out one of the elements by hand, namely the influence of the impurity on the nearest neighbor to nearest neighbor hopping from Wannier state $|r'{=}(1,0)\ n'{=}0\rangle$ to Wannier state $\langle r''{=}(0,1)\ n''{=}0|$. The partitioning scenario for this hopping element is depicted in the lowest of the five cartoons. First of all lets work out the partitioning weights. For this hopping element, the nearest impurities are located at supercell lattice vectors $R = (0,0)$ and $R = (1,0)$. Both the "from" Wannier state $|r'{=}(1,0)\ n'{=}0\rangle$ and the "to" Wannier state $\langle r''{=}(0,1)\ n''{=}0|$ are at a distance of one lattice constant a from the impurities. Therefore the distance of the hopping element according to formula 3.15 will be two lattice constants. The next nearest impurity is for example located at $R = (1,1)$. The "from" Wannier state $|r'{=}(1,0)\ n'{=}0\rangle$ is at a distance a from the impurity at $R = (1,1)$, but the "to" Wannier state $\langle r''{=}(0,1)\ n''{=}0|$ is at a distance of $\sqrt{5}a$ from the impurity at $R = (1,1)$. Therefore the distance of the hopping element to the impurity at $R = (1,1)$ is $(1+\sqrt{5})a$ which is beyond the partitioning radius $2a$. So for the particular hopping element we only need to consider the nearest neighbors. The same is true for all the other four partitioning scenarios depicted in figure E.2. Since all the nearest neighbors are equally far away, the partitioning weights will be equal to the number of nearest neighbors. Now lets complete the calculation

of the partitioning of that particular hopping element:

$$\langle r''{=}(0,1)\ n''{=}0|\Delta^{r=(0,0)}|r'{=}(1,0)\ n'{=}0\rangle$$

$$= \Big(\langle r''{=}(0,1)\ n''{=}0|H^1|r'{=}(1,0)\ n'{=}0\rangle - \langle r''{=}(0,1)\ n''{=}0|H^0|r'{=}(1,0)\ n'{=}0\rangle\Big)$$

$$\times \frac{P^{r=(0,0)}\Big(r''{=}(0,1)\ n''{=}0, r'{=}(1,0)\ n'{=}0\Big)}{\sum_R P^{r=R}\Big(r''{=}(0,1)\ n''{=}0, r'{=}(1,0)\ n'{=}0\Big)}$$

$$= \Big(\langle R'{=}(-1,0)\ N'{=}1|H^1|R{=}(0,0)\ N=1\rangle - \langle r'{=}(-1,1)\ n'{=}0|H^0|r{=}(0,0)\ n{=}0\rangle\Big)$$

$$\times \frac{P^{r=(0,0)}\Big(r''{=}(0,1)\ n''{=}0, r'{=}(1,0)\ n'{=}0\Big)}{P^{r=(0,0)}\Big(r''{=}(0,1)\ n''{=}0, r'{=}(1,0)\ n'{=}0\Big) + P^{r=(0,1)}\Big(r''{=}(0,1)\ n''{=}0, r'{=}(1,0)\ n'{=}0\Big)}$$

$$= (0.6\text{eV} - 0.5\text{eV}) \times \frac{\text{f}(2a)}{\text{f}(2a) + \text{f}(2a)} = (0.1\text{eV}) \times 0.5 = 0.05\text{eV} \qquad (\text{E.1})$$

where the values in the last equation were taken from figure E.1. Note that the interpolation function f dropped out as promised.

Appendix F

Partitioning Independence

To simplify the following analysis we suppress the Wannier lattice and orbital indices and the impurity indices, since they play no role for the point we want to make. Furthermore without loss of generality we consider a test system with only one impurity located at the zeroth normal cell.

claim 18 *If the input superlattice SL_{in} is a subset of the test superlattice SL_{test} then the effective Hamiltonian H_{test} is independent of the partitioning function $p^{(r)}$.*

proof 18 *Given a test superlattice of impurities located at the zeroth normal cell of the test supercells:*

$$H_{test} = H^0 + \sum_{R_{test} \in SL_{test}} \Delta^{(R_{test})} \tag{F.1}$$

Obviously H^0 is independent of the partitioning so we only need to focus on the second term, the sum of impurity influences. First we will use the fact that the input superlattice SL_{in} is a subset of the test superlattice SL_{test}.

$$\sum_{R_{test} \in SL_{test}} \Delta^{(R_{test})} = \sum_{R_{test} \in SC_{in}} \sum_{R_{in} \in SL_{in}} \Delta^{(R_{test}+R_{in})} \tag{F.2}$$

where SC_{in} is the input supercell of test supercells. To complete the proof we plug in the definition of the impurity influence as a function of the normalized

partitioning function:

$$\Delta^{(r)} = \left(H^{(r)} - H^0\right) \frac{P^{(r)}}{\sum_{R_{in} \in SL_{in}} P^{(r+R_{in})}} \tag{F.3}$$

to find that the partitioning functions drops out:

$$\sum_{R_{test} \in SL_{test}} \Delta^{(R_{test})}$$

$$= \sum_{R_{test} \in SC_{in}} \sum_{R_{in} \in SL_{in}} \left(H^{(R_{test}+R_{in})} - H^0\right) \frac{P^{(R_{test}+R_{in})}}{\sum_{R'_{in} \in SL_{in}} P^{(R_{test}+R_{in}+R'_{in})}}$$

$$= \sum_{R_{test} \in SC_{in}} \left(H^{(R_{test})} - H^0\right) \frac{\sum_{R_{in} \in SL_{in}} P^{(R_{test}+R_{in})}}{\sum_{R'_{in} \in SL_{in}} P^{(R_{test}+R_{in}+R'_{in})}}$$

$$= \sum_{R_{test} \in SC_{in}} \left(H^{(R_{test})} - H^0\right) \tag{F.4}$$

where in the second equation we used the periodicity of the input superlattice $H^{(R_{test}+R_{in})} = H^{(R_{test})}$.

Appendix G

Additional Benchmarks of the Effective Hamiltonian against DFT for NaxCoO2

To explore the applicability and limitation of the effective Hamiltonian for the case of $Na_x CoO_2$, we present here, in addition to figure 4.5 more comparisons of spectral functions $A(k, \omega)$ calculated from the full DFT and the effective Hamiltonian (see figures G.1-G.4). The size of the deviations between the full DFT and the effective Hamiltonian should be compared with the size of the Na impurity induced changes. For this purpose the spectral function of the undoped $Co_2 O_4$ is also plotted as a reference for each benchmark. From these comparisons we see that the Na impurity induced changes on the spectral functions, are accurately reproduced by the effective Hamiltonian far into the high doping regime.
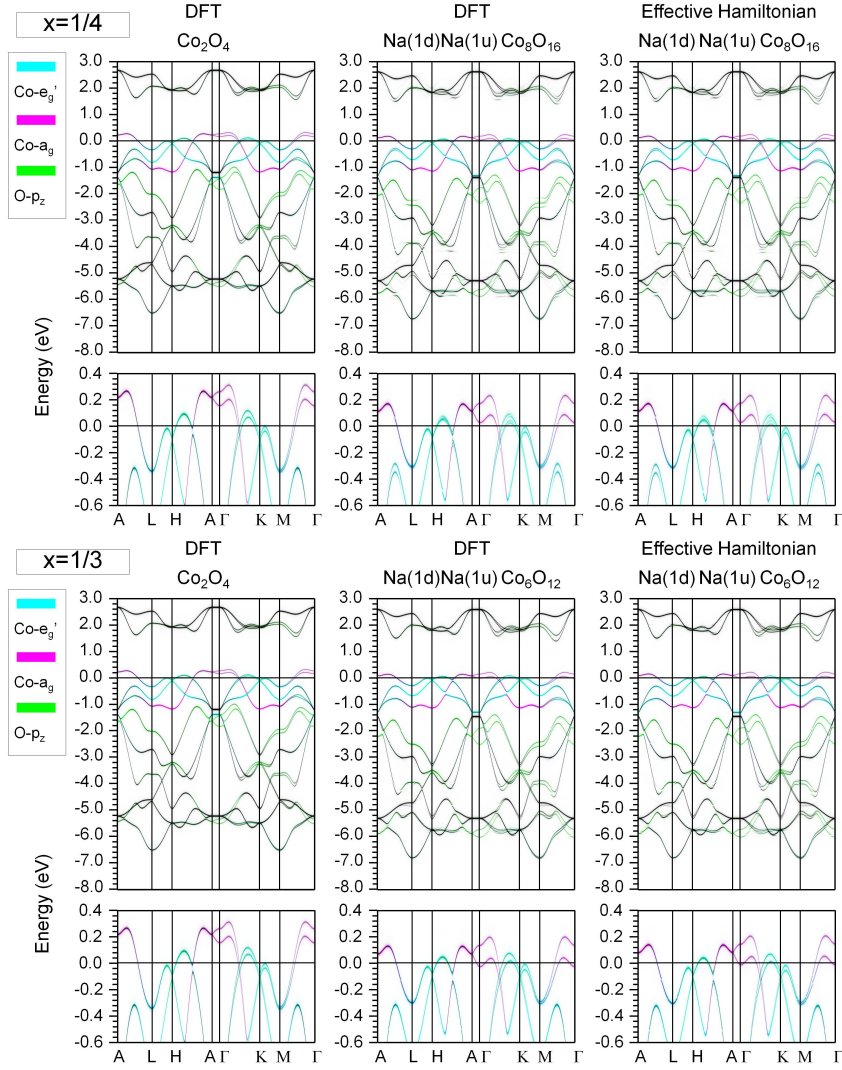
Figure G.1: The spectral functions $A(k, \omega)$ of test systems, calculated from the full DFT and the effective Hamiltonian.
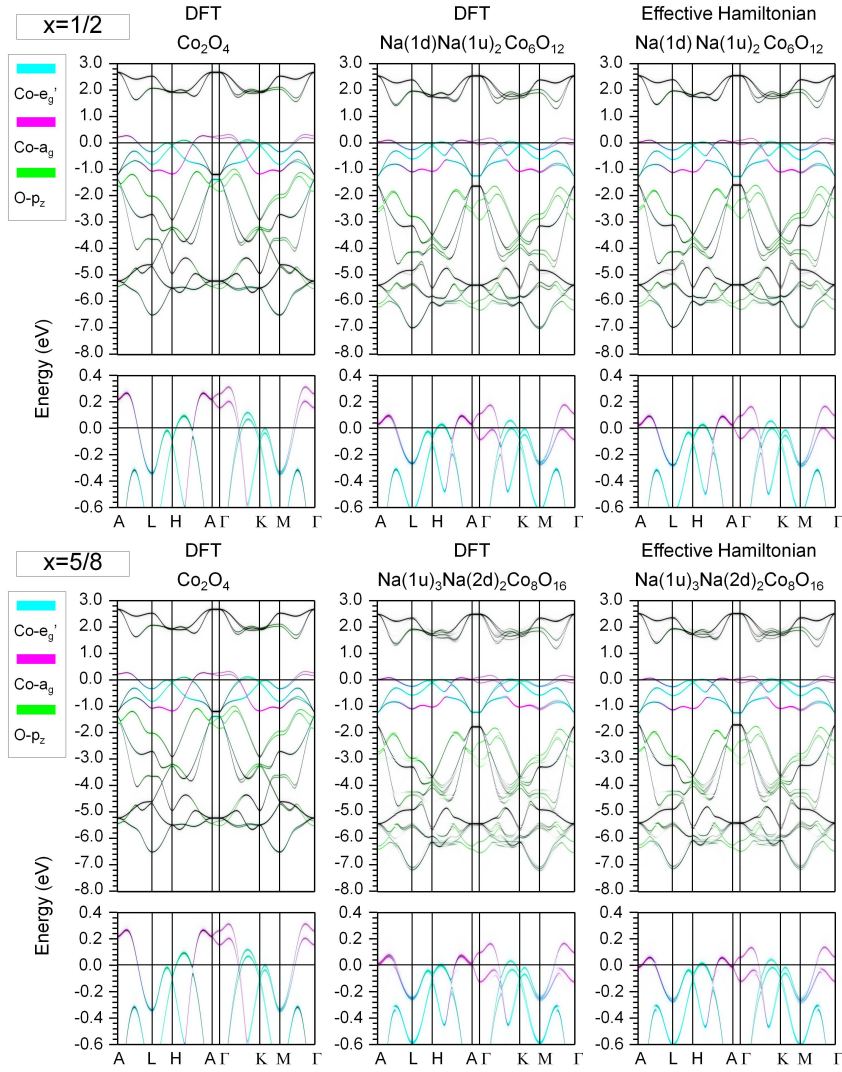
Figure G.2: The spectral functions $A(k, \omega)$ of test systems, calculated from the full DFT and the effective Hamiltonian.
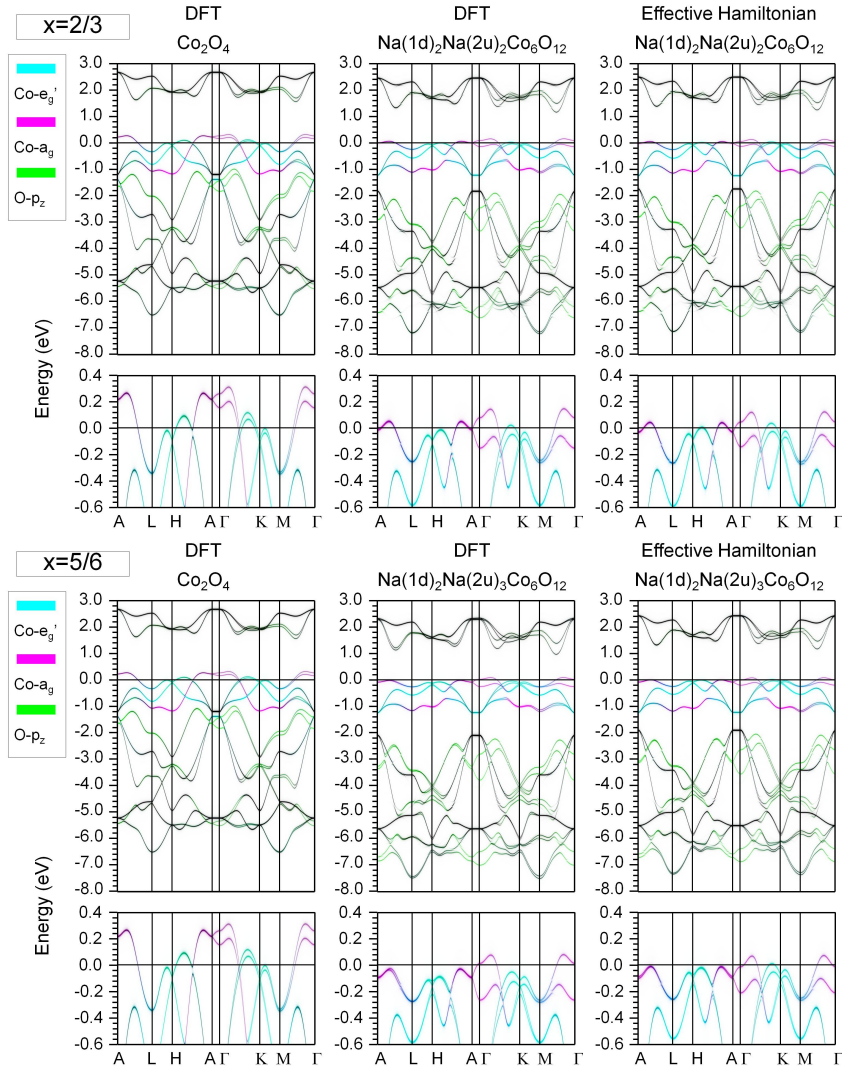
Figure G.3: The spectral functions $A(k, \omega)$ of test systems, calculated from the full DFT and the effective Hamiltonian.
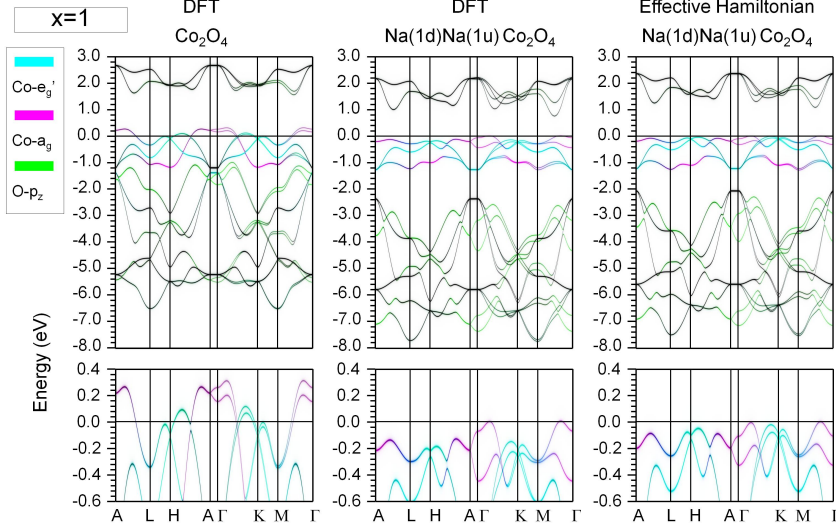
Figure G.4: The spectral functions $A(k, \omega)$ of test systems, calculated from the full DFT and the effective Hamiltonian.

Notice a systematic deviation near $x = 1$, which reflects the serious extrapolation from $x = \frac{1}{8}$ to $x = 1$. To some extent this deviation can be understood from the fact that at high doping ($x \gtrsim 5/6$), the e_g' pocket sinks below the Fermi level, after which it will no longer be exposed to additional electron repulsion. Unlike the DFT, the effective Hamiltonian method (as implemented in this work) does not treat the electron occupation self-consistently and therefore keeps adding additional electron repulsion to the e_g' states, even after they are already filled. If an effective Hamiltonian is needed to calculate the spectral function near $x = 1$, of course a much better approach would be to treat the small number of Na vacancies as impurities of $NaCoO_2$. For the present work however, the deviations near $x = 1$ are unimportant, because the main conclusion is on the lower end of the doping range ($x = 0.3$).

Appendix H

Estimating the Oxygen Vacancy Radius from the Theoretical Spectral Function

Suppose that in the supercell there is an eigenstate $|V_O\rangle$ associated with the oxygen vacancy with Gaussian form.

$$\langle r|V_O\rangle = e^{-\frac{r^2}{2\sigma^2}} \tag{H.1}$$

where the normalization constant is omitted and σ roughly equals half of the FWHM, in other words the radius of the oxygen vacancy state (since $e^{-\frac{r(N)^2}{2\sigma^2}} = \frac{1}{2} \Rightarrow x = \sqrt{2\ln 2}\sigma \approx \sigma$). From this the structure factor can be calculated:

$$\langle k|V_O\rangle = \sum_{r \in \text{supercell}} e^{-ikr}\langle r|V_O\rangle \tag{H.2}$$

Suppose that the size of the oxygen vacancy is bigger then the lattice constant but smaller then the supercell then we can use the identity

$$\int_{-\infty}^{\infty} dx e^{-i\alpha kx} e^{-\frac{x^2}{2\beta^2}} = \sqrt{2\pi}b e^{-\frac{1}{2}\alpha^2\beta^2 k^2} \tag{H.3}$$

121

to approximate the structure factor to be

$$
\begin{aligned}
\langle k|V_O\rangle &\approx \int d^3 r\, e^{-ik\cdot r} \langle r|V_O\rangle \\
&= \int d^3 r\, e^{-i\frac{2\pi}{a}k\cdot r} e^{-\frac{r^2}{2\sigma^2}} \\
&\propto \exp\left(-\frac{k^2}{2((\sigma\frac{2\pi}{a})^{-1})^2}\right)
\end{aligned}
\tag{H.4}
$$

From the structure factor follows the spectral function

$$
\begin{aligned}
A(k,\omega) &= \delta(\omega - \epsilon_{V_O})|\langle k|V_O\rangle|^2 \\
&= \delta(\omega - \epsilon_{V_O})\left|\exp\left(-\frac{k^2}{2((\sigma\frac{2\pi}{a})^{-1})^2}\right)\right|^2 \\
&= \delta(\omega - \epsilon_{V_O})\exp\left(-\frac{k^2}{2((\sigma\frac{2\sqrt{2}\pi}{a})^{-1})^2}\right)
\end{aligned}
\tag{H.5}
$$

So the final conclusion of this exercise is that the radius of the oxygen in real space is related to the radius in the spectral function by $\tilde{\sigma} = (\sigma\frac{2\sqrt{2}\pi}{a})^{-1}$. In the theoretically calculated spectral function we find the radius half of the FWHM to be roughly $1/10$ of ΓM, i.e. the radius $\tilde{\sigma} = 1/20$. From this it follows that the corresponding radius in real space is $\sigma = \frac{a}{2\sqrt{2}\pi}\frac{1}{1/20} \approx 2.25a$.

Appendix I

CPA Equations for 1 Dimensional 1 Band Binary Disorder

Before we can write down the CPA equations, we need to establish that the local Green's function $\langle r|G(z)|r\rangle = G_{rr}(z)$, also known as the locator can be expressed in terms of an interactor $\Delta_r(z)$. Here z is the complex generalization of frequency.

I.1   The Locator and the Interactor

claim 19 *Given the Hamiltonian*

$$H = \underbrace{\sum_r \epsilon_r c_r^\dagger c_r}_{E} + \underbrace{\sum_{r \neq r'} t_{rr'} c_r^\dagger c_{r'}}_{T} \tag{I.1}$$

then the locator equation of motion (from [53] page 61) is given by

$$G_{rr'} = g_r \delta_{rr'} + g_r \sum_{r'' \neq r} t_{rr''} G_{r''r'} \tag{I.2}$$

where the bare locator (with bare referring to no hopping) is given by

$$g_r = (z - \epsilon_r)^{-1} \tag{I.3}$$

proof 19

$$(z - H)G = 1$$
$$(z - E - T)G = 1$$
$$(z - E)G = 1 + TG$$
$$G_{rr'} = g_r \delta_{rr'} + g_r \sum_{r'' \neq r} t_{rr''} G_{r''r'} \tag{I.4}$$

claim 20 *The formal solution of the site diagonal part of G (from [53] page 137):*

$$G_{rr} = (z - \epsilon_r - \Delta_r)^{-1} \tag{I.5}$$

where the renormalized interactor is given by

$$\Delta_r = \sum_{r' \neq r} t_{rr'} g_{r'} t_{r'r} + \sum_{r' \neq r, r'' \neq r} t_{rr'} g_{r'} t_{r'r''} g_{r''} t_{r''r} + ... \tag{I.6}$$

proof 20 *We start with the off-diagonal part of the locator expansion*

$$G_{rr'} = g_r \sum_{r'' \neq r} t_{rr''} G_{r''r'} = g_r t_{rr'} G_{r'r'} + g_r \sum_{r'' \neq r, r'} t_{rr''} G_{r''r'} \tag{I.7}$$

Then we plug for $G_{r''r'}$ on the right as a first order approximation $g_{r''} t_{r''r'} G_{r'r'}$ to obtain:

$$G_{rr'} = g_r t_{rr'} G_{r'r'} + g_r \sum_{r'' \neq r, r'} t_{rr''} g_{r''} t_{r''r'} G_{r'r'} + ... \tag{I.8}$$

Now we plug this expansion into the diagonal part of the locator expansion

$$
\begin{aligned}
G_{rr} &= g_r + g_r \sum_{r'' \neq r} t_{rr''} G_{r''r} \tag{I.9} \\
&= g_r + g_r \sum_{r'' \neq r} t_{rr''} g_{r''} t_{r''r} G_{rr} + g_r \sum_{r'' \neq r} t_{rr''} g_{r''} \sum_{r''' \neq r'', r} t_{r''r'''} g_{r'''} t_{r'''r} G_{rr} + ...
\end{aligned}
$$

so we find

$$G_{rr} = g_r + g_r \Delta_r G_{rr} \tag{I.10}$$

124

which we can rewrite as

$$G_{rr} = \frac{g_r}{1 - g_r \Delta_r} = \frac{1}{g_r^{-1} - \Delta_r} = \frac{1}{z - \epsilon_r - \Delta_r} \qquad \text{(I.11)}$$

I.2   CPA Equations for 1 Band and 1 Dimension Binary Disorder

Now we consider the following one dimensional one band tight-binding model with nearest neighbor hopping t and a site energy that takes the random values 0 and ϵ:

$$H_0 = \sum_r t c_r^\dagger c_{r+a} + h.c. \; ; \; H = H_0 + \sum_r \epsilon_r c_r^\dagger c_r \; ; \; \epsilon_r \in \{0, \epsilon\} \qquad \text{(I.12)}$$

The bare local Green's function for H_0 can be taken from the literature (formula (5.29) in [52]):

$$G_0(z) = \frac{-i}{\sqrt{4t^2 - z^2}} \qquad \text{(I.13)}$$

From this we can derive an explicit formula for the interactor:

$$\Delta_0(z) = z - G_0^{-1}(z) = z - i\sqrt{4t^2 - z^2} \qquad \text{(I.14)}$$

Due to the inbedding in the medium the interactor will shift by the self-energy:

$$\Delta(z) = \Delta_0(z - \Sigma(z)) \qquad \text{(I.15)}$$

Now we can write down the CPA equation as the self-consistent average of the local Green's functions:

$$\langle G(z) \rangle = \frac{1}{z - \Sigma(z) - \Delta(z)} = \frac{1-x}{z - \Delta(z)} + \frac{x}{z - \epsilon - \Delta(z)} \qquad \text{(I.16)}$$

from which we can obtain the self-energy:

$$\Sigma(z) = x\epsilon + \frac{(1-x)x\epsilon^2}{z - (1-x)\epsilon - \Delta(z)} \qquad \text{(I.17)}$$

So all in all we have the following self consistent cycle:

1. Guess an initial self energy function, for example the VCA value: $\Sigma(z) = x\epsilon$

2. Plug the self-energy in (I.15) to obtain the locator.

3. Plug the locator in (I.17) to obtain self energy.

4. Plug the self-energy in (I.15) to obtain the locator.

5. etc